DEVELOPMENT AND APPLICATIONS OF THIN FILM RESISTS FOR ELECTRON BEAM LITHOGRAPHY

by

KURTIS C. FAIRLEY

A DISSERTATION

Presented to the Department of Chemistry and Biochemistry
and Graduate School of the University of Oregon
in partial fulfillment of the requirements of
Doctor of Philosophy

December 2015

DISSERTATION APROVAL PAGE

Student: Kurtis C. Fairley

Title: Development and Applications of Thin Film Resists for Electron Beam Lithography

This dissertation has been accepted and approved in partial fulfilment of the requirements for Doctor of Philosophy in the Department of Chemistry and Biochemistry by:

David Tyler	Chair
Darren Johnson	Advisor
David Johnson	Core Member
Richard Taylor	Institutional Representative

and

Scott L. Pratt	Dean of the Graduate School

Original approval signatures are on file with the University of Oregon Graduate School.

Degree awarded December 2015

DISSERTATION ABSTRACT

Kurtis C. Fairley

Doctor of Philosophy

Department of Chemistry and Biochemistry

December 2015

Title: Development and Applications of Thin Film Resists for Electron Beam Lithography

Throughout this work several thin film resists have been studied with substantial focus on HafSOx and SU-8. The study of HafSOx has granted more insight into how inorganic, spin coated films form and react under the electron beam. These films have been shown to form a thin dense crust at the surface that could have interesting implications in the interaction of the electrons. Continuing to further understand the electron interactions within the resist, low voltage patterns were created allowing the accelerating voltage to be matched to the film. With this general knowledge, higher resolution films can be constructed with shorter patterning times. Both resists complement each other in that HafSOx produces incredibly thin, dense structures to be formed with features below 10 nm in all dimensions. SU-8 allows micron thick features to be created over several millimeters. This flexibility in feature size enabled the creation of large fractals that could improve neuron binding to artificial retina down to the smallest fractals reported that are interesting for their applications as antennas. The final facet of this work involved looking at other methods of making structures. This was done through adding differing salts to organic molecules that stack into unique crystals.

This dissertation includes previously published co-authored material.

CURRICULUM VITAE

NAME OF AUTHOR: Kurtis C. Fairley

GRADUATE AND UNDERGRADUATE SCHOOLS ATTENDED:

University of Oregon, Eugene
Pacific Lutheran University, Tacoma, Washington

DEGREES AWARDED:

Doctor of Philosophy, Chemistry, 2015, University of Oregon
Master of Science, Chemistry, 2010, University of Oregon
Bachelor of Science, Chemistry, 2009, Pacific Lutheran University
Bachelor of Science, Physics, 2009, Pacific Lutheran University

AREAS OF SPECIAL INTEREST:

Thin Film Resists
Electron Beam Lithography
Fractals

PROFESSIONAL EXPERIENCE:

Graduate Research Assistant, University of Oregon, July 2009 – November 2015
Advanced Nanocrystal Characterization Intern, Life Technologies, June 2011 – January 2012
NSF RUI, Pacific Lutheran University, June 2008 – May 2009

GRANTS, AWARDS, AND HONORS:

Technology Entrepreneurship Program (TEP) Fellow, Lindquist College of Business, 2013

OMSI Science Communication Fellow, Oregon Museum of Science and Industry, 2014

Informal Science Education (ISE) Fellow, Center for Sustainable Materials Chemistry, 2013

Innovation Fellow, Center for Sustainable Materials Chemistry, 2012

Educational Outreach Fellow, Center for Sustainable Materials Chemistry, 2012

PUBLICATIONS:

Fairley, K.C.; Sharp, M.; Ditto, J.; Mitchson, G.A.; Johnson D.C.; Johnson D.W., Low voltage electron-beam lithography of HafSOx films, *Submitted to ACS Applied Materials & Interfaces*

Fairley, K.C.; Merril, D.R.; Woods, K.N.; Ditto, J.; Xu. C.; Gastufsson, T.; Johnson D.W.; Garfunkel, E.L.; Johnson, D.C.; Page, C.J., Non-uniform Composition Profiles in Inorganic Thin Films from Aqueous Precursors, *Submitted to ACS Applied Materials & Interfaces*

Watt, M.M.; Engle, Jeffrey M.; Fairley, K.C.; Robitshek, T.E.; Haley, M.M.; Johnson, D.W., "Off-on" aggregation-based fluorescent sensor for the detection of chloride in water, *Organic & Biomolecular Chemistry*, **2015**, 13, 4266-4270

Oleksak, R.P.; Ruther, R.E.; Luo, F; Fairley, K.C.; Decker, S.R.; Stickle, W.F.; Johnson, D.W.; Garfunkel, E.L.; Herman, G.S.; Keszler, D.A., Chemical and structural investigation of high-resolution patterning with HafSOx, *ACS Applied Materials & Interfaces*, **2014**, 6, 2917-2921

ACKNOWLEDGMENTS

I wish to express a deep appreciation for Professor Darren Johnson. Not only has he supported my growth as a scientist in the lab but also as a professional ready for the workplace. I have always felt supported in taking advantage of every opportunity, be that a six moth internship to get industrial experience or spending several weeks in Eastern Oregon helping set up an advanced chemistry course for rural schools.

I would also like to acknowledge some of my closest collaborators that have not only been a pleasure to work with but have directly contributed to this work. I have spent many hours discussing fractal geometry and neuron binding with Professor Richard Taylor and his lab. They are a wealth of knowledge and through the collaboration, became my favorite project I have worked on at the University of Oregon. I would like to take special note of Rick Montgomery and William Watterson in Richard's lab as incredibly helpful and a driving force in the project.

I would also like to note the excellent collaboration with Professor Dave Johnson's lab. Their expertise in modeling data was critical to understanding the composition of thin film resists and the electrons interactions within the material. I would like to take special note of Jeffry Ditto, Gavin Mitchson, and Devin Merrill in Dave's lab. Jeff and Gavin have both contributed to great discussions on the chemistry of thin film resists and microscopy in general.

I would also like to acknowledge the collaboration with Professor Michael Haley's lab and the interesting structures I was able to explore with their synthetic help. Without Jeffery Engle, I would not have been able to study any of the interesting crystal morphology, composition, and conductivity seen in chapter V.

I would like to acknowledge the Center for Sustainable Materials Chemistry, CSMC, for their support both financially and professionally. Many opportunities and collaborations throughout my time at the University of Oregon have been because of the CSMC. I would like to acknowledge CAMCOR facilities and staff. Without their instrumentation and guidance I would not have been able to complete this work.

Finally, I would like to acknowledge the support of my wife, Shannon Fairley, who has not only helped edit every paper I have written but also supported my pursuit of obtaining a doctorate. Without her, none of this would have been possible.

I would like to dedicate this to my loving wife, wonderful family, and fantastic friends.

TABLE OF CONTENTS

Chapter Page

Chapter Page

LIST OF FIGURES

Figure Page

Figure Page

CHAPTER I

AN INTRODUCTION TO LITHOGRAPHY AND HIGH RESOLUTION RESISTS

Chapter I consists of work that has not been published.

1.1. Chapter Introduction

In this chapter, the basics of lithography are discussed along with chemistry of several prominent resists that will be used throughout this work. This chapter will set the foundations for understanding the principles that guide the work to follow.

1.2. Introduction

Photoresists are a vitally important aspect of the world today, which can be seen by their rich history and every expending study. Photoresists have been around since the early 1900s, with Louis Minsk and Otto Suess creating the first synthetic negative and positive resists respectively. Since then it has become an ever exploding field particularly dominating the semiconductor industry. Ever since Feynman's famous "There's plenty of room at the bottom" lecture over half a century ago, there has been a steady push to decrease the feature size which has finally penetrated the single nanometer regime. [1]

It is important to understand the difference between the two main mechanics, negative or positive, by which resists are used and how they function. The first is a

negative resist that leaves behind any material that has been patterned. The second is a positive resist that removes the patterned material but leaves everything else behind. Both of these methods use the same principle: the interactions of the resist with an energy source cause a local solubility change to occur within the material itself. For negative resists, this is usually the condensation of inorganic material or cross-linking of polymers, making the patterned area insoluble whereas the rest of the film is dissolved away. The opposite is true for positive resists, where the energy source damages the patterned area and either physically removes it during the patterning or breaks it up enough that it becomes soluble.[2]

Another stark difference in the field is between inorganic and organic resists and how they fundamentally function. The most common organic resists are polymeric and, with a small number of cross-links formed or broken dramatically impacting the solubility, they have few active sites that react to the patterning beam. This generally makes the material very sensitive, meaning it takes very little energy to cause a solubility change. Conversely, inorganic resists generally have very small components that each require several active sites to react to cause a solubility change, dramatically reducing their sensitivity. Generally, organic resists are used to create large features over a large area because they are easier to pattern, but inorganic resists are able to produce smaller features and they are more resilient in post processing such as etching.

Understanding the different types of material is incredibly important, but equally important is understanding the method in which energy is delivered. Two main methods involve using electrons or photons. The main distinction between them is using a directed

beam (electrons) or a mask (photons). With directed beams, higher resolution is possible, but with a mask the lower resolution benefits from faster speeds and higher throughput.[3,4]

Next, the methods will be further broken down and their applications will be discussed. When using electrons or Electron Beam Lithography (EBL), a concentrated stream of electrons is accelerated toward the material to cause the chemistry to occur. This has allowed for features smaller than 10 nm to be patterned and is the cutting edge in resolution.[5] The drawback to this method is that a very small area is able to be patterned at one time, dramatically decreasing the throughput and limiting the industrial applications. In the case of photons or photolithography, a powerful lamp emits energy in all directions that is then filtered out by a mask, projecting the desired pattern. There are several types of photolithography that each differ by the energy used and thus the final resolution possible. The main method uses ultraviolet light but industry is moving towards extreme ultraviolet or even soft x-rays to take advantage of the smaller wavelengths. These methods have garnered impressive results, bringing the resolution to sub 20 nm features.[6] Photolithography is able to pattern large areas, resulting in an immense throughput that is incredibly industrially relevant. Other methods involving physical removal of the material can be used. This is usually accomplished by methods similar to ion milling or physical abrasion but are for niche applications usually where the depth is a critical and changing factor.[7]

1.3. Chemistry of HafSOx

A relatively new inorganic resist that shows high promise is HafSOx ($Hf(OH)_{4-2x-2y}(O_2)_x(SO_4)_y \bullet zH_2O$).[8] This resist is comprised of a hafnium oxychloride salt, dissolved

into a piranha solution, resulting in a semi-stable precursor that can be spun into a thin film. The amount of peroxide is not very critical, as once it saturates the hafnium, any excess will be lost during the spin coating process. However, peroxide is a critical component of the resist because it is sensitive to the electron beam and helps induce the solubility change. The sulfate plays a critical role, and it dramatically changes the sensitivity and resolution of the resist. At lower concentrations, the film has an increased sensitivity and contrast. This can be seen by concentration curves in Figure 1 where the lower dose squares are patterned at 0.7:1 but not at 0.85:1 (SO_4:Hf). The ratios of all three components have been optimized to 1:0.7:10, hafnium to sulfuric acid to peroxide, which provide the best resolution.[9]

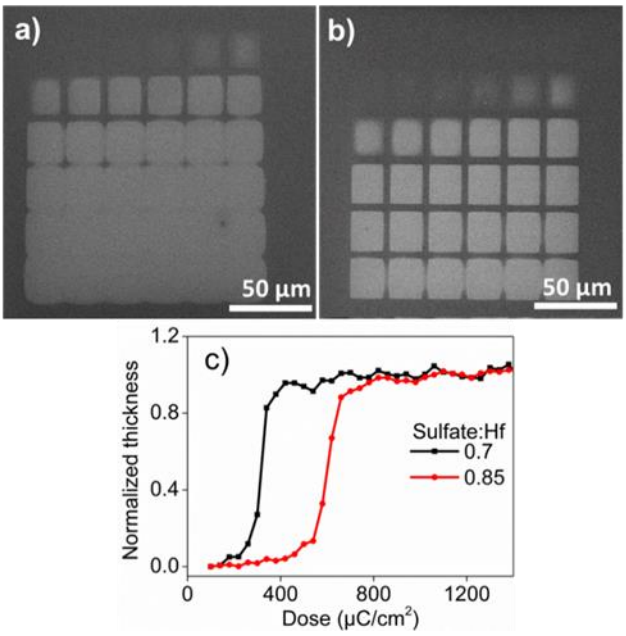

Figure 1: SEM images of dose arrays from 100 µC/cm2 to 1500 µC/cm2 (Top) for 0.7:1sulfuric to hafnium (Left) and 0.85:1 sulfuric to hafnium (Right). Dose curves are plotted for both (Bottom) through ellipsometry measurements.

To process the films, once the resist solution has been created, the surface of a silicon wafer is cleaned by oxygen plasma. Not only does this remove any trace organic compounds but also makes the wafer hydrophilic, increasing the wettability. The solution is then spun on the wafer to make a thin film. The thickness of the film depends on the concentration of the precursor but to achieve a ~20 nm thick film, a 0.15 M Hf solution spun at 3000 RPM is used. Increasing the concentration of the solution can provide films up to ~60-80 nm thick if needed. The films go under a soft bake, under 100 °C, to densify and remove unnecessary solvent before patterning. The patterning is currently done using a scanning electron microscope where an electron beam is used to pattern the film. After the film is patterned, it is developed in 25% tetramethylammonium hydroxide to dissolve any unpatterned material. This step also swaps the sulfate counter ions for hydroxide and allows for the final bake, above 300 °C, to produce dense, hafnium oxide.

1.4. Patterning HafSOx

There are several things to consider when patterning HafSOx. The first and most critical is the dose as it controls the amount of sites activated in the resist. HafSOx is typically patterned at a dose of 800 $\mu C/cm^2$ to achieve highest resolution but when patterning low resolution large features, doses as low as 500 $\mu C/cm^2$ can be used. It is also critical to keep the pitch to the beam at 5-10 nm when patterning high resolution features to prevent any gaps of unexposed resist between each pass. This can be extended to ~50 nm when patterning features over ~50 μm due to the enlargement of the spot size and blurring of the beam. With a highly aligned beam that is in focus and stigmated properly, sub 10 nm lines are achievable. These features are even achievable at larger magnifications, allowing for several different size scales to be serially patterned without

any loss in resolution, as seen in Figure 2, giving access to large intricate surface structures.

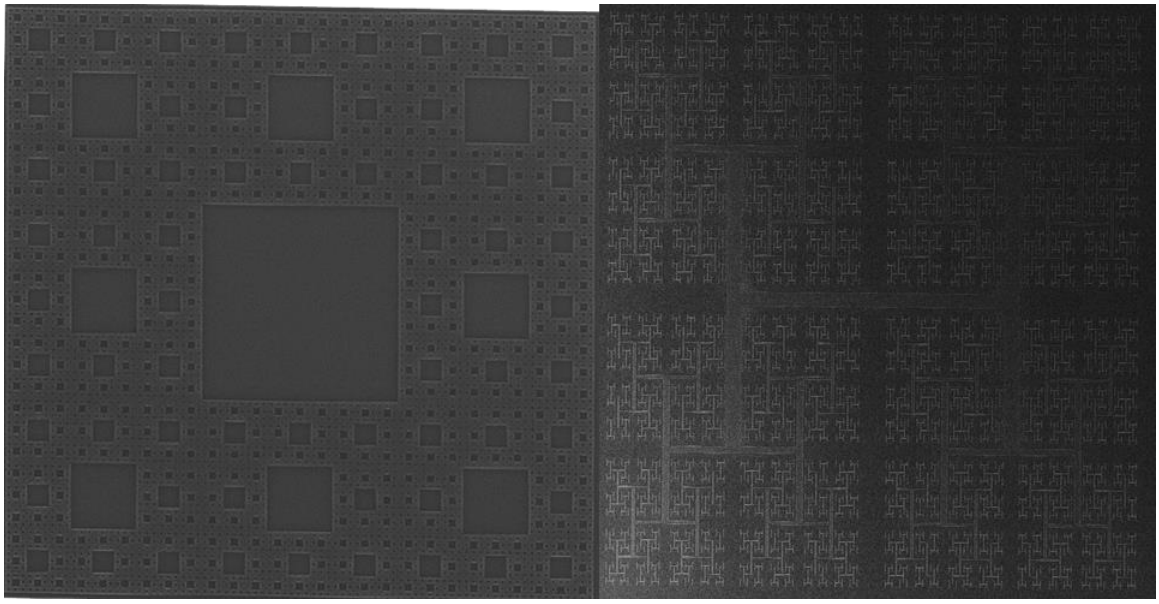

Figure 2: HafSOx patterns that both span from 100 μm in overall size to 15-30 nm as the smallest features. The patterns include wells (left) and ridges (right) displaying the versatility of the resist.

1.5. Rival Resists

There are several other commercially available resists that rival HafSOx in performance. The most closely related is HSQ (hydrogen silsesquioxane) which is a silicon based cluster that creates a negative tone resist when spun with sub 10 nm resolution.[10] HSQ has a very similar performance to HafSOx but is a commercial product with limited details publicly available. HafSOx still allows incredibly high resolution but also allows for a better understanding of the chemistry. HSQ is a very high resolution inorganic resist and there are several high resolution organic resists as well. Both NEB and SU-8 are relatively high resolution negative tone resists that are chemically

amplified, photoprotected catalysts are added, dramatically increasing the sensitivity but the final pattern has poor resistance to most etching.[5]

1.6. Other Forms of Lithography

There are several other forms of lithography that can be used to make small features other than the dominant UV and electron beam lithography previously mentioned. Two physical methods include nano imprint and scanning probe lithography. Nano imprint uses a physical model that shapes the surface before it is hardened allowing many replicas to be made in quick succession but with a low resolution. In contrast, scanning probe lithography deposits very tiny amounts of material that when hardened form high resolution features, but the process is very slow.[11] As alternative approaches, both ion beam lithography and physical evaporation take advantage of moving the material to and from the surface. Ion beam lithography has the ability at low current to deposit material onto the surface or at high current remove it entirely. This allows for very high resolution features to be patterned in both a negative or positive fashion.[7] Physical evaporation requires a mask to block a cloud of material which then is deposited on the surface. The resolution of the features is dependent on the mask used and material deposited. All of these methods can be used to create nano-scale features and have strong advantages but usually lack in either resolution or speed, limiting their applications.

1.7. Conclusion

Lithography is a fundamental component of many fields of industry and research that has made great strides in the last 100 years. Two basic forms of lithography have emerged as the dominant methods used, UV and EBL, which compete regarding speed

and flexibility. For creating the same pattern over and over, UV lithography is incredibly fast since it can pattern very large areas in parallel, and with advances in EUV the resolution has become close to EBL. EBL is still the most practical tool for creating extremely high resolution features especially if they change often. This is due to the fact that a physical mask is not required to pattern and the beam is controlled by a CAD file. This leads to the conclusion that innovation demands strong advances in EBL, and EBL resists that will allow the flexibility to discover new and interesting phenomena and interactions that occur on the nanoscale.

1.8. Co-authored Work

Several chapters include co-authored work in collaboration between several labs. section 2.2 in Chapter II has work that was submitted for publication in collaboration with Dave Johnson, Catherine Page, and Eric Garfunkel's lab. The specific co-authors are Devin Merril, Keenan Woods, Jeffery Ditto, Can Xu, and Torgny Gastufsson. They contributed modeling, AlPO material, TEM cross-sections, and MEIS data respectively. Section 2.3 in Chapter II has work published in collaboration with Douglas Keszler, Gregory Herman, and Eric Garfunkle's lab. The specific co-authors are Richard Oleksak, Rose Ruther, Feixiang Luo, Shawn Decker, and William Stickle. Richard and Rose preformed TEM cross-sections, Feixiang preformed XPS. Work in section 3.2 of Chapter III was submitted for publication in collaboration with Dave Johnson's lab. The specific co-authors are Meredith Sharp, Gavin Mitchson, and Jeffery Ditto. They contributed dose curves, simulations, and TEM cross-sections respectively. Chapter IV could be published with the co-authors William Watterson and Rick Montgomery who have done extensive modeling of the electric field produced from fractal top contacts. Section 5.2 through 5.5

of Chapter V was done in collaboration with Michael Haley's lab. The Specific co-authors are Calden Carroll and Jeffery Engle. Both contributed to the synthesis of the organic molecule.

CHAPTER II

CHARACTERIZATION AND PREFORMANCE OF A HIGH RESOLUTION INORGANIC THIN FILM RESIST: HAFSOX

Chapter II consists of work that has been submitted for publication in ACS Applied Materials and Interfaces; Fairley, K.C.; Merril, D.R.; Ditto, J.; Johnson, D.C.; Johnson D.W.; Garfunkel, E.L.; Keszler, D.A., *The structure of inorganic resists: Non-uniform density profiles in HafSOx films.* It also consists of work that has been published in ACS Applied Materials and Interfaces: Oleksak, R.P.; Ruther, R.E.; Luo, F; Fairley, K.C.; Decker, S.R.; Stickle, W.F.; Johnson, D.W.; Garfunkel, E.L.; Herman, G.S.; Keszler, D.A., Chemical and structural investigation of high-resolution patterning with HafSOx, *ACS Applied Materials & Interfaces*, **2014**, 6, 2917-2921

2.1. Chapter Introduction

Understanding the chemical and structural composition of emerging resists has been shown to be vital in improving their performance and designing new resists needed for the next generation of lithography.[1,2] In this chapter, the density profile of HafSOx is examined and characterized revealing a thin, dense crust at the surface. Following the density study, standard electron beam lithography is used to determine the resolution

capable with the resist and transmission electron microscopy is used to examine the cross section of the features along with the unintended film left behind.

2.2. Density Profile of HafSOx Introduction

A variety of metal oxide films ($InGaO_x$, AlO_x, 'HafSOx') prepared from aqueous solutions were found to have non-uniform electron density profiles using X-ray reflectivity. The inhomogeneity in HafSOx films ($Hf(OH)_{4-2x-2y}(O_2)_x(SO_4)_y \bullet zH_2O$), which are currently under investigation as inorganic resists, were studied in more detail by HAADF-STEM and MEIS. The HAADF-STEM images show a greater concentration of heavy atoms near the surface of a single layer film. MEIS data confirms the aggregation of Hf at the film surface. The denser 'crust' layer in HafSOx films may directly impact patterning resolution. More generally, the phenomenon of surface layer inhomogeneity in solution-deposited films likely influences film properties and may have consequences in other thin film systems under investigation as resists, dielectrics and thin-film transistor components.

Inorganic coatings are ubiquitous in modern technology. While the majority of inorganic coatings are made via high vacuum processes (e.g., sputtering, evaporation, atomic layer deposition), there has long been an interest in preparing dense, smooth inorganic coatings using a solution route. Perhaps the most widely studied solution route to thin films is the sol-gel method, which generally employs non-aqueous solvents.[3] This method has been used to prepare films with varying degrees of porosity and a wide range of pore sizes. Sol-gel-derived monoliths and films can generally be described as porous rigid oxide networks in which the pores are filled with liquid or gas.[3,4] More recently,

Keszler and coworkers have developed a 'Prompt Inorganic Condensation' (PIC) aqueous route to prepare ultra-smooth amorphous inorganic films with a variety of cations by controlling the condensation process.[5–12] This method allows the preparation of dense oxide films with near-atomic surface smoothness, presumably due to the surface tension of the water-based solution during spin coating.[5,12] Film thicknesses can easily be controlled via the concentration of the solution and the physical parameters used to spin the films. Thin films made via PIC have been incorporated into thin-film transistors using spin coating and low temperature annealing to obtain devices that meet or exceed the performance of conventional vapor-deposited devices.[7,13–17] PIC films prepared from solutions of hafnium oxychloride dissolved in sulfuric acid (HafSOx) with added peroxide have been shown to function as ultra-high resolution resists, patternable with electron beam or extreme ultraviolet radiation.[18,19] These resists enable patterning with minimum linewidths and edge roughnesses superior to those obtainable using organic resist materials using conventional lithography techniques. These advantages are expected to become even more important for extreme ultraviolet (EUV) lithography in next generation semiconductor manufacturing.[20]

For solution-processed films, developing a fundamental understanding of the chemistry occurring in each processing step is critical for improving film morphology and performance.[1,21–24] In the case of inorganic metal oxide films (using sol-gel or PIC), processing steps include: film deposition (via spin coating or dip coating), a "soft bake" to drive off excess solvent, and higher temperature annealing to facilitate counterion removal and condensation. In the sol-gel process, evaporation of organic solvent molecules and simultaneous hydrolysis reactions at relatively low temperatures lead to a

stiff inorganic network, and subsequent drying occurs via evaporation from pores.[25] By contrast, in the aqueous PIC route, evaporation of solvent (water) involves considerably more energy due to hydrogen bonding and increased solvent/solute interaction strength. The loss of water leads to condensation reactions that directly link the inorganic species as their concentration increases.[14]

Although fundamentally different chemistries occur in the various methods used to prepare inorganic films, drying and densification models generally assume the resulting films are homogeneous.[25] However, there are a few previous studies that show inhomogeneities in sol-gel- derived multilayer films observable by TEM[26] or X-ray reflectivity (XRR).[27,28] Denser surface 'crusts' in single-layer films have also been observed via ellipsometry in sol-gel silica coatings[29] and by XRR in PIC aluminum oxide phosphate films.[30] The nature of these inhomogeneities, whether due to density variations or compositional inhomogeneity, has not been determined. This prompted us to undertake a systematic study of density and composition gradients in PIC-prepared films using multiple techniques.

In this paper we present XRR data on a variety of films made using PIC with different metal precursor solutions. Films comprised of multiple layers yielded XRR patterns inconsistent with those expected for homogeneous films, suggesting density or composition gradients in the individual layers. Using HafSOx as a model system, single and multilayer films annealed at different temperatures were examined using XRR, cross-sectional high-angle annular dark-field scanning transmission electron microscopy (HAADF-STEM), and medium energy ion scattering (MEIS). These techniques reveal the evolution of density and compositional inhomogeneity in the films during processing.

They suggest a thin, dense surface 'crust' forms during spin coating, presumably because the reactants near the surface dehydrate faster than the interior of the film. This surface 'crust' persists during subsequent low temperature annealing, but surprisingly does not increase in thickness. Because the performance of photoresists has been shown to be very sensitive to processing conditions,[23] controlling the inhomogeneity in HafSOx films may be an important avenue towards improving performance in ultra-high resolution resist applications. More generally, the presence of a dense surface layer may affect the kinetics of film formation, as well as the final properties of metal oxide films derived using PIC. Therefore, understanding and controlling the formation of the surface layer is important for tailoring the evolution and properties of films made using this method.

2.2.1. Experimental

$InGaO_x$ and AlO_x Films: A 2.00 M total metal concentration (6:7 In:Ga) solution of $In(NO_3)_3 \cdot xH_2O$ (Sigma Aldrich, 99.9% In) and $Ga(NO_3)_3 \cdot xH_2O$ (Alfa Aezar, 99.999% Ga) and a 1.70 M metal concentration solution of $Al(NO_3)_3 \cdot 9H_2O$ (Alfa Aezar, 98% Al) were electrochemically treated to reduce nitrate counterion concentrations according to known methods.[31,32] Both solutions were diluted to 0.25 M (total metal concentration) with 18 MΩ nanopure water and filtered through 0.45 μm PTFE filters.

HafSOx Films: A 1.00 M stock solution of $HfOCl_2 \cdot 8H_2O$ (Alfa Aesar, 98% Hf) was prepared by dissolution and dilution with 18 MΩ nanopure water. Solutions for spin coating were prepared by mixing 2.000 N H_2SO_4(aq) (VWR) and 30 wt% H_2O_2(aq) (EMD Millipore) followed by the addition of $HfOCl_2$(aq). The final solution was diluted

using 18 MΩ water to a concentration of 0.105 M sulfuric acid, 0.45 M hydrogen peroxide, and 0.15 M hafnium. The 4-coat multilayer was synthesized from a solution without peroxide to decrease the solubility of the film, allowing for a lower annealing temperature to prevent subsequent layers from dissolving the previous.[19]

N-type, Sb-doped silicon substrates (0.008-0.02 Ω*cm) received surface treatments using a MΔRCH cs-1701 plasma cleaner running on O_2 plasma at 30% O_2 in N_2 using 150 W for 60 s immediately before spin coating. Films were prepared by filtering the solutions through a 0.45 μm filter and spin-coating at 3000 rpm for 30 s. The HafSOx thin films were subjected to a one minute anneal at either 80 °C for a single layer or 180 °C for the multilayer samples. The $InGaO_x$ and AlO_x multilayer films were annealed at 450 °C for 20 min per coat followed by a final 60 min anneal at 450 °C.

XRR patterns were obtained on a Bruker D8 discover (Cu k_α radiation). Sample alignment was checked to ensure that the incident and exit angle were equal and that the sample was in the center of the goniometer. Alignment procedures involved iteratively performing rocking curves and z (height) scans to ensure the above criteria were met.[33]

Fits of the XRR data were performed using the BEDE Refs software package, which creates a population of solutions based on an initial model and uses a genetic algorithm to minimize residuals.[34] Once the best fit was achieved, the models were perturbed to confirm that the model was not a local minimum. Films were initially fit as a single film, to determine the average density and total film thickness. For single-coat films, the model was then split in half, with each half allowed to vary thickness and density independently to improve the fit. A gradient was also added to the fit, as the

abruptness of the interface was unknown. Comparison of the residual values over a constant range allows for the quantitative comparison of the fits for a single-coat film. Multilayer films were modeled similarly; each coat was split into a two-layer unit and each layer was allowed to vary independently in thickness and density (all coats assumed to be identical).

For scanning transmission electron microscopy (STEM) investigations, a thin cross-section sample was prepared from a section of the film using an in-situ lift-out process on a FEI Helios 600 equipped with a Sidewinder ion column and a Quorum cryo stage.[35] Steps were taken to avoid exposure of the beam-sensitive film while imaging with the SEM and sputtering with the focused ion beam (FIB). Prior to loading the sample in the FIB-SEM, the sample was coated with a 30 nm protecting layer of evaporated carbon. A second 1.5 μm thick protecting layer of FIB-induced carbon was deposited over the area of interest using a 2 keV accelerating voltage (<5 nm stopping range in evaporated carbon). The lift-out and thinning process was carried out using a 500 eV accelerating voltage on the electron beam to minimize the interaction volume of the beam (<9 nm interaction depth). After completing the lift-out, the sample remained 1.5 μm thick to assure no beam interaction had taken place. The sample was then cooled to -170 °C throughout the thinning process. The FIB accelerating voltages used were lowered as the thickness decreased, 30 keV (1.5 to 0.5 μm), 5 keV (500 to 100 nm), and 2 keV (100 to 40 nm). During thinning the sample was monitored using low dose electron beam conditions to reduce risk of exposure and excessive heat (periodic single frames using 500 eV, 90 pA, 500 ns dwell per pixel, 50 um horizontal field width, 1024x768 pixels). The thin sample (approx. 40 nm thick), was warmed slowly overnight in the FIB-

SEM vacuum chamber to ambient temperature. High-angle annular dark-field (HAADF) STEM imaging was completed on a FEI Titan at 300 keV (0.245 m camera length, 10 μs dwell, 2048x2048 pixels, 0.6 nA current) at -175°C with a Gatan single-tilt cryo-transfer holder.

Medium energy ion scattering (MEIS), a high resolution version of Rutherford backscattering (RBS), was performed at the Rutgers MEIS facility using 130 keV protons as the incident ion.[36] All atom ratios have an error of +/- 0.05 and densities have an error of +/- 0.1 associated with the measurement.

2.2.2. Results and Discussion

Four-coat samples of $InGaO_x$, AlO_x, and HafSOx were prepared using PIC as described above and examined by XRR (Fig. 1). For all samples, the XRR patterns

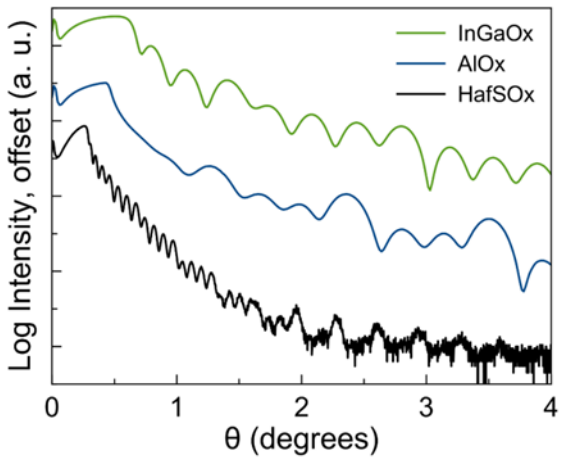

Figure 1: XRR patterns of 4-coat films of $InGaO_x$, AlO_x, and HafSOx, (top to bottom, respectively). The patterns are offset for clarity.

consist of regular Kiessig fringes with a pattern of varying intensity. Figure 2a contains a schematic of two potential structures of these films, one that is homogeneous and one that contains a repeating structure of four layers (coats) where each layer has an identical non-uniform electron density gradient. Figure 2b contains the calculated XRR patterns for these two films. Since XRR is very sensitive to variations in electron density, small (1%) differences in electron density can be detected. The calculated XRR pattern for a homogeneous single film shows a characteristic systematic decay in the Kiessig fringe intensity with increasing diffraction angle. The calculated XRR pattern of the film with a repeating inhomogeneous layered structure contains a characteristic modulation of the Kiessig fringe decay, with more intense diffraction maxima corresponding to the thickness of the individual layers resulting from the coherent scattering of the electron density profiles in each layer. Between these more intense maxima are n-2 smaller maxima, where n is the number of coats, resulting from incomplete destructive interference. All of the multilayer films prepared via PIC have XRR patterns (Fig. 1) characteristic of films consisting of repeating layers of non-uniform electron density profiles, inconsistent with those expected for homogeneous films. This suggests that this inhomogeneity is a general characteristic of PIC solution-deposited thin films. We elected to study the effects of this phenomenon in more detail for the HafSOx system.

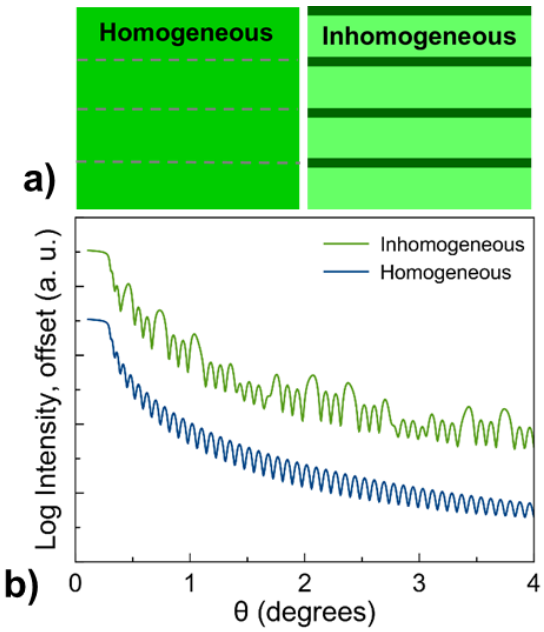

Figure 2: (a) A schematic representation of two simple structures of a 4-coat stack, one in which each coat is homogeneous and one where each coat has the identical inhomogeneous electron density. (b) The modeled XRR data for the two cases shown in (a).

In Figure 3, we model the XRR data of the 4-coat HafSOx film assuming that each deposited coat consists of a bilayer: a 'bulk' layer and a surface layer. The density and thickness of the bulk and surface layers were allowed to freely vary in order to obtain the best possible fit. It was assumed that all four coats were identical. Within these constraints, the best fits were obtained with a thin surface layer (or 'crust') in each coat with a higher electron density than the underlying bulk layer.

A single coat film was also investigated to determine if the 'crust' is inherent in each coat or whether it is induced by the processing conditions used to make the 4-coat multilayer. To match the processing of the 4-coat multilayer, the film was annealed at 180 °C. XRR data for the single coat film was modeled both as a homogeneous single

layer film and as a bilayer, with a surface and bulk layer which were allowed to freely vary in thickness and electron density (Figure 4).

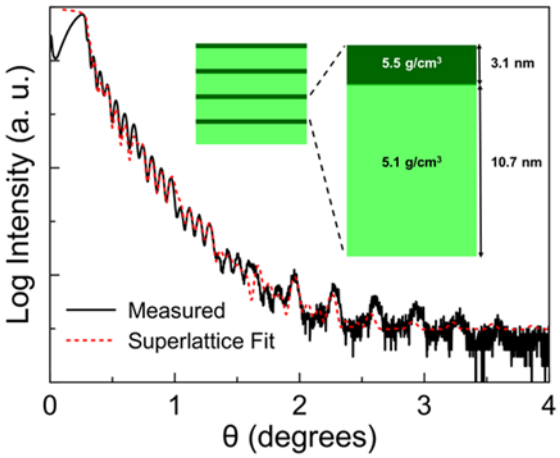

Figure 3: The raw and modeled XRR data of a 4-coat multilayer of HafSOx.

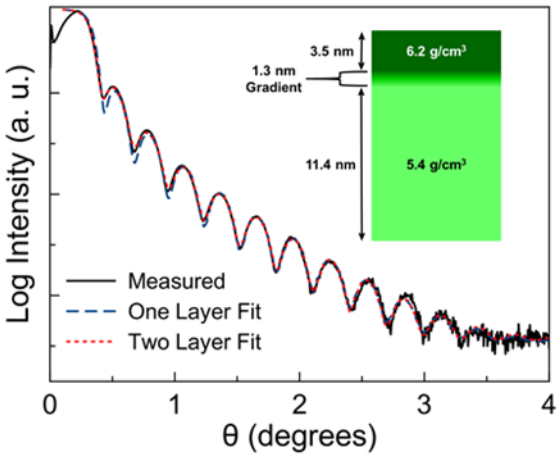

Figure 4: XRR data for a single coat film without peroxide annealed to 180 °C. The data was modeled as a homogeneous layer and as a thin top dense layer over a less dense bulk film. The addition of the surface 'crust' improved the agreement between the model and the data, especially in the first three observed minima in the XRR pattern.

Between the two models, the two-layer model with a thin, denser ‘crust’ has a 20% reduction in the residuals as compared to the single-layer model when both models are allowed to search for the minimum using the genetic algorithm and modeling procedure described above. Perturbing the models from the fits to find better solutions was unsuccessful, indicating the refined fits represent global minima. This suggests the best description of the film within the applied modeling constraints is that of a less electron-dense layer topped by a thin, higher electron density ‘crust’. These are probably separated by a thin gradient region between the surface and bulk layers, but this was not included in the model.

Since it has previously been reported that peroxide-containing HafSOx films used for lithography were homogeneous,[19] new films containing peroxide were prepared to test whether the crusts observed above also occur when peroxide is added. These peroxide-containing films were also used to examine the effect of annealing temperature. In order to replicate HafSOx films used for patterning, a single coat film containing peroxide was annealed to the soft-bake temperature of 80 °C for XRR studies. As seen in Figure 5, not only does the bilayer model give a better fit to the data, but the residuals are reduced by 50% when the model is allowed to create two layers separated by a gradient. This supports the formation of a ‘crust’ in films containing peroxide, even at the low soft bake temperatures used for lithography.

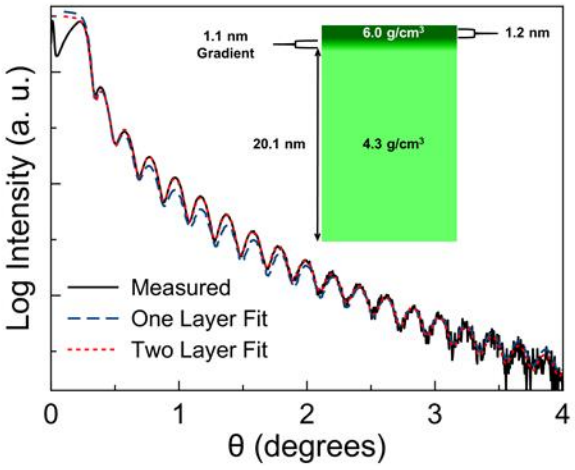

Figure 5: XRR data for a single coat film containing peroxide annealed to 80 °C. The data was modeled as a homogeneous single layer and as bilayer consisting of a thin top dense layer on a less dense bulk layer. The addition of the surface 'crust' improved the agreement between the model and the data, especially with respect to the minima in the XRR pattern between 0.8 and 2 degrees.

XRR studies reveal electron density gradients and periodicity (in multilayers), but do not reveal the source of the density gradients (i.e., whether they are due to density variations of a single chemical composition or a chemical gradient). Additional information on the HafSOx films was obtained using HAADF-STEM. Cross sections of a single coat film containing peroxide were prepared with care to maintain its condition prior to exposure, and a representative cryo–HAADF STEM image is shown in Figure 6a. The image reveals a bright thin band at the top of the sample indicating an increased density of heavy atoms at the surface. Texture can be observed throughout the film. Integration of the average HAADF signal intensity over the highlighted area in Figure 6a provides a two-dimensional plot of the heavy atom density profile across the film (Figure 6b). This indicates that in addition to concentration of heavy atoms at the surface of the film, there is also a slight increase of heavy atom density near the bottom of the film.

This data provides direct evidence that there is electron density inhomogeneity within the films and supports the two-layer XRR model used above.

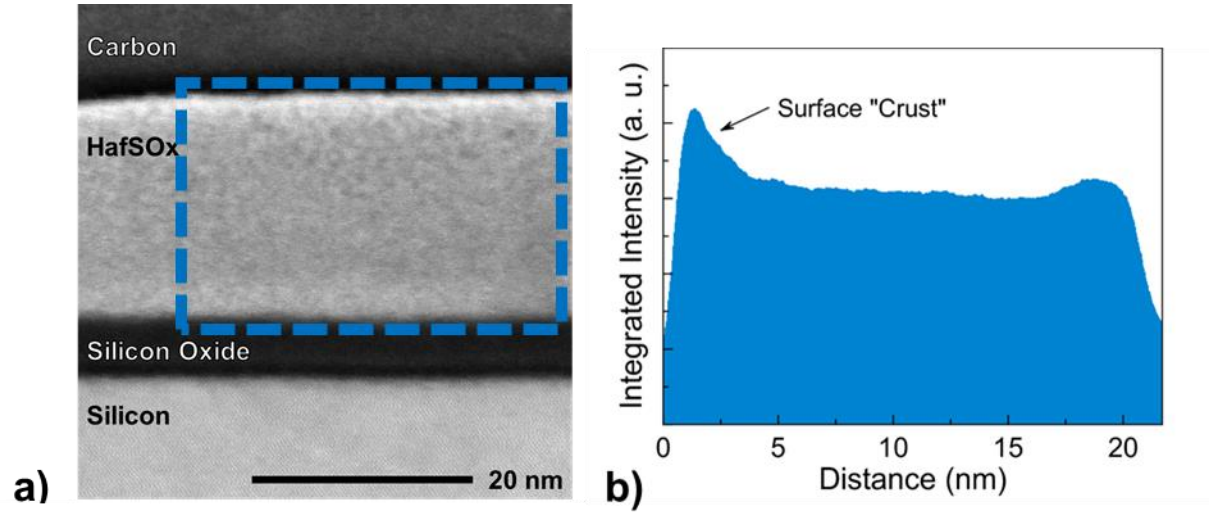

Figure 6: (a) Side on view of a TEM cross-section of a single layer HafSOx film, and (b) the heavy atom density profile of the film.

In order to obtain information about *chemical* inhomogeneity, medium energy ion scattering (MEIS) data was collected as a function of annealing temperature and time on a different set of HafSOx films made in a similar manner. MEIS data (Figure 7) shows clearly that the increased intensity in the HAADF-STEM image at the surface of the film is due to increased concentration of heavy atoms (in this case hafnium). In MEIS, the detected energy of the backscattered ions depends on the incident ion energy, the masses of the incident ion and scattering element, and the depth of the scattering element in the substrate. The spread in energy of the backscattered ions is related to thickness of the scattering element layer in the substrate and the intensity of the scattering depends on the density of the scattering ion. The highest energy peak results from protons backscattered from Hf in the film. It is apparent that the density of Hf is highest at the surface of the

films (as suggested by the HAADF-STEM images). It is also readily apparent that the film thickness decreases and becomes denser as the annealing temperature is increased (Figure 7b). The MEIS data can be modeled, yielding for the film annealed at 80 °C a 3.3 nm surface layer with a density of 2.8 g cm^{-3} and a composition that can be modeled as ~$Hf_{1.7}S_{0.8}O_5$ above an 18 nm thick $Hf_{1.0}S_{0.8}O_5$ film with a lower density of 2.5 g cm^{-3}, suggesting that the increased density is a result of increased Hf at the surface.

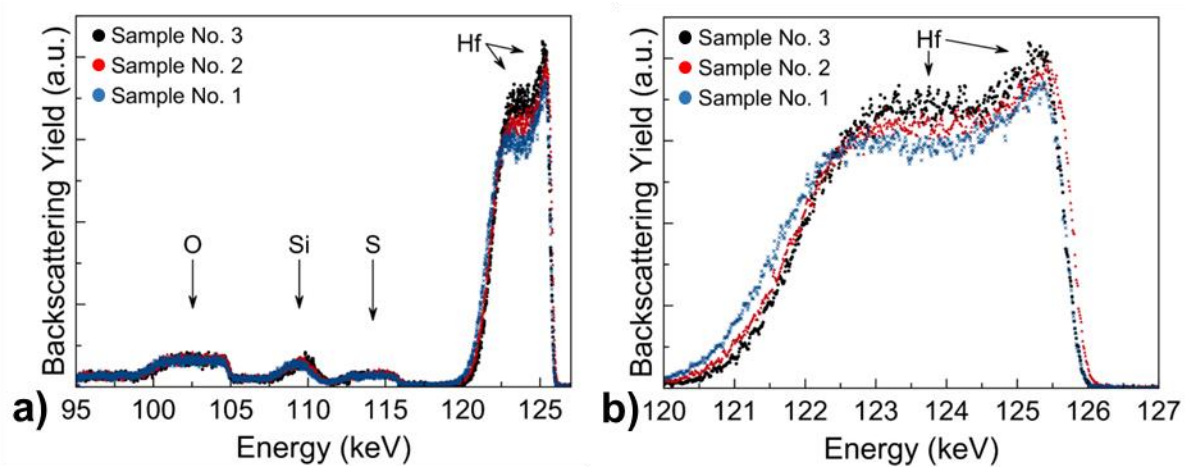

Figure 7:(a) MEIS data collected on a film annealed for 3 minutes at 80 °C (blue), 5 minutes at 150 °C (red) and 5 minutes at 300 °C (black). (b) An expansion of the Hf area clearly shows the total film thickness decreasing with increasing annealing temperature while the average density increases. The peak at 125 keV indicates that all of the films have a surface layer with higher Hf density.

The MEIS data modeling also suggests that the Hf-containing film reacts with the SiO2 surface of the silicon wafer to form a 4.0 nm thick layer with approximate composition $Hf_{0.07}SiO_2$ and a density of 2.2 g cm^{-3}. Increasing the annealing temperature to 150 °C decreases the thickness of the surface layer to 2.5 nm, increases its density to 3.5 g cm^{-3}, and decreases the thickness of the bulk of the film to 14 nm and increases its density to 3.3 g cm^{-3}. There is no significant change in the Hf-containing SiO_2 layer at the

interface with the silicon wafer. Increasing the annealing temperature to 300 °C further decreases the thickness of the surface layer to 2 nm and the thickness of the bulk of the film to 11 nm while again increasing their density. The MEIS data is consistent with the results obtained from XRR and STEM investigations, all showing the formation of a surface 'crust' during the initial spin coat and 80 °C anneal.

2.2.3. Summary

The data presented suggests that films prepared from aqueous solutions via the PIC process are inhomogeneous in composition and density throughout their thickness. For HafSOx films, a dense region forms at the surface after a low temperature anneal. This may result from enhanced evaporation of solvent at the surface of the film, increasing concentration and resulting in condensation reactions between the Hf-containing moieties to yield a dense surface layer on the film. Presumably this acts as a diffusion barrier, leading to the lower density observed in the bulk of the film. We postulate that the slow rate of water diffusion through the 'crust' relative to the rate of diffusion within the 'bulk layer' of the film prevents the formation of density gradients in the bulk of the film during subsequent annealing. In the case of HafSOx, the denser surface layer may influence the patterning resolution and contrast obtainable with this system. It may be possible to control the density and/or thickness of the surface 'crust' by adjusting annealing conditions (e.g., temperature, atmosphere, ramp rate) and to correlate changes with patterning metrics. We also show that 'crust' formation is quite general for PIC processed films, and that the density inhomogeneities in single coats result in periodic density gradients in multilayer films, which may affect film properties such as electrical conductivity or breakdown voltage. Ultimately, understanding and

controlling film inhomogeneities will provide an additional tool to modify the physical and chemical properties of films prepared using the PIC approach.

2.3. Patterning High Resolution Features

In this contribution, results from high-resolution imaging and chemical analysis of thin films and patterned structures of Hf(OH)4−2x−2y(O2)x(SO4)y·qH2O, commonly known as HafSOx.[6] HafSOx is representative of a new approach involving the chemistry of nanosized inorganic clusters for addressing the resolution, line-width roughness (LWR), and sensitivity (RLS) trade-offs that limit lithographic performance of conventional organic materials at resolutions <20 nm.[18,37,38] Dense, sub-10-nm features have already been written with HafSOx using extreme ultraviolet (EUV) irradiation.[39] By examining films and structures derived from electron-beam exposures, we offer new insights into the HafSOx patterning process.

The small spot size and direct-write capabilities of electronbeam lithography make it a convenient method for studying nanopatterning at high resolution.[24] Organic materials, such as polymethyl methacrylate (PMMA),[1,40,41] ZEP-520,[42,43] and related chemically amplified resists,[44] are commonly employed to produce features at resolutions near 30 nm. In such systems, resolution is limited by the large radius of gyration of a polymer chain (2−4 nm) and photoacid diffusion in chemically amplified systems. These characteristics lead to high LWR (2−4 nm), which ultimately limits resolution. Smaller LWRs (<2 nm) have been demonstrated in inorganic materials, notably hydrogen silsequioxane (HSQ),[24,45] but this performance has come at the expense of poor sensitivities and long exposure times. The HafSOx system may offer a path for redefining

the RLS triangle of conventional materials, because small LWRs and ultra-high-resolution features have been realized commensurate with relatively high sensitivities.[18] HafSOx uniquely affords these characteristics, because other Hf-based systems exhibit low resolution[46] and low sensitivity.[47]

The patterning capabilities and radiation sensitivity of HafSOx derive from the presence of Hf-bound peroxo ligands. The absorption of radiation leads to dissociation of the O−O bond of the peroxo group, which drives condensation reactions and a reduced solubility in exposed areas.[37] Unexposed areas of a film may be readily dissolved in an appropriate developer, leaving a negative-tone pattern. The patterning process for HafSOx thus follows that of a conventional organic photoresist, involving some or all of the sequential steps: spin coat, postapplication bake, exposure, post-exposure bake, development, and hard bake. Films and structures derived from selected steps in this flow have been characterized to develop an improved understanding of the overall process. As film thickness and feature size approach 10 nm and smaller, it becomes increasingly difficult to characterize in detail films and patterns using conventional methods, such as scanning electron microscopy.[48] In this study, we have used cross-sectional transmission electron microscopy (TEM) and energy-dispersive X-ray spectroscopy (EDS) to better assess these nanodimensional features. In addition, the high atomic-number elements of the HafSOx system make these techniques especially useful for high-contrast imaging and chemical analysis. Because these characteristics are not commonly present in conventional patterning materials, e.g., organic resists, HafSOx presents a unique platform for studying lithographic patterning at near-atomic resolution.

2.3.1. Experimental

Stock solutions (1 M) were prepared by dissolution and dilution of $HfOCl_2 \cdot 8H_2O$ (Alfa Aesar) and H2SO4(aq) (Mallinckrodt) with 18.2 MΩ purified water. Solutions for spin coating were prepared by adding 30 wt % H_2O_2(aq) (Macron) to the $HfOCl_2$(aq) solution, followed by sequential addition of H2SO4(aq) and 18.2 MΩ water. Final solutions were 0.15 M in hafnium, 0.105 M in sulfuric acid, and 0.45 M in hydrogen peroxide. Solutions were stable against precipitation for approximately 4 days at room temperature (depending upon the concentration) and several months when refrigerated. No change in film quality or reproducibility was observed for films deposited from aged, refrigerated solutions. Prior to spin coating, the substrates were treated with an O2 plasma to improve wetting of the substrate. Films were deposited by dispensing solutions through a 0.45 μm filter and spin coating at 3000 rpm for 30 s. The films were then baked on a hot plate between 80 and 300 °C for 3−5 min. For patterning, films were baked at 80 °C for 3 min. Exposures were performed with a ZEISS Ultra-55 scanning electron microscope operating at 30 kV at a dose of 800 μC/cm2. The microscope was equipped with a JC Nabity writing system for pattern generation. Unexposed and exposed films were soaked or developed at room temperature in 25 wt % tetramethylammonium hydroxide (TMAH, Alfa Aesar) for 30−60 s, thoroughly rinsed with 18.2 MΩ water, and baked at 300 °C for 3−5 min. A J. A. Woollam M-2000 spectroscopic ellipsometer was used to measure film thickness. Data were collected in 5° steps at incident angles covering the range of 55−65°. A Cauchy model was used to extract thickness. A FEI Titan G2 80-200 transmission electron microscope with ChemiSTEM operating at 200

kV was used for imaging and chemical analysis. TEM samples were prepared as cross-sections via focusedion- beam lift-out using a FEI Quanta three-dimensional (3D) dualbeam scanning electron microscope. Approximately 30 nm of amorphous carbon were thermally evaporated on the sample to serve as a protective layer during the lift-out process. EDS line scans were taken in STEM mode, and the areas were correlated to brightfield TEM images that were acquired on nearby locations of the sample to avoid significant damage during STEM operation. The line scans were collected with a step size of 0.15−0.2 nm and then averaged over 1 nm to reduce noise. The scans were analyzed with Bruker Esprit 1.9 software using automatic background subtraction and quantification without standards. X-ray photoelectron spectroscopy (XPS) measurements were performed with a Thermo Scientific KAlpha X-ray photoelectron spectrometer with an Al Kα (1486.7 eV) micro-focus monochromatic X-ray source and ultra-low energy electron flood gun. A 50 eV pass energy was used for high-resolution, element-specific XPS spectra. Spectra were analyzed with an Avantage XPS software package. All peaks were charge-corrected to adventitious hydrocarbon at 284.8 eV, and Au metal was used for energy scale calibration of the photoelectron spectrometer.

2.3.2. Results and Discussion

Cross-sectional TEM images and associated STEM−EDS traces of a blanket-coated, unexposed $HafSO_x$ film (baked at 300 °C) are shown in Figure 8. From the bottom to the top, the material stack consists of the Si substrate, native silicon oxide, spin-coated $HafSO_x$, and carbon/platinum protective layers. A low-magnification image (Figure 8a) reveals that the $HafSO_x$ film is smooth and very uniform. This uniformity is confirmed with a high-magnification image (Figure 8b), which was obtained immediately

upon moving to a new location on the sample. The $HafSO_x$ film thickness, measured to be 12−13 nm from spectroscopic ellipsometry measurements, agrees with the thickness and uniformity observed in these TEM images. Films are observed to change under prolonged exposure to the high-energy electron beam during analysis. A comparison of panels b and c of Figure 8, for example, reveals that the $HafSO_x/SiO_x$ bilayer thickness increases from approximately 15 to 17 nm after a 5 min exposure. In this process, the

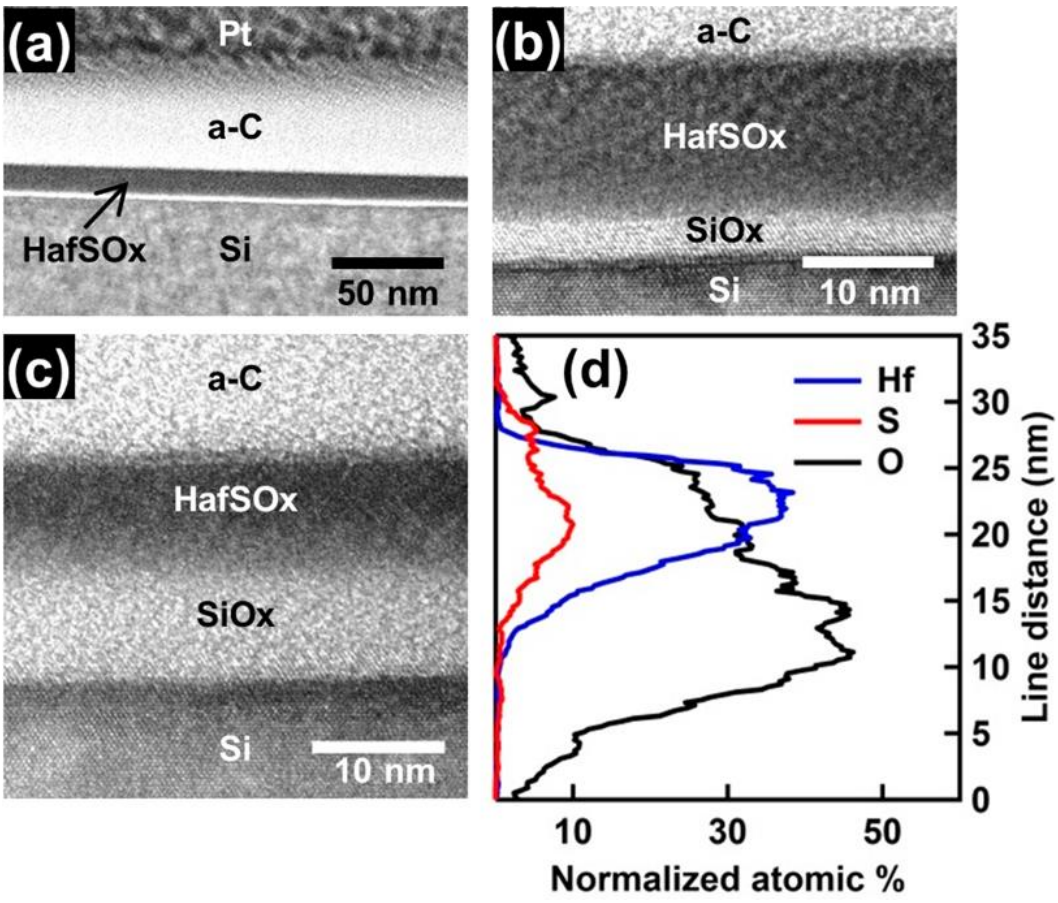

Figure 8: (a−c) Cross-sectional TEM images of the unexposed HafSOx film annealed at 300 °C and (d) STEM−EDS line scan aligned to panel c.

$HafSO_x$ film thickness decreases from 12 to 9 nm, while the SiO_x film thickness increases from 3 to 8 nm. This indicates that the electron beam is driving densification of the $HafSO_x$ layer while promoting further oxidation of the Si substrate. In the EDS line scan (Figure 8d), the S signal is found to track that of Hf, where S as a sulfate appears to be homogeneously distributed with Hf throughout the thickness of the film. This distribution is consistent with imaging results, and it confirms the high uniformity of the films in terms of both morphology and composition.

TEM images and STEM−EDS chemical analysis data of a HafSOx film, baked at 80 °C, exposed at 800 μC/cm^2, soaked in 25% TMAH(aq), and baked at 300 °C, are shown in Figure 9. A low resolution image (Figure 9a) indicates that the resulting film remains uniform and very smooth, similar to that of the unexposed film. From the high-resolution image (Figure 9c), the exposed film is found to be amorphous, and its thickness relative to an unexposed film (Figure 8b) decreases from approximately 12 to 7 nm. From the STEM−EDS line scan, sulfate (S) is no longer present in the film, following the soak in TMAH. These data indicate that electron-beam exposure and TMAH(aq) development have led to the formation of a thin, amorphous binary hafnium oxide hydroxide film. We also found that extended exposure of these films to the electron beam caused portions to crystallize (Figure 9b), producing atomic spacings consistent with monoclinic HfO_2.

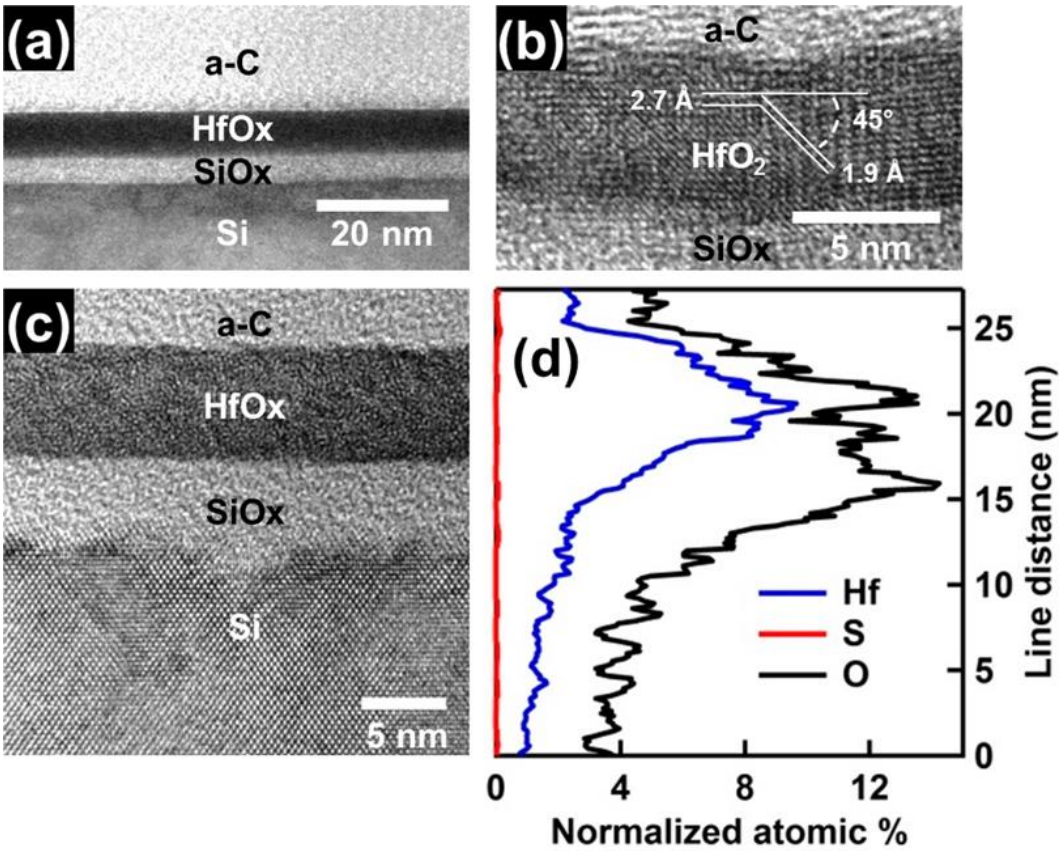

Figure 9: (a-c) TEM cross-sectional images of $HafSO_x$ film exposed at 800 μC/cm^2, soaked in 25% TMAH, and hard baked at 300 °C and (d) STEM−EDS line scan aligned to panel c.

XPS has been used to further elucidate composition and chemical state of the films. Hf 4f, S 2p, and O 1s spectra were monitored at four stages during the patterning process: (i) 80 °C post-application bake (PAB), (ii) 80 °C PAB and electron exposure dose of 800 μC/cm2, (iii) 300 °C PAB, and (iv) 80 °C PAB, exposure dose of 800 μC/cm2, soak in TMAH, and 300 °C post-soak bake. Results are summarized in Figure 10. Only subtle changes are observed in the relative intensities and binding energies of each element following only exposure and baking (80 °C, 80 °C and exposed, and 300 °C). After exposure and soaking in TMAH, however, significant spectral changes have

occurred. For example, the O 1s and Hf 4f peaks shift to lower binding energies, and the S 2p peak is now absent, indicating significant chemical changes, including the loss of sulfate from the film. For the O 1s spectra, the low-binding energy peak at 530.2 eV can be assigned to oxygen bound to Hf as oxide, while the high-binding-energy O 1s peak near 531.8 eV can be assigned to O bound as sulfate and hydroxo groups. Similar assignments have been made previously for Zr analogues of $HafSO_x$.[49,50] For this sample,

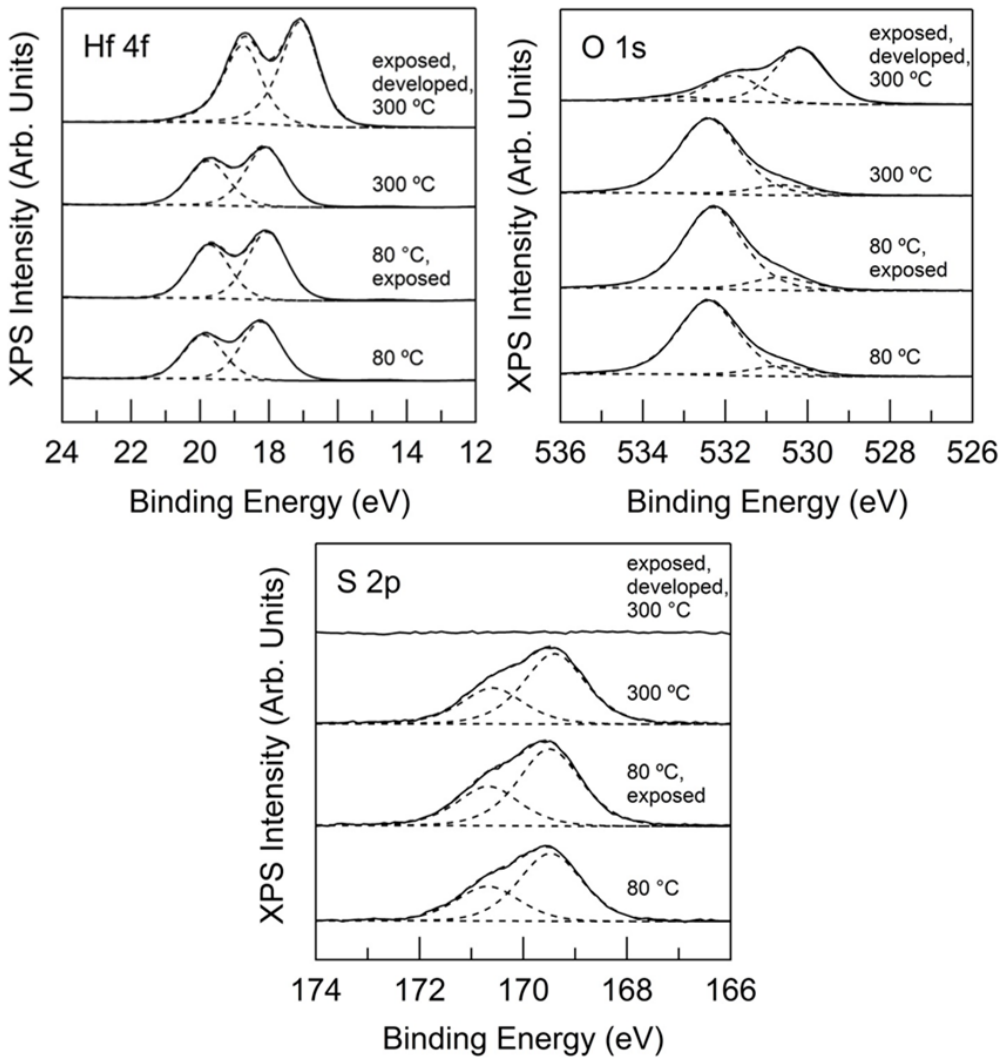

Figure 10: Hf 4f, O 1s, and S 2p X-ray photoelectron spectra of $HafSO_x$ films under selected process conditions.

a third low-intensity peak at 533.3 eV was necessary to obtain an adequate fit; it is assigned to residual water that is present following the development process. This O 1s binding energy is consistent with water adsorbed to metal oxide surfaces.[51,52] We found that the low-binding energy metal oxide component becomes dominant after both exposure and TMAH soak. A similar change in the O 1s spectra was observed after the thermal desorption of sulfate from $HafSO_x$ films in ultrahigh vacuum.[53] While most of the oxygen is coordinated as Hf−O, a significant number of OH groups are detected following the 300 °C bake, which may be partly attributed to surface contamination from exposure to ambient prior to analysis. Together, the XPS and STEM−EDS analyses indicate that a fully exposed and developed $HafSO_x$ film is converted into a hafnium oxide hydroxide product.

We have extended these findings to examine fine-scale patterning of 9 nm wide lines using electron-beam lithography to write the lines at defined spacing by following the same processing steps as those used for the blanket films. A crosssectional TEM image, representing decreasing line spacing from 44 to 11 nm, is shown in Figure 11a. The average full width at half maximum (FWHM) line width is 9.0 ± 0.7 nm. The features are readily resolved to the smallest spacing of 11 nm and a line−line distance of 21 nm. The rounded profiles reflect the modest development contrast of the system.[37] Initially, the as-processed features are amorphous, i.e., similar to the blanket film (Figure 9). After extended electron-beam exposure, the features are found to crystallize as monoclinic HfO2 (Figure 11b). A Fourier transform (Figure 11c) of the atomic-resolved image indicates that the grain is oriented along the [101] zone axis. A very thin layer of residual material containing Hf is consistently observed between the lines, independent of

spacing (Figure 11a). The TEM image of Figure 11b indicates that this residual is 1−2 nm thick and consists of small, discrete structures. HafSOx precursor solutions contain nanosized clusters (diameter ≈ 1 nm), and remnants of individual nanoclusters may become strongly bound to the substrate during the patterning process. At all of the line spacings, secondary electrons can also initiate exposure chemistry.

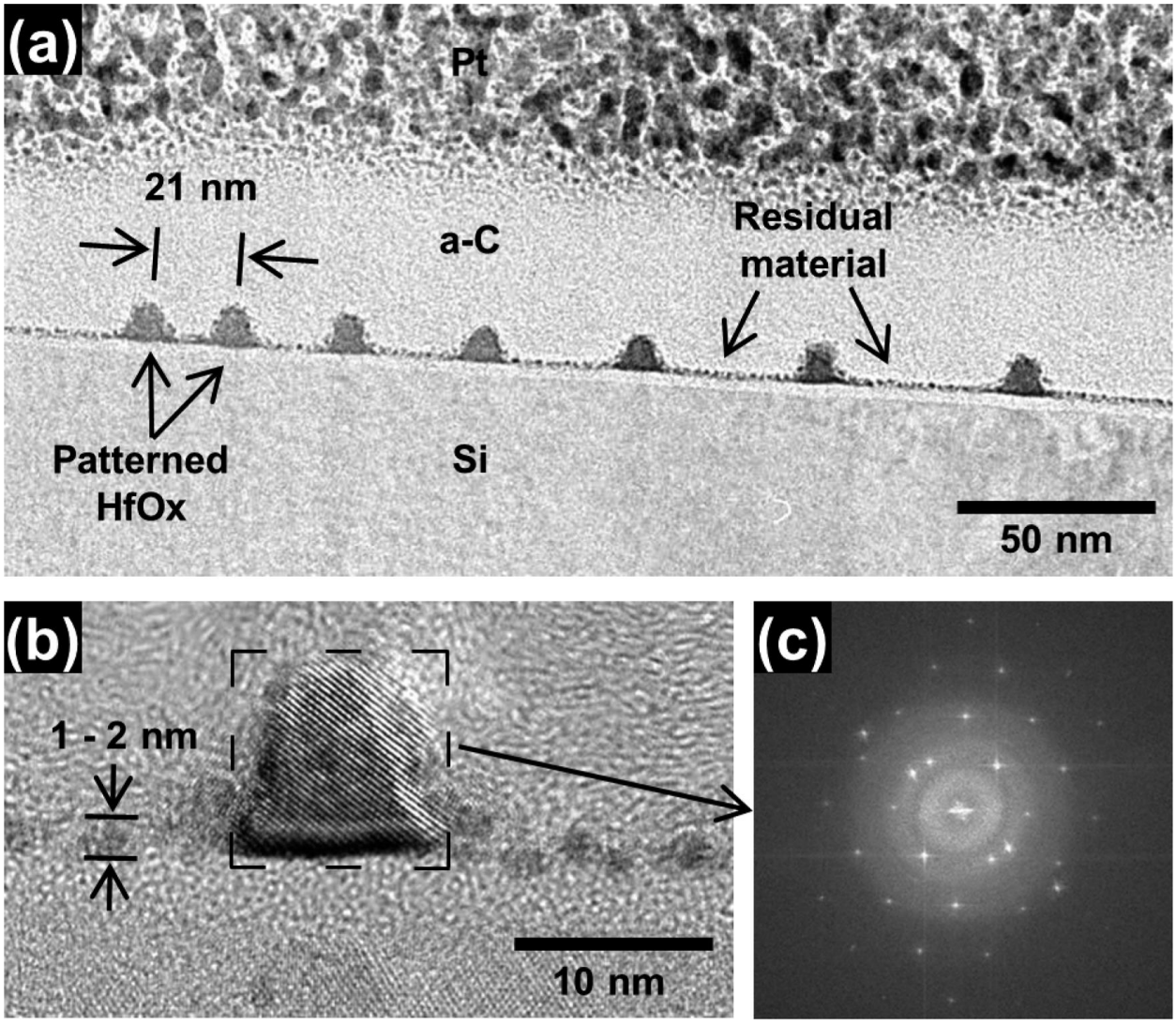

Figure 11: (a) TEM cross-sectional image of an electron-beam patterned HafSOx film after 800 μC/cm^2 exposure and development in 25% TMAH, (b) HR-TEM image of single line, and (c) fast Fourier transform of the region indicated in panel b.

This exposure could enhance interactions between the deposited film and the substrate or simply render these regions insoluble during development. A small increase in residual material thickness is observed at the smallest line spacing, where the thinnest portion is 2 nm. The image contrast is darker and more uniform relative to that of the discrete structures between the more widely space lines (Figure 11b). The buildup and broadening of the profile tails between the patterned lines are likely due to proximity effects associated with scattered electrons.

Overall, the findings can be well-correlated to the chemistry expected for the HafSOx system, i.e., $Hf(OH)_{1.6}(O2)_{0.5}(SO4)_{0.7}\cdot qH2O$. The binding of peroxide and sulfate to Hf in small nanosized clusters inhibits olation and condensation reactions. As demonstrated, exposure to radiation drives peroxide decomposition,[54] inducing condensation reactions that lead to diminished solubility in TMAH(aq). However, this radiationinduced condensation does not lead to full densification, because sulfate remains a mobile species. Because the films are solid acids, they are neutralized on contact with TMAH(aq), resulting in extraction of sulfate. This sulfate is replaced with −OH, which sets the stage for additional condensation. The insolubility of the final product is thus initiated by both radiation and the follow-on development chemistry.

2.3.3. Conclusion

In this study, the utility of high resolution imaging and composition-mapping techniques for examining selected chemical steps has been demonstrated to contributing to the direct patterning of an inorganic material at feature sizes near 10 nm. The techniques have been successfully used to identify key aspects of condensation, sulfate

exchange, and residual formation that contribute to pattern fidelity within the HafSOx system. We expect that the methods discussed herein will provide important information in future studies addressing near atomic-scale characterization of new classes of inorganic materials that hold promise for patterning at unprecedented resolutions.

CHAPTER III

NONTRADITIONAL ELECTRON BEAM PATTERNING AND APPLICATIONS FOR HIGH RESOLUTION PATTERNING

Work in Chapter III has been submitted to be published in ACS Applied Materials and Interfaces; Fairley, K.C.; Sharp, M.; Ditto, J.; Mitchson, G.A.; Johnson D.C.; Johnson D.W., *Low voltage electron-beam lithography of HafSOx films*.

3.1. Chapter Introduction

The chemistry of creating HafSOx thin films has been extensively studied but almost nothing has been reported on the final component, electrons. In this chapter, an extensive look at at non-traditional low voltage patterning was investigated to understand their interaction in the film and how to predict the voltage needed to only expose the film. After the improved patterning technique is demonstrated, some interesting applications for these high resolution, inorganic thin film resists as masks is discussed.

3.2. Nontraditional EBL Introduction

Lowering the accelerating voltage used to pattern a high resolution inorganic thin film electron beam resist, HafSOx, has dramatically decreased the dose required to pattern sub-10 nm lines. Ellipsometry measurements of dose curves created by HafSOx show a dramatic increase in sensitivity without any loss seen in the contrast. High resolution patterning at 10 keV has shown no decrease in obtainable feature size, producing 7 nm wide lines with half the dose required previously and no loss in line edge

roughness. Monte Carlo simulations of the incident electron beam into a 22 nm thick HafSOx film predict that even lower primary beam energies, down to 5 keV, could enable patterning of sub-20 nm features with significantly enhanced throughput. This supports our observation of improved film sensitivity at lower beam energies without loss of patterning resolution.

Improvements in scanning electron microscope (SEM) technology have led to overall performance enhancements across a broad range of common accelerating voltages, including those less than 5 keV.[1] The use of magnetic immersion lenses and stage deceleration have significantly reduced the impacts of aberrations associated with low energy (1-5 keV) beams.[2] This has been vital for studying biological samples in which beam damage is a serious concern. Modern cold-field emission sources, monochromators, and better lenses have improved the low-energy beam performance even further.[1] These performance enhancements have led to an explosion of SEM use in the biological world where beam damage at high voltages has traditionally been a limiting factor.[3] More recently, these advances have been applied to electron beam lithography. [3,4,5]

Electron beam lithography (EBL) performed using an SEM operating at high accelerating voltages, 30 keV and above, has been used extensively for the patterning of densely packed features under 10 nm.[6] High accelerating voltages reduce the spot size of the beam and penetrate deep into thick, dense films to fully expose them.[7] Work has also been done to optimize the chemistry of the EBL resists for use at high voltages, and these efforts to enhance sensitivity have garnered significant recognition. However, high accelerating voltages create several problems for EBL that are exacerbated with the use

of sub-micron films. A significant portion of the energy of the beam passes through the resist and is buried deep in the substrate instead of reacting with the resist.[8] These electrons heat and damage the sample directly beneath the beam and diminish lateral resolution due to long-range proximity effects from secondary electrons.[9] It has been shown in several high resolution resists that decreasing the accelerating voltage leads to an increase in the sensitivity of the target resist.[8,10,11] Due to the enhanced sensitivity, the time required to pattern the resist is dramatically decreased, enabling patterning of larger, more intricate structures while avoiding vacuum damage through drying or condensation effects in sensitive films. If the beam energy is reduced too much, the beam interaction volume may become smaller than the film thickness. This is a problem for full exposure, but has been shown to lead to interesting 3-D stepped structures in positive tone resists.[12] For thin inorganic resists, this suggests that reducing the accelerating voltage to an optimal value may lead to a substantial decrease in patterning time with full resist exposure and minimal impact on lateral resolution.

In this work, we investigate the patterning sensitivity and contrast of HafSOx,[13–16] a negative-tone inorganic electron beam resist, at primary beam energies of 2-30 keV, and the lateral resolution of the resist by patterning at 10 keV. HafSOx was chosen as a model resist because it is thin, dense, and inorganic. Consistent with reports for other thin inorganic resists, the sensitivity of HafSOx increased dramatically as the beam energy decreased. Furthermore, we were able to use 10 keV beam energy to produce sub 10 nm lines without any loss in line edge roughness using only half the dose required at 30 keV. Monte Carlo simulations predict sensitivity enhancements with decreased beam energy in good agreement with our experimental observations. The simulations also suggest that

patterning at beam energies less than 10 keV may still enable patterning of sub-20 nm feature sizes or better as film thickness decreases. This work has implications for improving the throughput of EBL with existing thin inorganic resists while maintaining good lateral resolution.

3.2.1. Experimental

HafSOx film prep: A 1 M stock solution of $HfOCl_2 \bullet 8H_2O$ (Alfa Aesar) was prepared by dissolution and dilution with 18 MΩ nanopure water. Solutions for spin coating were prepared by mixing 2 N H_2SO_4(aq) (VWR) and 30 wt% H_2O_2(aq) (EMD Millipore) followed by the addition of $HfOCl_2$(aq). The final solution was diluted using 18 MΩ water to a concentration of 0.105 M sulfuric acid, 0.45 M hydrogen peroxide, and 0.15 M hafnium. N-type, Sb-doped silicon substrates (0.008-0.02 Ω-cm) received surface treatments using a MΔRCH cs-1701 plasma cleaner running on O_2 plasma at 30% O_2 in N_2 using 150 W for 60 s immediately before spin coating. To obtain more reliable ellipsometry, 100 nm thermally grown oxide silicon substrates were used and treated with SE1 (5 parts 18Ω water, 1 part 39% ammonium hydroxide, 1 part 30% hydrogen peroxide) at 80 °C for 30 minutes before plasma cleaning. Films were prepared by filtering the solutions through a 0.45 μm filter and then spin-coating at 3000 rpm for 30 s. The HafSOx thin films were then subjected to a one minute anneal at 80 °C as a soft bake to densify the films.

Exposure for dose arrays: HafSOx films prepared as described above were patterned in an FEI Helios 600i DualBeam either manually or by using FEI's automation program, iFast. Arrays of 200 μm^2 boxes spaced 400 μm apart were patterned with

accelerating voltages of 2, 5, 10, 20, or 30 kV at a pitch of 60 nm and a dwell time of 100 ns. The number of beam passes across a pattern controlled the dose,

$$Dose = \frac{N \times I \times t}{p_X{}^2} \qquad (1)$$

where N is the number of passes, I is the beam current in μA, t is the dwell time in s, and p_x is the pitch in the X and Y directions, measured in cm. The beam current was measured prior to each experiment using a Faraday cup standard. Films were developed at room temperature in 25 wt% tetramethylammonium hydroxide (TMAH, Alfa Aesar) for 1 min and thoroughly rinsed with 18 MΩ water, followed by a post development hard bake at 300 °C for 3 min.

Ellipsometry measurements: Data was taken on a J.C. Woollam VASE Ellipsometer with focusing probes installed reducing the spot size to 60 μm. Each patterned box was measured at three angles, 55°, 60°, and 65°, with 8 second acquisitions at each angle. The resist was modeled as a Cauchy film on 100 nm SiO_2. All measurements had an MSE value below 10. The squares patterned with doses below the turn-on allow the contrast and sensitivity to be calculated by number of partially patterned squares. A trend line is drawn between the points that lie between a normalized thickness of 0.2 and 0.8, with 1 being completely patterned, striking the x-axis at d_0 and providing a y value of 1 at d_{100}. The slope of the trend line is used to calculate the contrast of the resists and d_{100} is defined as the sensitivity.

Exposure for resolution arrays: HafSOx films were prepared as described above and patterned in an FEI Helios 600i DualBeam. A 10 kV beam with a current of 7.7 pA

was used to pattern high resolution line arrays. An immersion lens was used to decrease the spot size of the probe, lensing through the sample for better resolution. To focus the beam without exposing the resist or moving the stage from the target location, a 2 μm tall platinum-carbon pillar 50 nm in diameter was created by using the electron beam to decompose a platinum-containing gas precursor, $MeCpPtMe_3$. Individual platinum grains were used to confirm the final focus and stigmation without exposing any of the surrounding material. The horizontal field width was set to 61.4 μm, and pattern was then generated from a bitmap using iFast. The pitch, set by the bitmap pixel size, was set at 10 nm, but only a single pass per line was used to allow for the highest resolution.

Line Width and Edge Roughness Measurements: Following exposure, the resolution arrays described above were developed using the same procedure as described for the dose arrays and subsequently imaged with the SEM. High magnification, high resolution images were obtained (1.484 pixels per nm) and analyzed using the freely available ImageJ software. The images were converted to binary format, and the average line widths for six of the lines in the array were obtained over a 700 nm length of each line. The line width roughness was calculated as three sigma of the standard deviation in the line width measurements for each line. The reported average line width and line width roughness were calculated by averaging the values obtained for each line. The line edge roughnesses were calculated in a similar fashion for the top and bottom edge positions of each line. The line edge roughness was calculated as three times the standard deviation in the line edge positions, and then averaged for each line. The line edge roughness we report was obtained by averaging the line edge roughnesses measured for all six distinct lines.

Monte Carlo Simulations: We calculated the point spread functions ("PSFs") of 2, 5, 6, 10, 20, and 30 keV primary beam energies in 22 nm thick soft-baked HafSOx films using the Monte Carlo software CASINO v3.2.0.4.[17] The PSFs represent the implanted energy distribution in the resist as a function of radial distance from the beam irradiation spot.[8] The film density was 4.3 g/cm^3, with an infinitely-thick SiO_2 substrate below the resist. All simulations were conducted using a 1 nm beam spot size and 100,000 electrons. To save on computational power, the implanted energy distributions were output within 100 nm radially from the beam irradiation spot with a 1 nm step size in both *r* and *z* and summed over the depth of the resist to obtain the cumulative PSF in the resist. Contributions from electrons backscattered by the underlying SiO_2 were included in the sampled volume. The default models in the software for secondary electron generation were used. For comparison purposes, we also calculated the PSF for a 10 keV beam incident on a PMMA resist, with 1.18 g/cm^3 density.

STEM Imaging: Cross-sectional images of developed HafSOx lines were acquired using high-angle annular dark field imaging in a scanning transmission electron microscope (HAADF STEM, FEI Titan, 300 kV incident beam). The specimens for cross-sectional imaging were prepared using Ga^+ focused ion beam (FIB) milling and a procedure similar to the Wedge-prep method described by Schaffer et al.[18]

3.2.2. Results and Discussion

Arrays of 200 μm squares were patterned in HafSOx using doses from 1 μC/cm^2 to 1 mC/cm^2 and accelerating voltages from 2 keV to 30 keV to determine the turn-on dose in the resist at each voltage. Planar SEM images (see Figure 1 for an example) were used to identify the approximate turn-on dose for the resist by observing when patterned

material no longer remained after development. The images showed no defects, such as voids or ridges, in the exposed films. Such defects would lead to errors in the ellipsometry measurements used to quantify the thickness of the films to determine sensitivity and contrast. Several arrays were also created using an immersion lens to confirm there was no impact on the sensitivity when high resolution patterns were created. The patterned square edge length was reduced to 80 μm for these arrays due to a reduction in the maximum horizontal field width allowed with the immersion lens active. The immersion lens did not impact the sensitivity or contrast when patterning the resist.

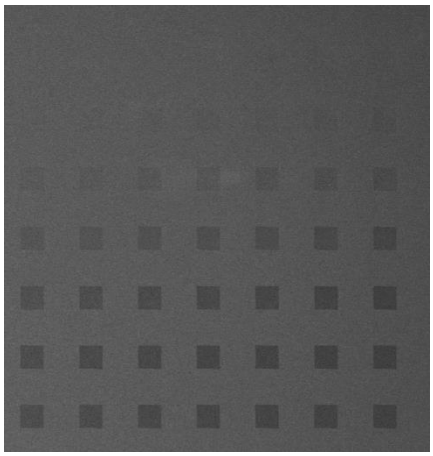

Figure 1: SEM image of an example dose array.

The sensitivity and contrast are both excellent measures of the quality of a resist. Films with high sensitivity require less energy and time to pattern which allows for patterning using instruments that are more economically accessible. Films with high contrast enable close packing of patterned features and sharp sidewalls due to the high separation between patterned and unpatterned material. The completely patterned squares are 9 nm thick and give a baseline for sensitivity calculations. The sensitivity of the film linearly increases (decrease of the d_{100} value) with increasing accelerating voltage, as shown in Figure 2. At 2 keV the time required for full resist exposure is

almost an order of magnitude less than at 30 keV, the beam energy currently used for high resolution lines in HafSOx.[13]

At all accelerating voltages, the contrast values are greater than two. The contrast initially decreases as the accelerating voltage used to pattern the material decreases at 10 keV, but the contrast then recovers at 2 keV. This could be due to the tradeoff from losing the narrow "neck" of the interaction volume at high voltages and reducing the entire "tear drop" that interacts with the film. In the middle where the contrast decreases, the interaction volume is in a regime in the middle and gains the benefit of neither the narrow interaction volume "neck" or "tear drop" interaction with the film (Figure 2). Every accelerating voltage tested was able to produce high resolution lines.

Any resist that has high sensitivity and high contrast is a good candidate for an E-beam resist, but without the ability to pattern at high resolution it is significantly less impactful or relevant with the myriad of well-established low resolution organic resists. To understand the interaction volume of the beam used to pattern the contrast curves and gain insight into the resolution, Monte Carlo simulations were created to model secondary electrons within the film and substrate. As expected from previous results, as the accelerating voltage decreases, the bulk of the electrons are contained within the resist. To further grasp how the beam is contained within the film, PSF analysis was used to understand the width of the beam and how the energy is distributed. The normalized point PSFs of the beam for 2, 5, 6, 10, 20, and 30 keV primary beam energies are shown in Figure 3. The PSF for each beam was normalized to the total energy deposited in the resist by that beam. Because the sensitivity of the resist changes greatly with primary

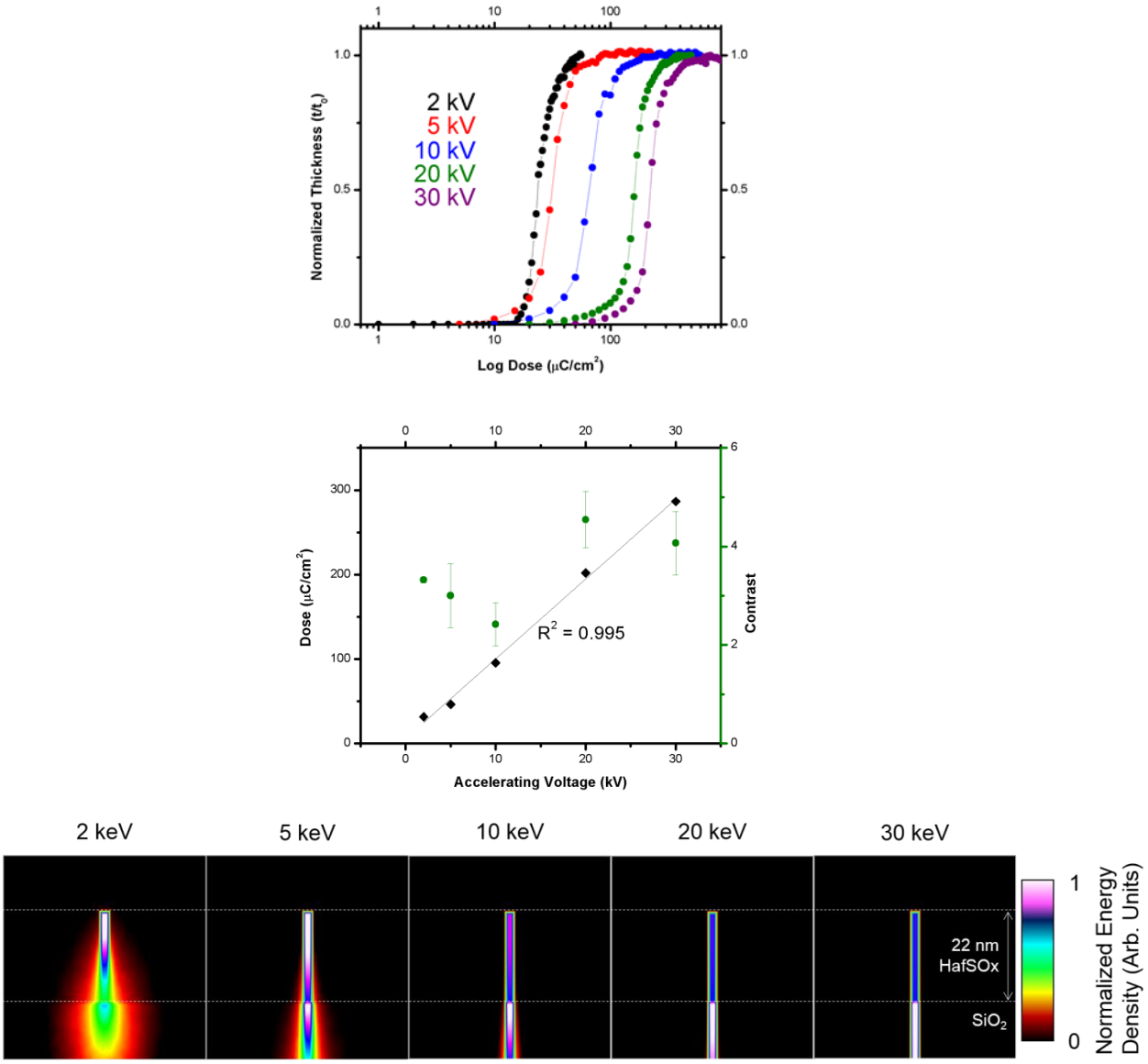

Figure 2: Plotted contrast curves for varying accelerating voltages (Top). Modeled interaction volumes for the corresponding voltages showing the retraction of the "tear drop" to the film (Bottom).

beam energy, this allows a more accurate comparison of how the energy is distributed radially throughout the resist. Integrating the area under each unnormalized PSF provides an estimate for the total amount of energy deposited in the resist. In Figure 4, we show the sensitivity increase relative to 30 keV calculated from our simulations and from our experimental data from the turn-on dose curves. The trend in our simulation results is similar to the trend in our experimental observations: the resist sensitivity increases as the beam energy decreases. For beam energies 10 keV and greater, the simulated and experimental data match closely where there is little beam spread. At lower energies, the theoretical and experimental starts to differ most likely due to an inability to accurately model the contributions from the non-patterned material.

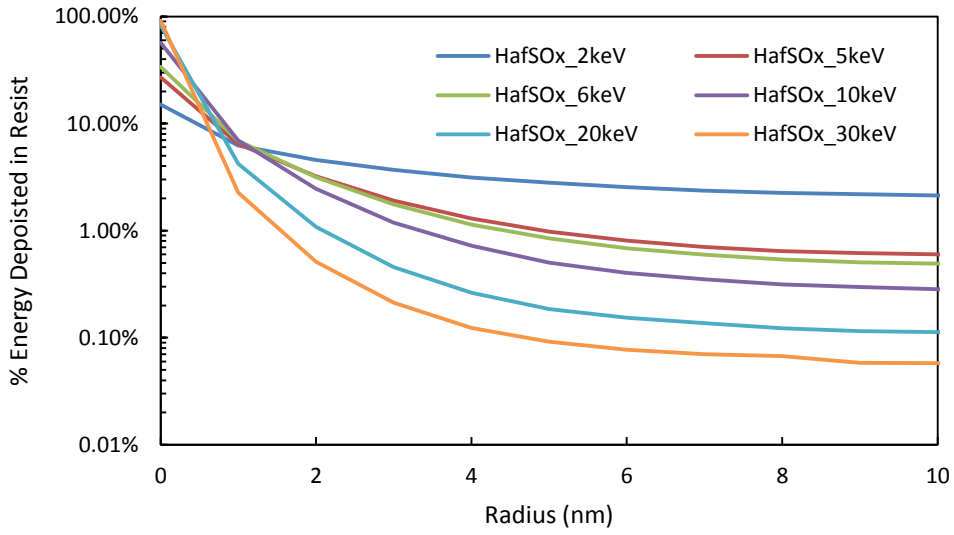

Figure 3: Simulated normalized PSFs for 2, 5, 6, 10, 20, and 30 keV primary beam energies in a 22 nm thick HafSOx resist.

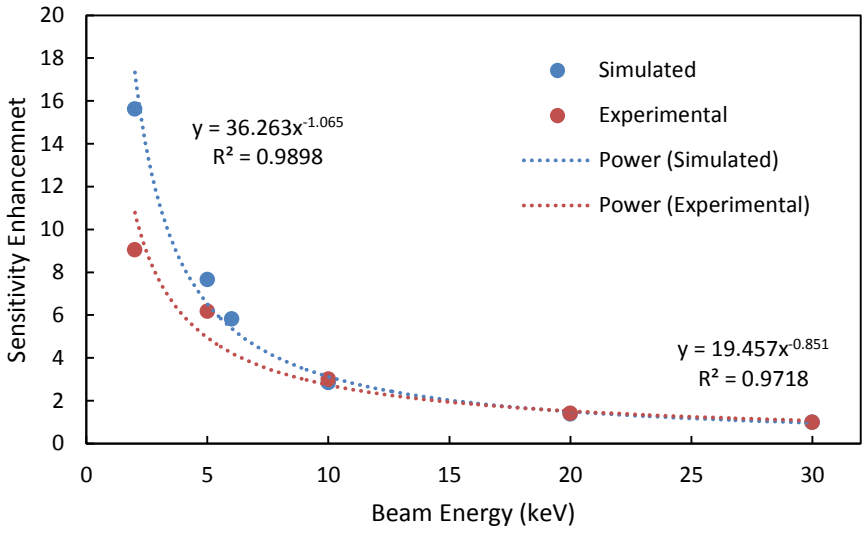

Figure 4: Simulated and experimental sensitivity enhancement as a function of beam energy, relative to 30 keV.

The normalized PSFs in Figure 3 also give some indication of the possible lateral resolution that could be achieved as the beam energy is decreased. As expected, the energy deposited by a 30 keV beam is deposited within a very narrow region through the resist. As the beam energy is decreased, the width of the region in which energy is deposited or exposed increases. The width of the exposed region does not scale linearly with beam energy, but increases rapidly as the beam energy is decreased below 10 keV. Our average line width measurements (vide infra) indicate that at 10 keV the exposure radius of the beam is approximately 4 nm. From our simulations, this radius corresponds to approximately 99% of the total energy deposited in the resist by the 10 keV beam.

To test the resolution of HafSOx at low accelerating voltages, line arrays were created with varying pitch. When patterning with small horizontal field widths, three artifacts produced by the limitations of the instrumentation arose that impeded high resolution measurements, as seen in "3.4. Chapter Supporting Information," Figure 13. At

10 keV high resolution lines were produced with line widths down to 8 nm spaced 35 nm apart, Figure 5. The dose used to create these lines was 488 uC/cm^2, nearly a twofold reduction in the time previously required at 30 keV. As measured from a plan view image, the line width roughness of the 8 nm lines was 2.5 nm and the line edge roughness was 2.63 nm, directly in step with previously reported, high voltage patterning of HafSOx.[13] These results show that high resolution lines that have the same roughness and dimensions of previously reported results can be patterned using lower accelerating voltages in a fraction of the time required to pattern at 30 keV.

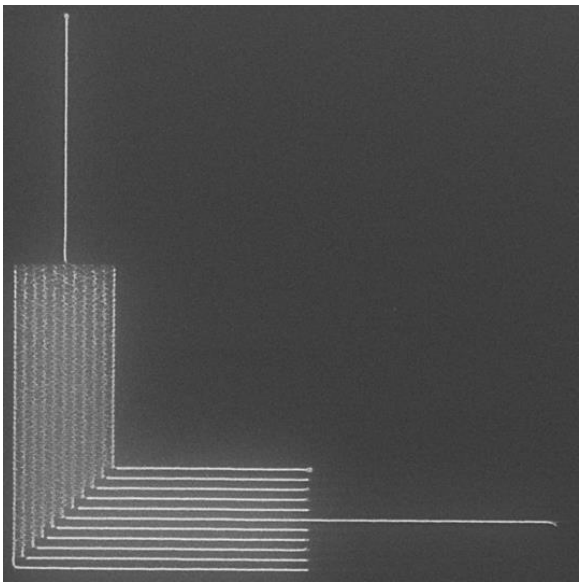

Figure 5: SEM images of patterned 7 nm lines at 10 keV.

After obtaining plan view images of the lines to obtain the line edge and width roughness, cross-sectional STEM gave further supporting measurements of the line height and width. HAADF-STEM images (Figure 6) of a line array patterned at 10 keV show the height of each HfO_2 line, 9 nm, is identical to the film thicknesses determined for the dose arrays after exposure and development using ellipsometry. The images also show a 7 nm full width at half maximum (FWHM), surpassing the previous record for

HafSOx of 9 nm. There is a 1-2 nm residual film between each of the lines that remains after processing, as seen in prior HafSOx studies. The lines are spaced 30 nm apart from each other in an array of 11 lines, giving tight packing along with the high resolution. With moderate contrast, rounded edges appear instead of an ideal top hat shape. The contrast curves indicate that 10 keV accelerating voltage should produce the lowest resolution lines with the highest roughness most likely due to the fact that it does not have the small spot size nor the small interaction volume seen at high and low voltages. Since the results reported above show these factors to be negligible, it is likely that patterning at 2 keV or below should reduce the dose required by an order of magnitude without sacrificing any resolution.

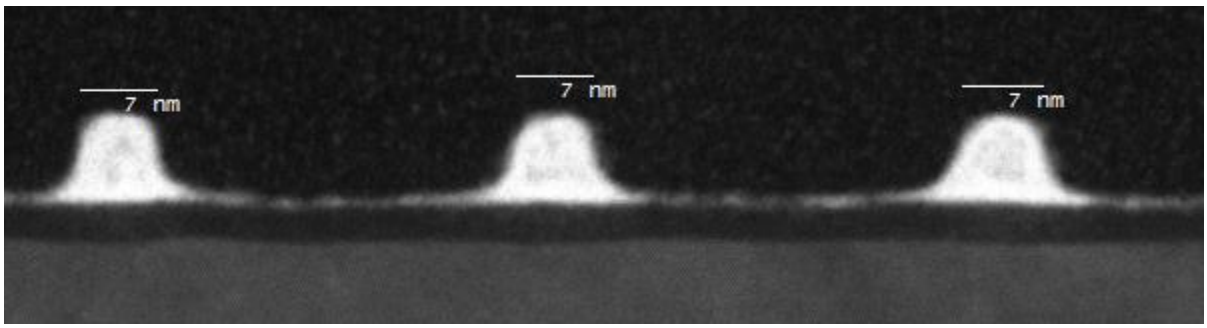

Figure 6: STEM cross-section images of 7 nm lines at 10 keV.

For a 22 nm thick HafSOx resist, 10 keV beam energy appears to provide an acceptable compromise between high resolution patterning and increased resist sensitivity. At very low beam energies, such as 2 keV, the lateral resolution is expected to be much worse than at 30 keV because more lateral scattering of the primary beam occurs in the resist. However, 1-2 keV beam may still enable high resolution patterning in thinner resists, such that only the "neck" of the interaction volume is in the resist.

Since inorganic resists have been able to become incredibly thin, we also simulated the effects of resist thickness using a 10 keV incident beam (Figure 7). Decreasing the resist thickness provides an effect similar to increasing the primary beam energy. More of the energy is deposited immediately in the vicinity of the beam irradiation spot for a thinner resist than for a thicker resist. However, decreasing the resist thickness also leads to less total energy deposited in the resist and a corresponding decrease in the resist sensitivity. These results lead to the implication that as these resists get continually thinner, the ability to go to lower accelerating voltages and faster processing is becoming more feasible without any loss in resolution.

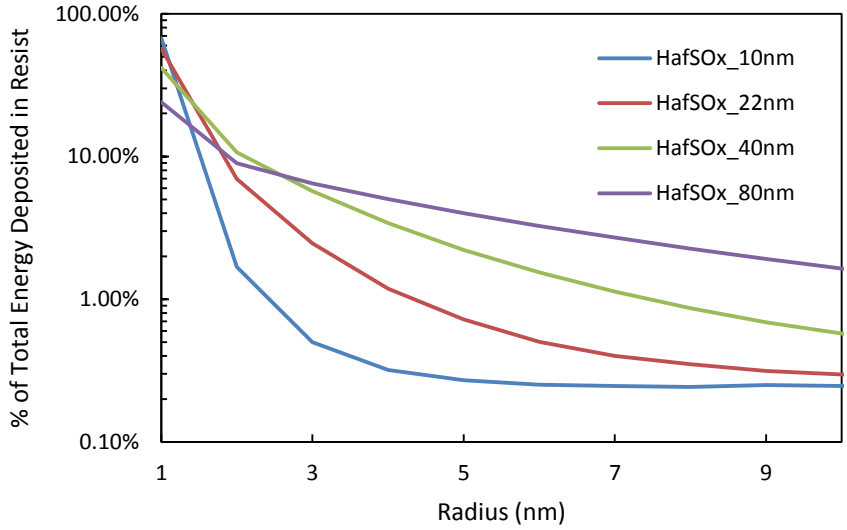

Figure 7: Percentage of total energy deposited in the resist as a function of radius from the beam irradiation spot for HafSOx films of different thicknesses.

In order to understand the effects of traditional thick organic resists compared to the modern thin inorganic resists, both PSFs were modeled. We also compared the normalized 10 keV incident beam PSF for a 22 nm HafSOx resist with that of a 50 nm PMMA resist, shown in Figure 8. Although PMMA is less dense than HafSOx and

scatters the primary beam less, it is more difficult to make in thin layers. Thus, reduced beam energies impact the lateral resolution of PMMA because the body of the interaction volume is partially within the resist.

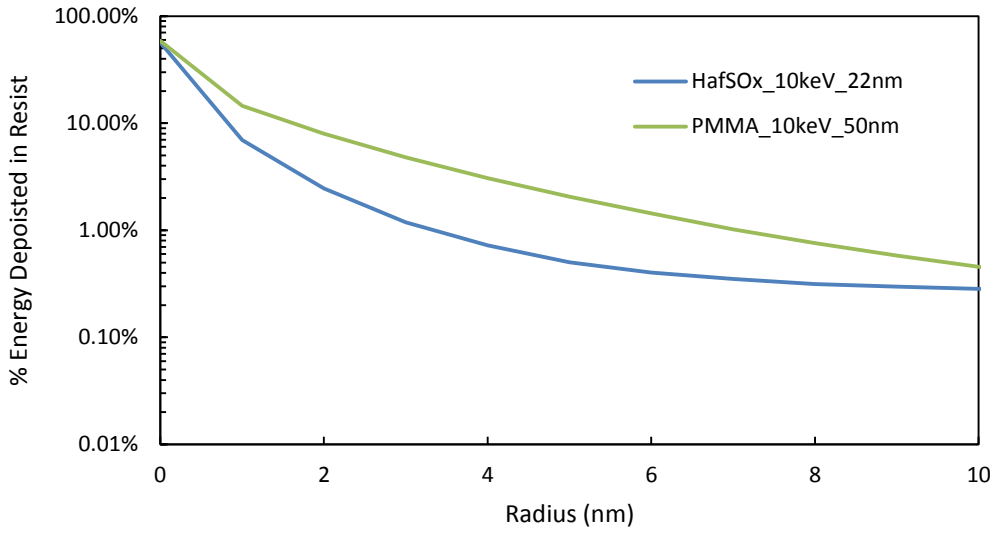

Figure 8: Percentage of energy deposited in the resist vs radius from 10 keV beam irradiation spot for 22 nm HafSOx and 50 nm PMMA resists.

Our simulations indicate that the resist sensitivity increases strongly as the primary beam energy is reduced, in good agreement with our experimental observations. Additionally, our simulations indicate for a 22 nm thick HafSOx resist, 10 keV appears to provide a compromise between good lateral resolution (sub-10 nm) and high throughput (3x relative to 30 keV patterning).

3.2.3. Conclusion

Our results show that reducing the accelerating voltage of the primary beam to 10 keV or less dramatically increases the sensitivity of the film and still enables high resolution patterning. With modern advances in microscopy, such as the various methods of creating magnetic and electric lenses through the film itself, low voltage patterning has

not diminished the resolution nor has the roughness of the patterned material. Sub 10 nm lines are produced using half of the energy previously required with promise to drop process times by as much as nine fold once hardware challenges are overcome. These results suggest EBL should no longer try to maximize the voltage of the incoming electrons, but instead match the energy required to penetrate only as deep as the thickness of the resist.

3.3. High Resolution Resist Applications Introduction

An aqueous inorganic photoresist, $HfSO_x$, was patterned into several fractal arrays using electron beam lithography. These arrays can be built up and converted into metal-oxide hard masks that are able to be used to etch a pattern down into another film or as a conductive gate for thin films above. The fractals have a large range of feature sizes (200 μm to 10 nm) that can be patterned at the same time. This allows for up to eight fractal orders within each pattern which can greatly increase the sensitivity and intensity of fractal devices. These fractals show promise in pushing forward the field of nanoantennas, in demonstrating that high resolution patterning can be retained without sacrificing the fractal order of the pattern, and can be patterned efficiently without lengthy processing steps.

The ability to make devices with conductive fractal patterns has become very advantageous in the field of fractal electronics and antennas. Incorporating exact fractal geometries into the patterned designs has opened the door to new applications that include reduced broadband scattering in photovoltaics[19] and ultrawide band anntenas[20]. Exact fractals are fractals that have a repeating subunit that is exactly the same in every dimension as the original unit as opposed to inexact fratals that are distorted or are

naturally occurring such as a coastline. Among the most famous and widely studied exact fractals are the Sierpinski carpets and gaskets, first described by Waclaw Sierpinski and seen in Figure 9.[21] These exact fractals have been created in the literature using smaller and smaller feature sizes to make many devices including nanoantennas. One of the smallest antennas reported was created using Sierpinski gaskets that had up to three fractal orders with the smallest feature just over 100nm. These antennas allow field enhancement from the THz band down to the visible region using the surface plasmons in the gap of two gaskets.[22] Even with these improvements to currently published nanoantennas, there is still room for higher resolution and incorporation of more iterations of each fractal. To accomplish this, there is a need for smaller feature sizes or increased footprint, but due to limitations in current fabrication techniques these have remained untapped.[23]

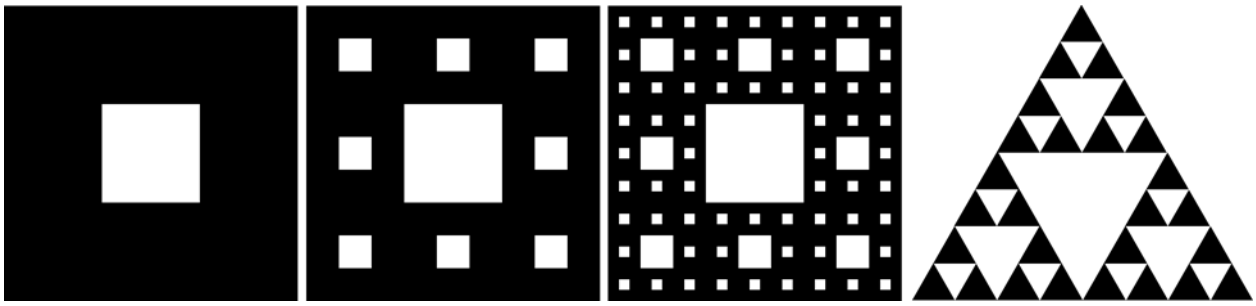

Figure 9: Starting on the left, a first, second, and third order Sierpinski carpet is shown. On the far right, a third order Sierpinski gasket.

One area that is promising for furthering the creation of smaller exact fractals is inorganic photo resists.[13] These resists allow for direct patterning of a fractal array without needing to perform lift-offs, which is a huge hurdle to getting complex features under 100 nm. Another key advantage to inorganic resists that are patterned with electron beam

lithography (EBL) is the versatility that is afforded with the technique itself. EBL removes the need to rely on a physical mask for patterning of the fractals and allows for a variety of exposure doses on the same write. This allows for rapid refinement and configuration of the fractal size and layout for any application that is desired.

One great example is the ability to quickly tune bowtie antennas by adjusting the number of iterations in each fractal and the gap separating each half of the bowtie. It has been shown that gap enhancement in disconnected bowties can be dramatically increased by adding more fractal orders, which allows for a more sensitive plasmonic antenna.[24] Likewise, the magnetic field intensity can also be enhanced in bridged bowties by increasing the number of iterations in the fractal.[25] Since increasing the fractal order will increase the footprint, it is important to be able to tune the pattern in order to take full advantage of tradeoffs between the footprint and feature size. Finally, the Hausdorff dimension, defining how fast a fractal spreads out as each fractal order is added, can be altered with in a plasmonic bowtie antenna which allows for tuning of the resonant wavelength. [26] All of these aspects and physical limitations can be extended or overcome using EBL to pattern hard masks with high resolution without sacrificing for other limitations.

Aside from antennas, another fascinating reason to push the boundaries of fractal patterns is creating interesting electrical devices. The non-regularity of fractals allows for unique effects on current passed through patterns such as Sierpinski carpets by applying side gates to the system.[27] When the flow of current through a uniform device is restricted, the resistance should increase uniformly as well. On the other hand, with a fractal layout, there are gaps that vary in size across the device that lead to large changes

or jumps in the resistance with a very small change in the side gates that restrict the flow of current. This could lead to many exciting avenues including logic gates or the physical detection of charged species that hit the device itself.

3.3.1. Materials and Methods

A 1 M stock solution of $HfOCl_2 \bullet 8H_2O$ (Alfa Aesar) was prepared by dissolution and dilution with 18 MΩ nanopure water. Solutions for spin coating were prepared by mixing 2 N H_2SO_4(aq) (VWR) and 30 wt% H_2O_2(aq) (EMD Millipore) followed by the addition of $HfOCl_2$(aq). The final solution was diluted using 18 MΩ water to a concentration of 0.105M sulfuric acid, 0.45 M hydrogen peroxide, and 0.15 M hafnium. The substrates had surface treatments using an O_2 plasma at 30% O_2 using 150 W for 30 s immediately before spinning. Films were spun by filtering the solutions through a 0.2 μm filter and then spinning at 3000 rpm for 30 s. The samples were then subjected to annealing at 80 °C for one minute to drive off solvent and densify the film. The thickness of these films was 15-17 nm as measured by cross-sectional SEM and XRR.

The thin film was patterned via electron gun in a Zeiss Ultra-55 scanning electron microscope. The beam was run at 30 kV through a 7.5 μm aperture. The patterning was done with Nanometer Pattern Generation System (NPGS) software that used a CAD file which was composed of individual squares, as seen in Figure 10, placed together to make the overall fractal pattern. These squares were patterned with a line spacing of 2 nm and an area dose of 800 $\mu C/cm^2$. Each individual square was patterned stitching together the entire fractal. A benefit of

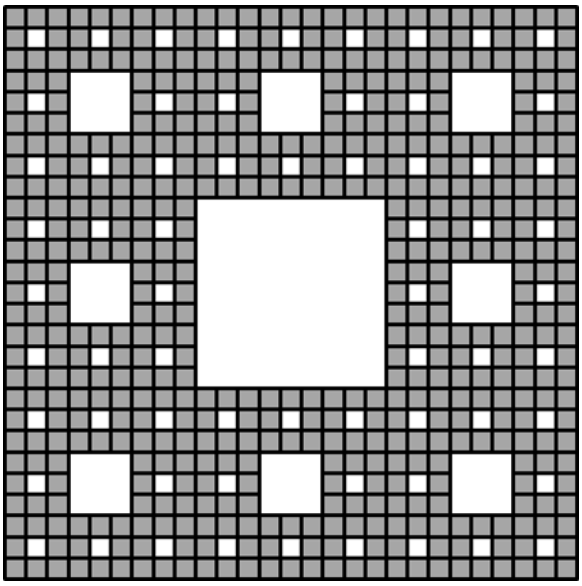

Figure 10: An example of what a CAD file used to create a third order Sierpinski Carpet would look like. The system patterns everything within the lines of each individual box (the grey shaded area), leaving the rest unexposed.

patterning this way is that each square can be made into individual layers, allowing variation in the exposed dose which prevents over exposing congested sections within the fractal. After patterning, the films were hard baked at 300 °C for 3 min on a hot plate to convert the patterned film to hafnium oxide.

One of the first fractal patterns created was a Sierpinski carpet as shown in Figure 11. The smallest feature in the figure is a 15 nm well, but features as small as 10 nm have been created on fractals with smaller footprints. Eight of these 15 nm wells surround a 45 nm well making up the first iteration of the carpet. For each fractal order, the previous iteration is repeated eight times around the new well until the entire fractal is created, which spans over 100 μm. These fractals can then be covered with a conductive material or etched down into another substrate to create an electrical device as mentioned above.

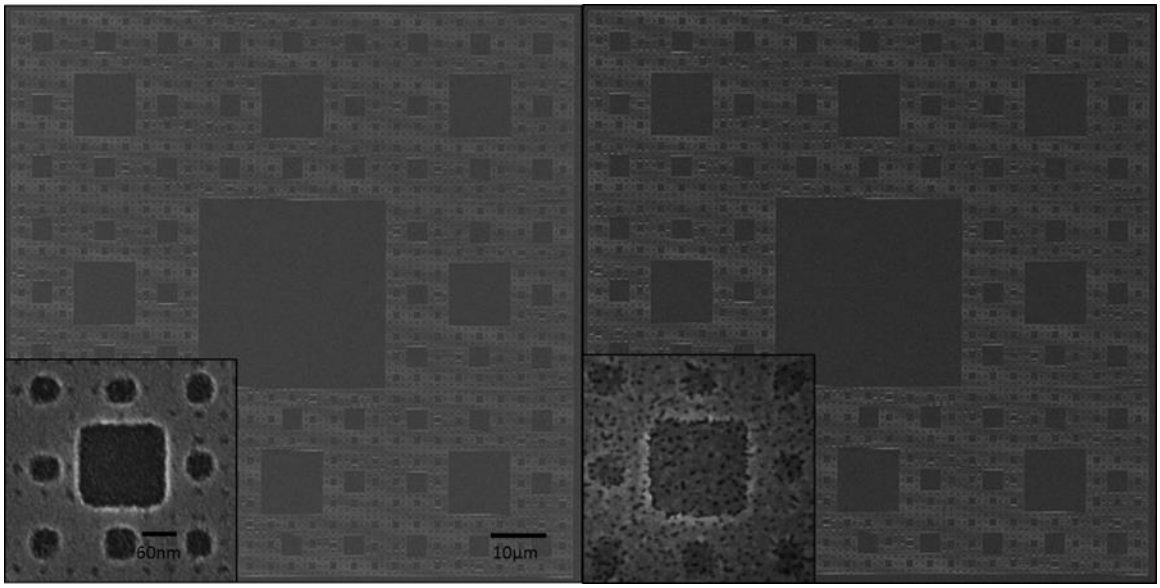

Figure 11: An eighth order fractal is shown on the left that ranges from 100 µm overall size, down to 15 nm wells shown in the lower left. On the right is a fractal with the same dimensions covered with 5 nm of gold making a conductive fractal textured surface.

It can be seen that smaller features can get lost once the gold is applied but the next larger set of features do clearly remain. This is most likely due to the grain size of the gold on the surface which is the limiting factor for building up the device. Since hafnium oxide has such high resistance to dry etching, it would be amenable to making a device down into a conductive substrate with little undercutting unlike other, softer inorganic hard masks.

One fractal pattern that is more amenable to gold coating is the second family of fractals created, the Sierpinski gaskets, seen in Figure 12. This fractal has ten orders of magnitude and even retains the 18 nm bridges that connect each of the smallest patterned features. This can be doubled with a 10 nm gap between the two fractals to make the fractal nanoantenna.

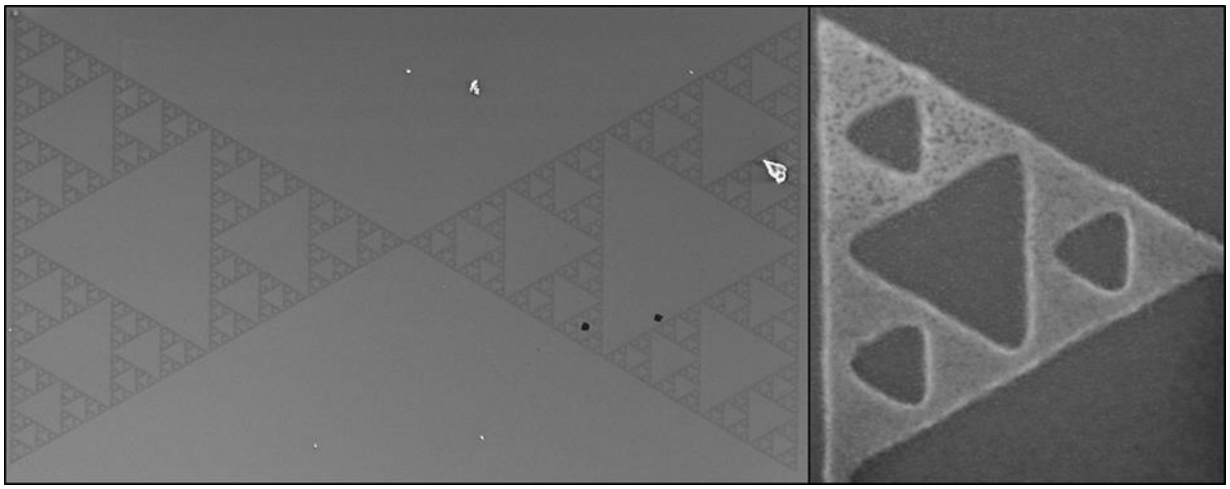

Figure 12: A Sierpinski gasket is shown ranging from 100 μm on the left to 50 nm features shown on the right. This fractal covers ten fractal orders of a triangular void surrounded by three triangular patterned areas. The bridges connecting the patterned triangles are all 18 nm in width.

3.3.2. Results and Conclusions

In this work, fractal patterns have been created that have features ranging from 200 μm to 10 nm. With this versatility, it has allowed for fractals with eight to ten fractal orders to be constructed. These fractals include Sierpinski carpets and Sierpinski gaskets that could have significant implications in creating a nanoantenna or electrical devices that could allow for even broader enhancements to the field of fractal electronics. The resist used to make these patterns is adaptable, allowing for the patterning of very large patterns without losing the small features on the nanoscale.

3.4. Chapter Supporting Information

Three distinct artifacts were observed when patterning, seen in Figure 13. The first is a small dot in the upper right hand corner of the desired pattern. This is believed to be the resting position of the beam due to the spherical nature of the artifact. The second artifact is a bar along the top of the field of view and is proportional to the horizontal

field width. The third artifact is a box that is anywhere on the field for view and also proportional to the horizontal field width. All three of these artifacts are seen when the stage is moved to a new location and patterning occurs without rastering. This is most likely due to a lack of a fast beam blanker but can be overcome by making the horizontal field view large and diluting the artifact electrons beneath the energy required to cause condensation within the film. To reduce the impacts from these artifacts, the horizontal field width was expanded to 61 μm, and the pixel size was set to 10 nm at a field resolution of 6k. This removed all defects except the dot that is related to the parking position of the beam during patterning. These strategies were only successful for high resolution patterns that used 10 keV or higher; otherwise the film was so sensitive that the artifacts persisted. Patterning high resolution features using less than 10 keV is currently not possible due to the horizontal field width required to no longer see the artifacts.

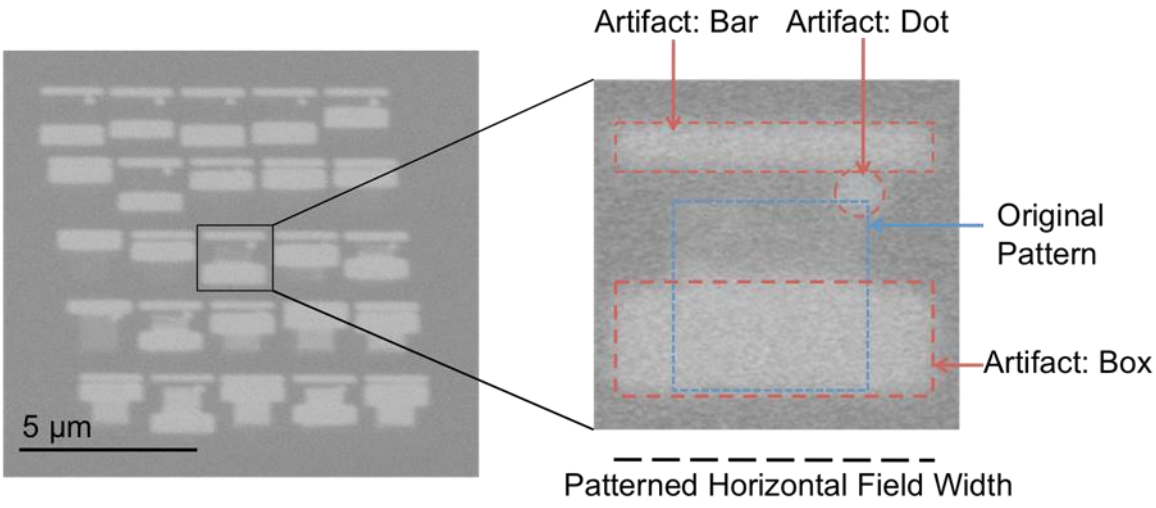

Figure 13: Image of a 5x5 does array with three distinct artifacts. The "Bar" and "Box" both reflect the horizontal field width used to pattern and the "Dot" is the resting position of the beam in between each pass.

CHAPTER IV

FRACTAL TOP CONTACTS FOR NEURON BINDING STUDIES

Work in this chapter has not been published but data may be included in future publications on neuron binding in 2016. Co-authors could include, William Watterson, Rick Montgomery, Darren Johnson, and Richard Taylor.

4.1. Chapter Introduction

One of the most basic and powerful senses people use to navigate their daily lives is vision. This is accomplished by light entering the eye and being absorbed by photoreceptor cells called rods and cones. After the photons are absorbed, they cause a change in the electric potential of the membrane generating a signal that is relayed to the brain. This is accomplished by the neurons directly connected to the retina responding to the field, causing a chemical shift. The path to the brain is long, and one of the most critical steps in this process is transmission from the photoreceptors once they are generated.[1]

Retinal damage can cause many photoreceptors to cease functioning, breaking the chain and leading to loss of sight. Once the eye cannot collect light, there is no way to form any signals the brain can understand, resulting in the person becoming blind. Total blindness is a problem that affects thirty-nine million people in the world today.[2] There have been large strides in developing new surgeries that can correct problems such as

cataracts, which account for over fifty percent of people who are legally blind, but this has not solved the problem entirely. Unfortunately, diseases such as AMD (age-related macular degeneration) and RP (retinitis pigmentosa) have led to a loss of function in the photoreceptors, and with RP there is no effective treatment for the loss. This affects over one million people worldwide and is a prime candidate for the new emerging technology of artificial retina.[3]

Sub-retinal artificial retinas have very powerful implications that arise from avoiding the necessity of repairing damaged biological material, sidestepping it altogether by replacing it.[4] This allows for photodiodes or other light sensitive materials to be placed into the eye, collect the incoming photons, and convert them into electrical signals for the brain to interpret. By implanting artificial retina, millions of people can regain the vision they lost to diseases that destroy the receptors in the eye such as RP and AMD. The layout of the sub-retinal artificial retina includes a photodiode as its core component that can take in the photons and convert that into an electrical potential. The second component is the interface, as it is critical that the signals generated by the receptors are transitioned into the biological system or nothing is accomplished.

The most mature and widely used clinical solution is an external device that uses a camera to collect light outside of the body and then transmits intense, focused beams into the eye or with wires directly stimulates the neurons themselves.[1] The popularity of these external devices is due to a lack of efficiency in the current sub-retinal methods using inefficient square top contacts of the photodiodes, which does not provide enough energy into the device and onto the neurons. The loss stems from the lack of adhesion neurons have with the top contact, along with insufficient light passing through the top

contact and striking the photoactive material to generate a signal. Overcoming these problems removes the need for any exterior devices that can be bulky and intrusive.[3]

One current method to overcome these barriers is to use functionalized carbon nanotubes which both allow for adhesion of neurons[5,6] and allow light to pass through the mesh to the active material, generating a current. Once the current is generated, it is able to travel through the matrix of nanotubes and generate the field required to affect the neuron. The significant hurdle to this approach is the random nature of the nanotubes themselves, making it more difficult to determine where the photon hit from the emission alone. Photodiodes covered with square top contacts have also been used that feature the sensitivity of a well-defined surface and high conductivity due to the basic materials used.[7] Since a large flat material is employed, light is unable to pass through, and the final footprint of the entire artificial retina must be larger to still collect enough signal to create a field the neurons can detect.

Moving forward, combining the two styles by placing a fractal top contact on top of an active material will be incredibly beneficial. Fractals by nature have a large amount of empty space that will allow light to pass through but are entirely connected making a continuous structure, which generates a uniform field throughout the entire device. The open, weaving structure mimics that of the nanotubes taking advantage of all the benefits the structure offers along with allowing high reproducibility. Varying the sizes of the features also allows for neurons to adhere much more readily due to having large hand-holds or binding areas to grab onto but also small cavities that capture nutrients the neurons seek out. By placing the fractal top contact onto a large continuous photodiode, the amount of surface area that can react with photons is greatly increased and therefore

allows much more light to be collected and transmitted to the neurons and a smaller footprint.

In this work, it is hypothesized that neurons, fractal in nature, will preferentially bind to fractal texturing as opposed to smooth surfaces. To test this, fractal textures are fabricated using thin film resists patterned via scanning electron microscope (SEM). Several different fractals were chosen alongside controls that will determine whether the neurons are attracted to the fractal nature of the structure or simply drawn to a defect in the surface. These structures have neurons cultured on the surface, and after staining, any preferential binding is observed via fluorescent microscope.

4.2. Experimental

The initial samples produced in this study were fabricated from a HafSOx resist.[8] The films were created using a 1 M stock solution of $HfOCl_2$ • 8H2O (Alfa Aesar) prepared by dissolution and dilution with 18 MΩ nanopure water. Solutions for spin coating were prepared by mixing 2 N H_2SO_4(aq) (VWR) and 30 wt% H_2O_2(aq) (EMD Millipore) followed by the addition of $HfOCl_2$(aq). The final solution was diluted using 18 MΩ water to a concentration of 0.105M sulfuric acid, 0.45 M hydrogen peroxide, and 0.15 M hafnium. The substrates were 10 x 10 mm and were scribed into four quadrants on the back for future cleaving. This was done to obtain a final size of 5x5 mm for neuron culturing but reduce the edge effects from the spun film. The wafers had surface treatments using a MΔRCH cs-1701 plasma cleaner running on O_2 plasma at 30% O_2 in N_2 using 150 W for 30 s immediately before spin coating. Films were spun by filtering the solutions through a 0.45 μm filter and then spincoating at 3000 rpm for 30 s. The thin films were then subjected to a one minute anneal at 80 °C.

The patterns for the initial samples were created using a Ziess Ultra-55 scanning electron microscope with a 30 kV accelerating voltage at 7.5 pA. Each individual pattern was created in Design CAD and imported into Nanometer Pattern Generation System (NPGS) software where each pattern was spaced out 500 μm from each other making up a 5 x 5 grid. The array was patterned in the center of one quadrant to minimize any damage from cleaving at a dose of 800 $\mu C/cm^2$. To develop the patterns, the samples were soaked in 25 % tetramethylammonium hydroxide for one minute followed by a thorough flushing of the surface with 18 MΩ water. Converting the pattern to a hard oxide was accomplished by heating at 300 °C for three minutes. With the rigid pattern in place, the surface was protected with wafer tape and cleaved into 5 x 5 mm sections.

The majority of the samples were created using SU-8 photoresist. Silicon wafers had surface treatments using a MΔRCH cs-1701 plasma cleaner running on O_2 plasma at 30% O_2 in N_2 using 150 W for 30 s immediately before spin coating. The surface was flooded with SU-8 2002 and spun at 500 RPM at a ramp rate of 100 RPM/s for 10 s to make a uniform coat. The spin rate was increased to 2000 RPM at a rate of 200 RPM/s for 60 s to reduce the final film thickness to ~2 μm. A soft bake of 65 °C for 4 minutes ramping at 450 °C/hour followed by 95 °C for 8 minutes ramping at 120 °C/hour and finally cooled to 45 °C at a rate of 120 °C/hour was done to densify the film without causing any cracking from thermal shock.

The patterns for the remaining samples were created using a Ziess Ultra-55 scanning electron microscope with a 30 kV accelerating voltage at 7.5 pA. Each individual pattern was created in Design CAD and imported into Nanometer Pattern Generation System (NPGS) software where each pattern was spaced out 2 mm from each

other making up a 4 x 4 grid. The resist was patterned at 1 μC/cm^2 allowing for the smallest features to become fully exposed. A post exposure bake started the cross-linking of the polymers by heating to 65 °C for 1 minute ramping at 450 °C/hour followed by 95 °C for 8 minutes ramping at 120 °C/hour and finally cooled to 30 °C at a rate of 120 °C/hour. Removal of unreacted material was done by soaking in 1-methoxy-2-propanol acetate (microchem) for one minute and rinsed with isopropyl alcohol and dried with nitrogen. The final anneal was done at 450 °C for 10 minutes with a ramp rate of 450 °C/hour and then cooled to 45°C at a rate of 120 °C/hour.

Retinal neurons were cultured from 3 day old neonatal mice as described previously.[9] Briefly, the retina was removed from the outer epithelium and placed in the culture medium. The retina and culture medium were mechanically agitated to separate the neurons and then passed through a 20 μm filter to remove cell dendrites. After 3 days in culture, the substrate and surviving cells were rinsed and stained. Cells were stained with DAPI, GFAP, and β-tubulin III. DAPI fluoresces blue and fixes to cell nuclei, GFAP fluoresces green and attaches to glia cells, and β-tubulin III fluoresces red and binds to microtubules in neurons. Cell counts were obtained from fluorescent DAPI images by thresholding the image and counting the number of cells using ImageJ.

4.3. Results and Discussion

The initial attempts to create structures that bind retinal neurons used patterned HafSOx films. Using high resolution resists are advantageous for getting extremely small feature sizes but do not allow for a relatively large overall footprint due to the low sensitivity of the HafSOx. Since neurons have many fractal orders themselves it is

thought that having textures to match is advantageous. HafSOx allows for features well below 100 nm and a footprint up to 100 μm allowing for seven fractal orders to be patterned. The large range of feature size not only allows for ample binding sites as previously mentioned but also permits a large amount of light around the patterned material to a photodiode below. This allows for a larger top contact in respect to the photodiode without sacrificing the amount of energy absorbed into the active material as seen in Figure 1.

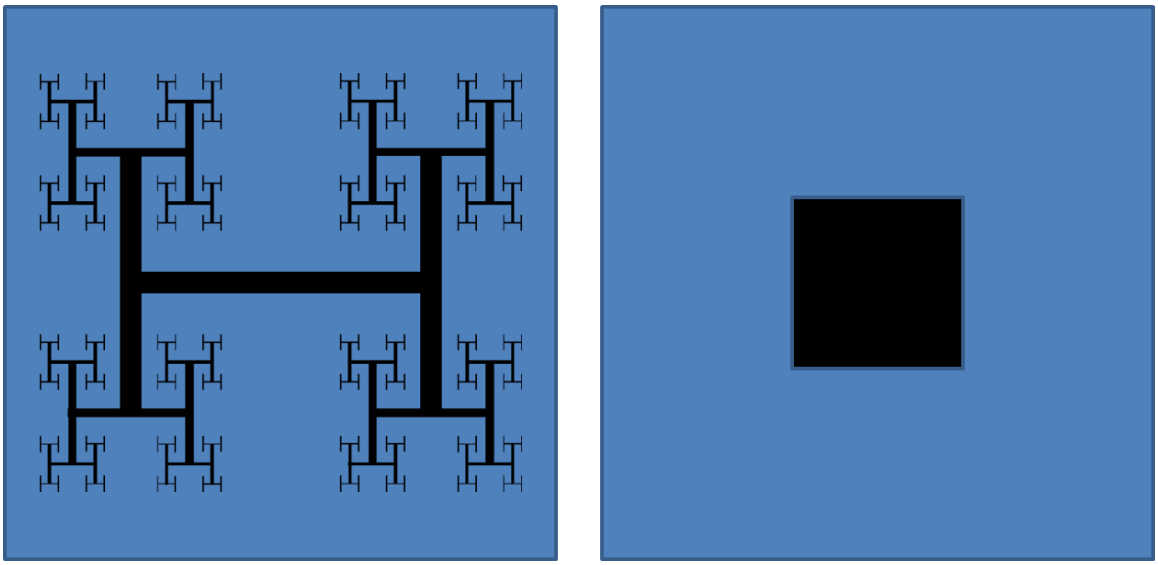

Figure 1: An H-tree fractal (left) and basic square (right). The fractal nature allows the H-tree to have a footprint 6.8 times larger and still have the same amount of exposed active material.

The largest physical challenge in fabrication of the test samples was substrate manipulation. To culture cells on the wafers, the physical size of the chip was limited to a 6 mm square. Edge effects from the spinning process become prohibitive at these sizes so it became necessary to break down the wafers after patterning, which led to silicon dust on many of the tiny samples or caused the substrate to cleave through the fractal surface texture destroying the samples.

In the first set of samples four fractals were chosen along with two non-fractal controls, seen in Figure 2. Design CAD was used to create each layer of the fractal as a unique entity. This allows for the independent patterning of each fractal order to reduce over exposure and retain the desired feature size. High resolution SEM images of the fractal patterned material confirm the smallest features (18-30 nm) have been successfully created without being washed out. To retain the highest resolution possible, each pattern was created individually and then the stage moved to a new position before starting on the next CAD file.

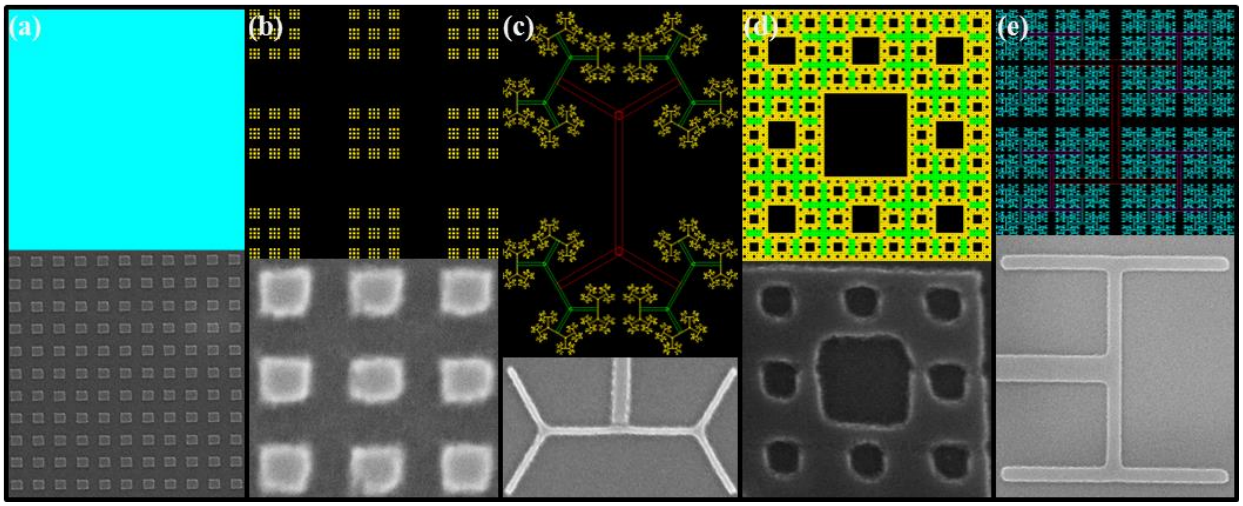

Figure 2: On top are CAD files of the entire pattern: a) non-fractal pillars (which are unresolvable at low magnification), b) fractal pillars, c) bent h-bar, d) Seirpinski Carpet, and e) H-bar. On bottom are SEM images showing the smallest features of the corresponding CAD files above, from left to right, 78 nm, 31 nm, 18 nm, 30 nm, and 71 nm. The square control was omitted from this figure.

The first two fractals took advantage of hills or valleys to gain favorable interactions with the neurons, relying heavily on ridges to play an important role in neuron binding. The H-bar (blue circle in Figure 3) and bent H-bar fractal (red circle), composed of a single large raised “H” surrounded by four smaller “H”s on each corner, centered on a terminal point and continued on in a fractal manner. These patterns created large raised

ridges and took advantage of these raised “hills” to capture neurons that might sweep across and latch onto the structure. The third fractal, the Sierpinski carpet (green circle), was composed of a large valley surrounded by eight smaller valleys, repeated over and over in a fractal manner. These patterns took advantage of lowered dips within the pattern to allow small nutrients to collect, creating a driving force for the neurons to migrate on top of the pattern. When comparing the two classes of fractals, neurons tended to respond better to raised structures when compared to cavities, which indicated that the H-bar fractal should get more favorable binding than the carpet. The preference for raised structures has been shown in previous work by using tall pillars for successful interactions with neurons but the mechanism is still unknown. With both the H-bar and Seirpinski carpet patterns densely packed, the more disperse H-bar 120 fractal was used which didn’t pack as tightly. The loose design was thought to give more access to the textured surface allowing for more interactions with large neurons but trapping fewer nutrients within the fractal architecture. These two groups of fractals are meant to illuminate which driving force has the most impact to neuron binding.

To control for any non-fractal binding accruing with the neurons, both an evenly distributed field for pillars (white circle) and a group of pillars with fractal separations (purple circle) were used. These two controls allow for interactions with the neurons that have been shown to be favorable, to validate the experimental conditions but also grant a direct comparison between fractal and non-fractal structures composed of the same basic building blocks. The final pattern used was a flat square (black circle) of HafSOx with the same footprint as the rest of the patterns as a control for the material itself. Each of

these patterns were made out of a resist that has not been used to study neurons before, as it was important to show that the material itself is not affecting the binding in any way.

With the limited number of data points each sample could produce, it was imperative to create a statistically diverse array. To do this, patterns were chosen and dispersed as evenly as possible to try and reduce any influence from their neighbors, as seen in Figure 3. The beneficial binding of one pattern could lead to a cooperative effect that increases the local binding or crowds out competitors. The lack of binding could affect the local environment as well, leading to a deficit that the surrounding patterns could take advantage of or be hindered by due to a lack of cooperative efforts. Randomizing the patterns will shed light onto these effects.

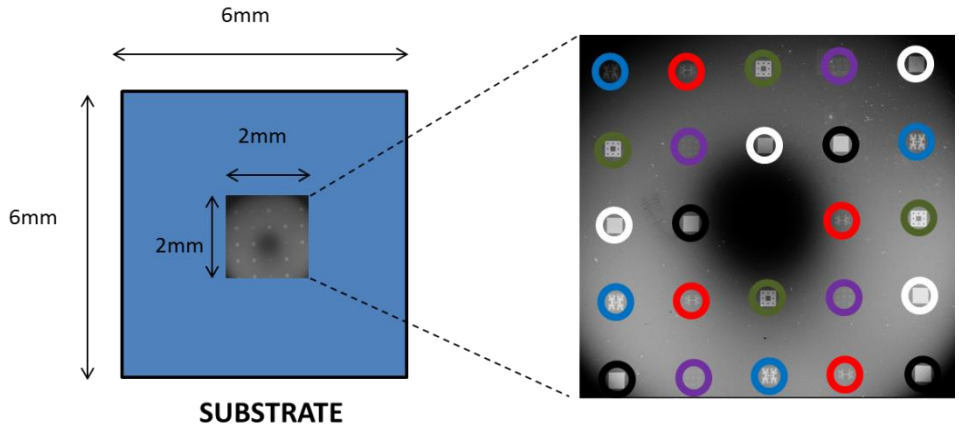

Figure 3: Chip layout containing H-bar fractals (blue), bent H-bar fractals (red), Seirpinski carpets (green), fractal pillars (purple), non-fractal pillars (white), and square (black).

To study the surface interactions of the neurons, they were cultured using a three step process. To start, a stock of mice that had been raised in the lab from a single father were

euthanized. Their eyes were harvested and the retina was removed by dissection. Finally, the retinas were dissociated and the relevant cells were collected. After the cells had been culled out, they were placed in a growing medium with textured substrates and allowed to grow over several days. After the growth period, the cells were fixed on the wafers and stained with fluorescent dyes for easy imaging. Three dyes were used, GFAP, β-tubulin III, and DAPI, marking the glial cells (green), neuron cells (red), and nucleus (blue) respectively.

The initial results from the HafSOx samples showed no preference to the fractal texturing as opposed to the controls or the bare surface, as seen in Figure 4. There is very even coverage of the neuron cells (red) indicating the neurons can't detect any beneficial or harmful areas over the entire substrate. The nuclei (blue) are spread out as well, matching the cell stains. There is a slight preference to the right side for the glial cells

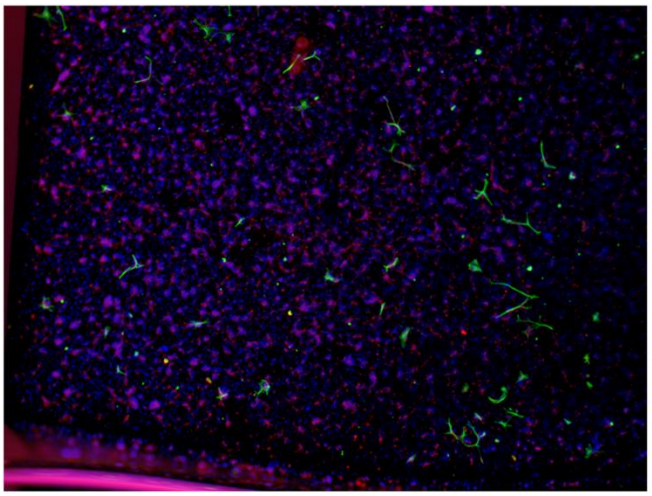

Figure 4: Fluorescent images from the first round of samples sent over to Lund, made with HafSOx.

(green) but it does not correlate to any patterns. The HafSOx patterns are well under 100 nm thick and are likely too small to interact with the neurons or trap any nutrients the neurons seek out, leading to the uniform dispersion of the neurons on the surface.

With the height of the HafSOx unable to collect a sufficient protein to attract the neurons, a more direct approach was desirable. SU-8 is a common resist used to create channels dozens of microns deep, far thicker than needed, but once it is diluted down could make structures a single micron high, perfect for interacting with neurons.[10,11] To get the resolution and flexibility required, e-beam lithography was determined to be the ideal solution as opposed to traditional photolithography. By diluting down the SU-8 and optimizing the spin rates, 1 μm thick films with very little edge effects were created using electron beam lithography. Optimizing the patterning conditions was done through a succession of dose tests where lines of differing thickness were exposed to observe the thickness and edge roughness. Arrays of these lines were patterned at varying doses and developed to find the ideal amount of energy to use as seen in Figure 5. Top down views give great approximation but to see how much of the film has reacted under the beam, cross-sections were taken of each line. Surprisingly, the sensitivity of SU-8 was low enough that it required three orders of magnitude less energy to pattern than many other common polymer resists such as PMMA, requiring much less time to fabricate.

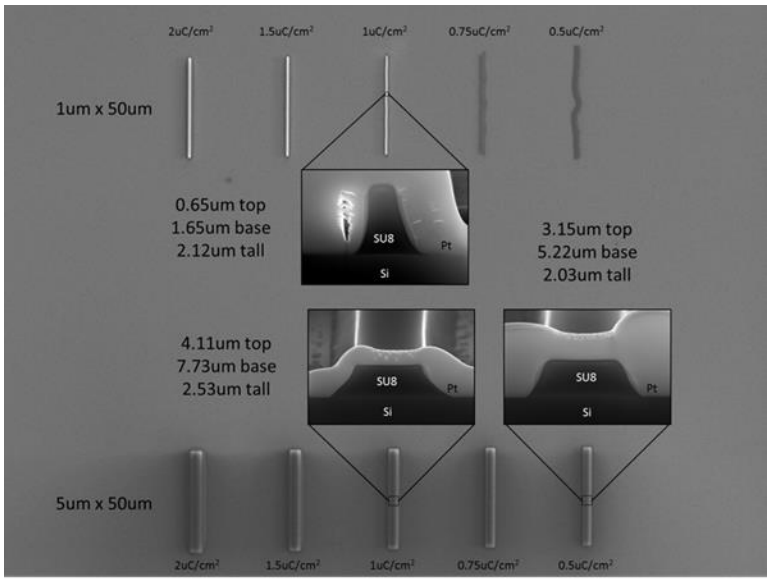

Figure 5: Dose array with cross sections to determine the limits of the resists.

The optimal dose changes depending on the size of the patterned feature. To accommodate the smallest widths that would be used in the pattern, 1μC/cm^2 was used. Initial exposures were done on the H-bar fractal as, due to its compact nature, it would represent some of the more challenging patterns that have to avoid over exposure. Cross sections were taken to confirm the structure was complete with very little over exposure that could have washed out smaller features, seen in Figure 6. The low exposure dose required for SU-8 allowed for the fractals to be twenty five times larger than previous HafSOx H-bars.

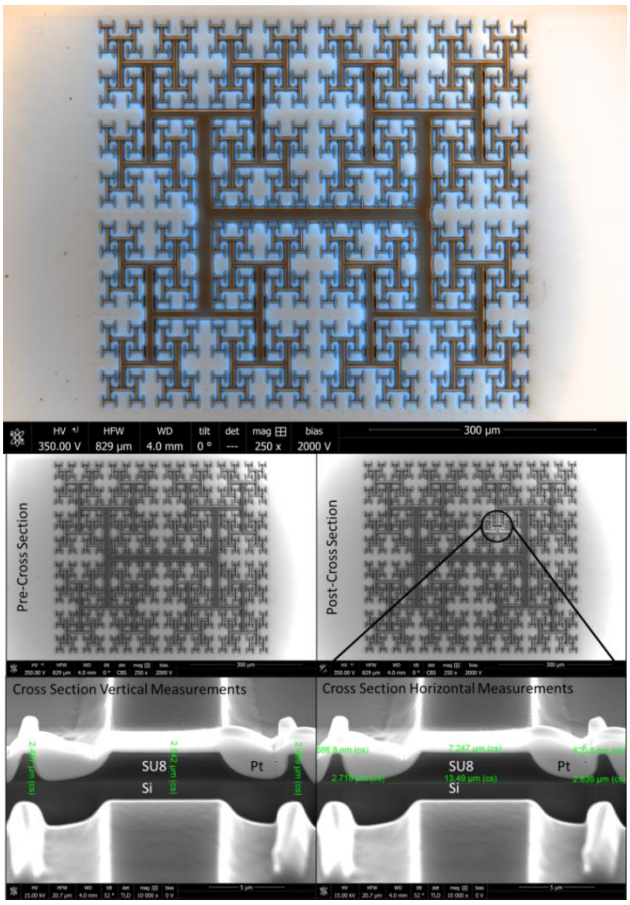

Figure 6: H-bar fractal with cross section.

Following the HafSOx samples, an array composed of SU-8 was created using sixteen 500 µm patterns containing four copies of an H-bar fractal and three controls. The new samples used only the H-bar but changed the packing within the fractal. Fractal packing is defined by the fractal dimension, D, as seen in Formula 1. The fractal dimension is determined by the scaling factor, ε, and the number of new iterations, N. The scaling factor is the relative size difference between fractal orders, meaning if the first H is twice the size of the second H, ε is two. The number of new iterations is how many new H's surround the first H, meaning if there are four new H's, N is four.

Three different sets of samples were created using SU-8 that was comprised of different D parameters for the H-bar fractal, 1.5, 1.7, and 2.0, allowing the effects of the scaling of the fractal on neural adhesion to be assessed, seen in Figure 7. With all three samples being almost identical, not only will the hypothesis of fractals aiding the binding of neurons to the surface be tested, but the effect of the packing of the fractals on neuron binding will be established as well.

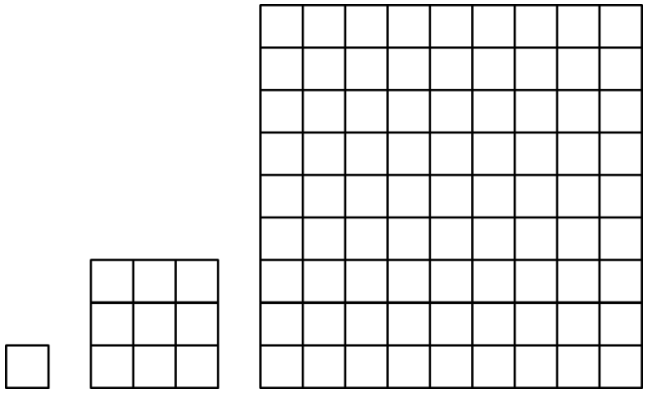

$$D = -\frac{Log\ N}{Log\ \varepsilon}$$

Figure 7: The fractal dimension (D) depends on the scaling factor (ε) and the number of iterations (N).

Three controls are needed to indicate what interactions dominate the neuron binding. The first is most basic, the footprint. A patterned square the same size as the footprint of the H-bar fractals, "same footprint square," will give a baseline for how much the neurons are affected by the simple presence of SU-8 over a set area. To assess the effect of the physical amount of SU-8 on neuron binding, a square with the same amount

of patterned SU-8, “same mass square,” is used. The last control is for the smallest H used in the fractals repeated in a grid, which will test the neurons’ affinity for small binding hand-holds. Sixteen samples were successfully created, six with a D of 1.5, six with a D of 1.7, and four with a D of 2.0 (Figure 8). All were sent to collaborators at Lund University to have neurons cultured on the samples and binding measured.

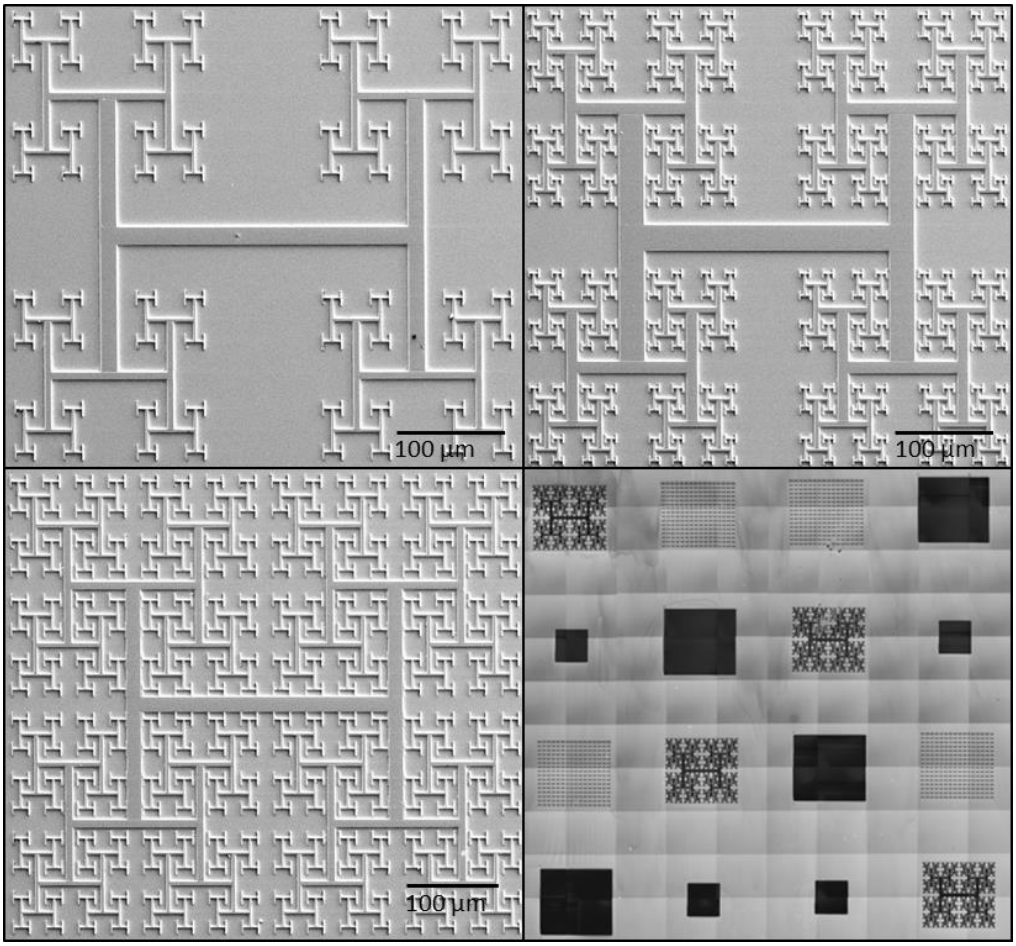

Figure 8: H-bar fractal with a D value of 1.5 (top left), 1.7 (top right), 2.0 (bottom left), and a complete array.

The samples were packed in gel bottomed jewel cases, Figure 9, to protect them in the shipping over to Lund, Sweden for the biological studies. It was also noted that the fractals have become so big that they can be seen with the naked eye, making processing and neuron growth more accurate with less sample destruction. It was important to

continue producing samples before the cells were cultured because the lead time is approximately one month and having another iteration to test immediately was critical. This led to guessing what would be needed in the subsequent iterations.

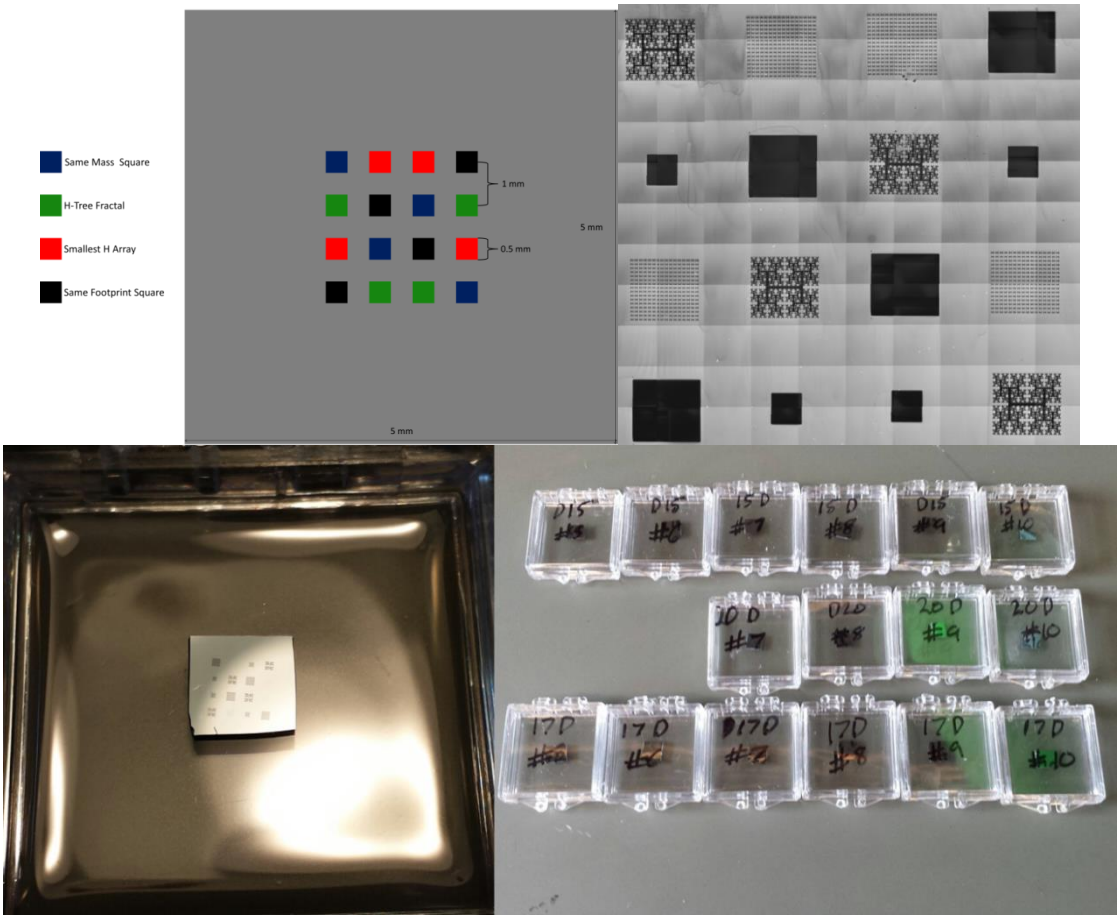

Figure 9: The first set of SU-8 samples sent to Lund. Their layout (top left), composite SEM image of a D 2.0 sample (top right), macroscopic image of patterns (bottom left), and complete array of samples sent (bottom right).

The third iteration of samples was done to combine the fractals with a D perimeter of 1.5 and 2.0 giving the largest range. To do this, the "same mass square" control was removed and the extra fractal was put into its place, Figure 10. Having both D dimensions on the same sample will allow a direct comparison between how the neurons react to the same fractal that has a different packing. Since neurons have different fractal

dimensions themselves, this could show how packing densities affect neuron binding. These samples have yet to be tested.

The fourth iteration of samples was done to test both the largest and smallest fractal “H” within the fractals to compare the interaction of the neurons with the largest and smallest features on the fractal. This is to compare the tiny hand-holds created by the smallest features versus the large, sweeping walls created by the main feature in the fractal. These samples have yet to be tested. The fifth and final iteration of samples was a carbon copy of the third iteration but without the final anneal. These samples were created to better compare to literature precedence on SU-8 interactions with neurons, mainly to show that annealing the samples and removing reactive components with the material is beneficial for neuron growth. These samples have yet to be tested.

To test the SU-8 fractal patterns, four samples from the first batch were submerged in a culture with neurons to promote growth, all from the samples with fractals that had a D of 1.5. The results showed the best performance was from the sample that was not only covered with 20 nm of hafnium oxide but was heated to 150 ℃ for three days as well. In all other samples, the small square control performed the worst even when the area was normalized between all the samples. As for the rest of the patterns, there doesn’t seem to be any clear trend.

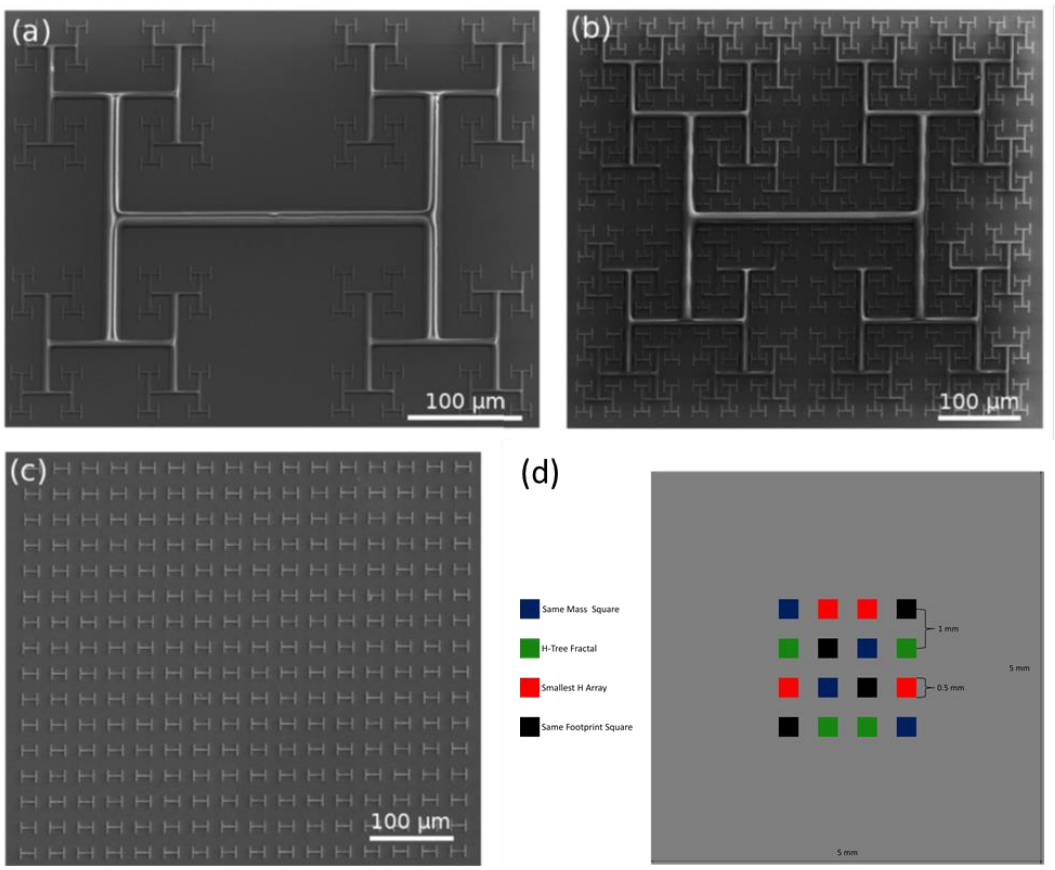

Figure 10: The third iteration of samples showing the D 1.5 fractal (top left), D 2.0 fractal (top right), small "H" array (bottom left), and chip layout (bottom right).

To determine the surface texture neurons prefer, the cells were stained and counted. This allows the direct comparison between any surface texture on the sample and the bare background. Three stains were used, DAPI, β-tubulin III, and GFP, as seen in Figure 11. DAPI targets the nuclei of the neurons, staining them blue, and allows for accurate counting of the density of the cells. β-tubulin stains the entire neuron red revealing the fine structure of the neuron growth and giving insight into the path the growth takes, Figure 12. GFP is a green dye that lights up glial cells, which act as physical and nutritional support for the neurons, possibly showing where nutrition is collecting within the surface texture.

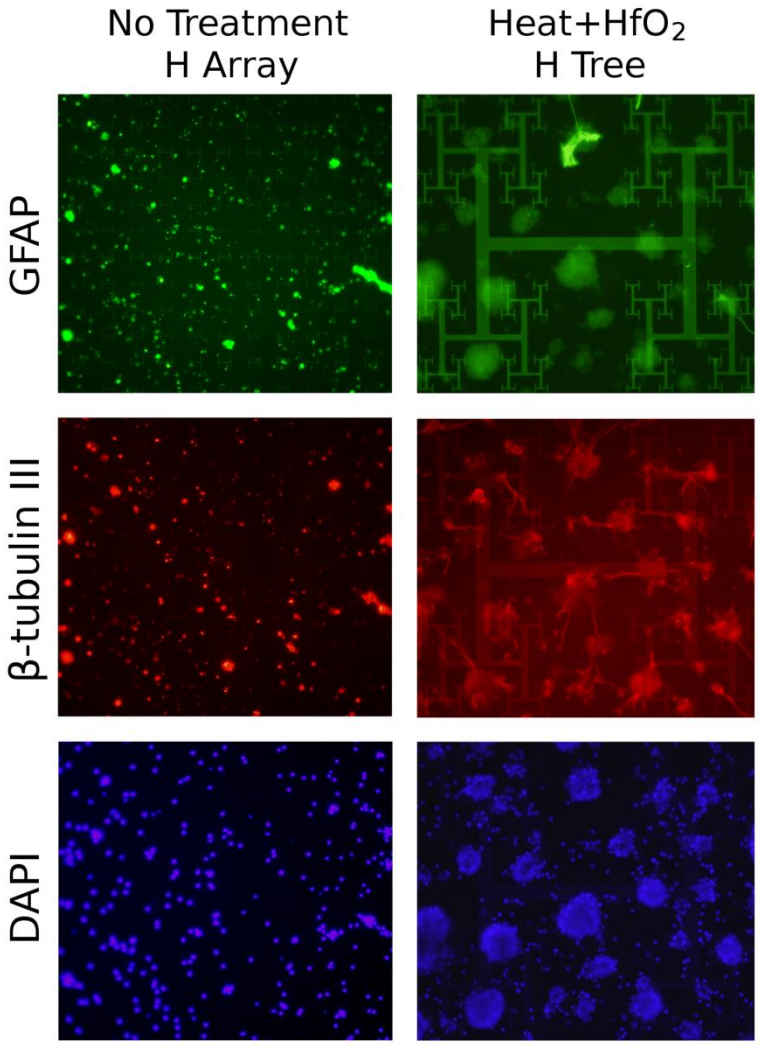

Figure 11: The three dyes used to stain the cells in the neuron studies.

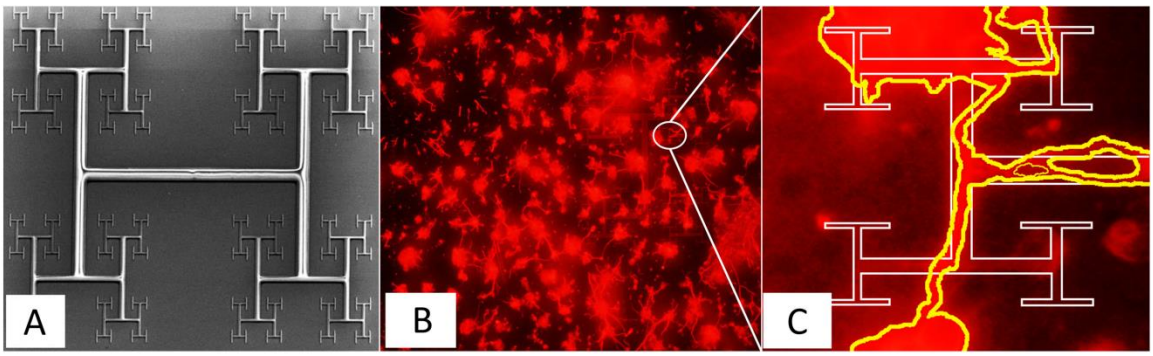

Figure 12: SEM image of an H-bar fractal, fluorescent image of H-bar fractal with stained neurons, the overlay of the H-bar fractal in a blow up of the fluorescent image.

The first set of SU-8 samples analyzed, Figure 13, show a side by side comparison between the bare SU-8 and the three post processing conditions used to reduce the toxicity of the resist. It can be seen that both the bare SU-8 and the SU-8 coated with 20 nm of hafnium oxide had comparable adhesion rates with the fractals performing the best. The sample that was baked at 150 °C for three days had the worst binding, and surprisingly the control of bare silica had the best binding. Finally, the sample with both the hard bake of 150 °C for three days and 20 nm of HfO_2 had the highest binding, but unlike the first two samples the large square had the best binding.

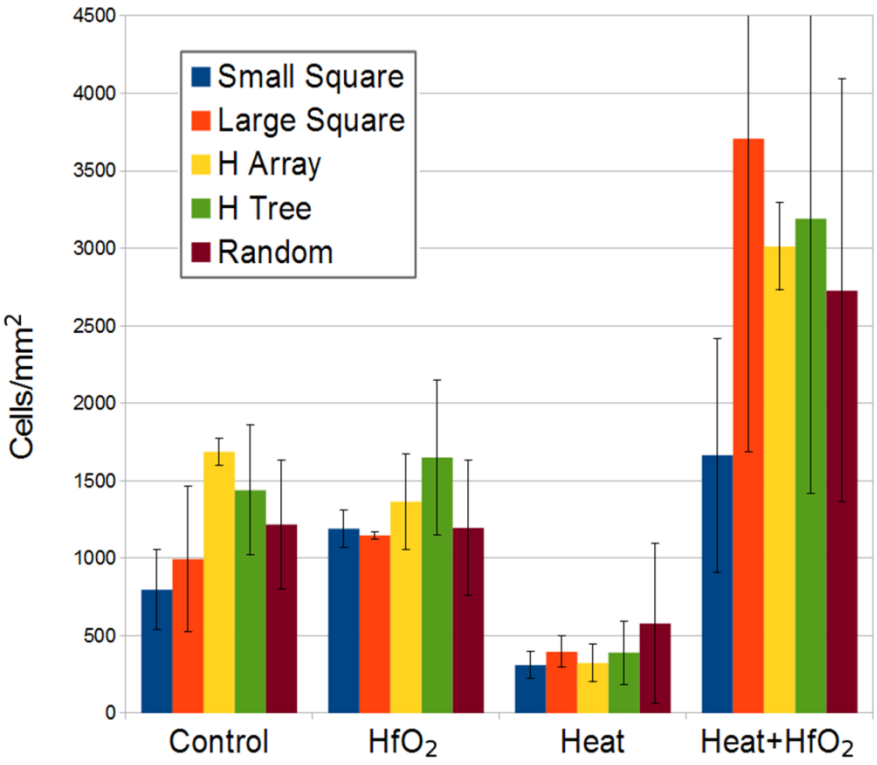

Figure 13: First round results from the neuron binding.

4.4. Conclusion

The images of the neurons show there is growth on some of the fractals following the physical structure. This indicates that there is a preference to the fractal texture on the surface. Without further studies, there is not much that can be conclusively determined since the error in the measurements is so large. What can be said is that in the control, the H Array has better binding than all three controls, which is promising to continue pursuing more trials.

This work has had promising results but lacks enough data to make any concrete assertions. The sample with both controls had the most neuron binding out of any sample suggesting the hafnium oxide coating and baking were beneficial. It is interesting that the

annealed sample had the least binding due to the fact that when coupled with the oxide it performed the best.

4.5. Moving Forward

The next step in testing neuron growth on fractal surfaces is to use a titanium nitride substrate that has the fractal texturing etched into it. Titanium nitride has been well studied in biological applications and it has been demonstrated to work well in medical applications within the eye.[7] To achieve a titanium nitride veneer, a 3" target will be loaded into the RF sputter system along with a silicon wafer with thermal oxide grown on top. 2 μm of material will be deposited to give enough material to etch and leave features detectable by neurons. HafSOx will be spun onto the veneered wafer as previously mentioned. If wetting is a problem, a thin layer of aluminum will be deposited via thermal evaporation. Etching will be done using a dry plasma etch and will need to be optimized.

A second method for achieving better interactions between the surface texture and neurons is to use functionalized SU-8 that is decorated with a biocompatible surface[12]. This will allow the use of previously developed SU-8 samples to be coated with a neuron friendly protein only on the fractals and controls. This decoration is not only already developed but has been shown to have favorable interactions with neurons and will greatly aid in attracting neurons and encouraging binding.

CHAPTER V

NON-LITHOGRAPHIC NANOWIRES AND NANOSTRUCTURE MORPHOLOGY THROUGH ANION INTERACTIONS

Work in Chapter V has not been published but led to a publication in *Organic and Biomolecular Chemistry*: Watt, M.M.; Engle, Jeffrey M.; Fairley, K.C.; Robitshek, T.E.; Haley, M.M.; Johnson, D.W., "Off-on" aggregation-based fluorescent sensor for the detection of chloride in water, *Organic & Biomolecular Chemistry*, **2015**, 13, 4266-4270

5.1. Chapter Introduction

Throughout this thesis it has been shown that lithography enables for the patterning of incredibly small and precise features that has propelled great advances in many fields. This typically relies on the use of focused energy in the form of electrons, photons, or ions that begin to do chemistry. In this chapter, a method to create specific geometries without the use of these external patterning forces is discussed.

5.2. Introduction

Organic nanofibers are interesting materials due to their tunability, flexibility, and potential use as electronic components. However, limitations remain to preparing these materials through scalable and selective processes. Typical nanofibers are fabricated using a porous mold or assembled using weak π-π and C–H-π supramolecular

interactions. This requires either preparation of a porous mold, or reliance on relatively weak supramolecular interactions that are highly solvent dependent. In order to report the characterization of fully organic nanofibers that overcome these obstacles, anions are used as an internal rather than external template for nanofiber growth, thereby taking advantage of the positive features of both existing design strategies. This new method provides a facile route to a variety of nanoscale structures by changing the anion template.

The development of organic 1-D nanofibers has received considerable attention over recent years due to potential uses in nanoscale electronics and biomaterials.[1–7] Organic nanofibers unlike inorganic nanofibers are more synthetically flexible and can be tuned to a greater degree with respect to their electronic properties and morphologies.

One area that has been lacking is the methodologies available for nanowire assembly. Current methods typically consist of using a porous solid-support casting system, or taking advantage of supramolecular stacking, consisting of primarily π-π or hydrogen bonding interactions.[8–12] While both of these methods allow access to organic nanofibers, both have fundamental shortcomings. First, casting techniques are inherently more burdensome since a porous mold must be made and subsequently removed.[2,12] Second, supramolecular techniques currently only take advantage of relatively weak non-covalent interactions, π-π and C–H-π.[11]

Herein, a system is proposed that takes advantage of supramolecular stacking while utilizing anions as an internal template for nanofiber fabrication. Furthermore, variation of the anionic guest allows for an array of morphologies to be formed from one parent molecular system. This could allow for rapid investigation of a variety of organic

supramolecular nanofibers, and speed up development in this burgeoning field of materials chemistry.

5.3. Materials and Methods

General Methods: Compounds **1-2** were prepared according to the previously published literature reports.[13–15] Acetonitrile used was High Purity HPLC grade solvent purchased from Burdick and Jackson. Tetrabutylammonium salts were purchased from Sigma Aldrich (98% purity and higher) and used after being desiccated via high vacuum overnight.

*Nanofiber Fabrication Scheme***:** A 2 mM stock solution of **2·HBF$_4$** in acetonitrile was prepared and filtered using a 0.45 µm acrodisk syringe filter. In addition 2 mM stock solutions of TBACl, TBABr, TBAI, TBAClO$_4$, TBAH$_2$PO$_4$, and TBANO$_3$ were prepared in acetonitrile and filtered using a 0.45 µm acrodisk syringe filter. Silicon wafers approximately 1.5 cm by 1.5 cm were cut and 5 µL of the **2·HBF$_4$** stock solution was added to the top of the wafer followed immediately by 5 µL of a corresponding tetrabutylammonium salt stock solution. The substrate used was a doped silicon wafer. No surface treatment was used to alter the ~2 nm native oxide. SEM images were taken using a Zeiss Ultra-55 SEM operating at 5Kv with a 20um aperture and an in-lens detector.

5.4. Results and Discussion

The Darren Johnson group has previously reported the synthesis and characterization of a series of supramolecular anion sensors based on a 2,6-bis(2-anilinoethynyl)pyridine scaffold.[13–18] These easily tunable sensors bind anions through electrostatic interactions and hydrogen bonding. The group has shown some of these

sensors to be highly specific to certain anions across an array of solvent conditions.[13–15]

Compound **1·HCl** (Fig. 1) was one of the first Darren Johnson anion sensors that showed a remarkable degree of selectivity for chloride when protonated. Examination of the crystal packing in the X-ray structure revealed that the host molecule stacked on itself through an inversion center between each molecule with Cl^- bound inside. Each Cl^- anion was bound to the parent host molecule through five hydrogen bonds along with an electrostatic pyridinium interaction.[14]

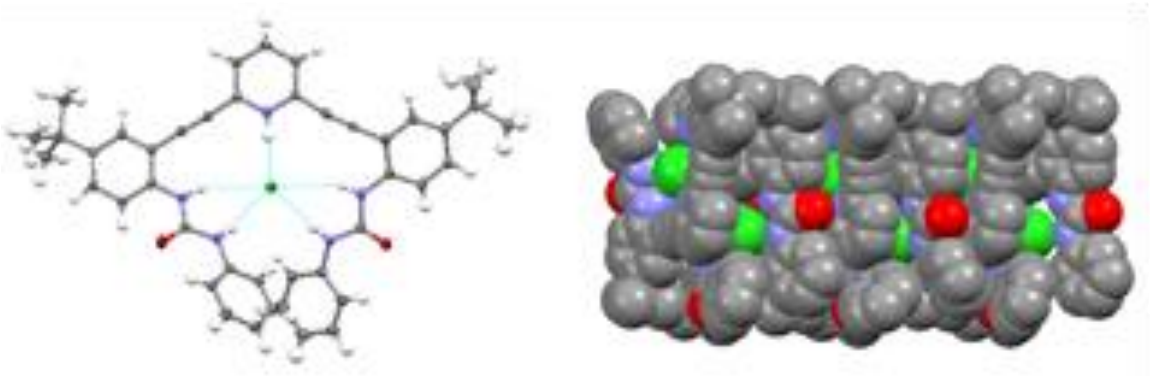

*Figure 1: (Left) Single crystal X-ray structure of **1·HCl** with ellipsoids drawn at the 50% probability level. (Right) Space filling model of **1·HCl** from the top-down view showing alternating up/down host molecules with Cl^- in their respective cavities (hydrogens removed for clarity).*

Additional evidence of this stacking behaviour was observed during the investigation of this class of compounds. For example, compound **2·HBF$_4$** (Fig. 2) is entirely transparent when dissolved in acetonitrile, but upon addition of tetrabutylammonium salts the solution becomes opaque.

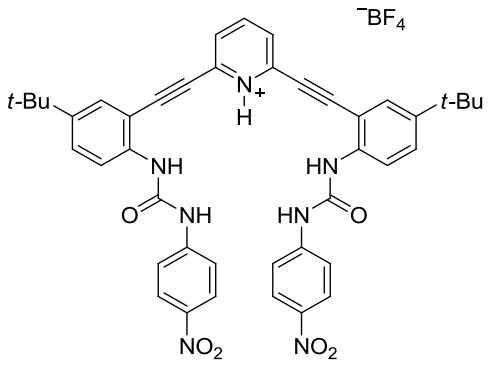

*Figure 2: Compound **2·HBF$_4$***

While the aggregation proved problematic for determining binding constants due to the complex equilibrium occurring in solution,[13] it proved to be very intriguing when examined by

scanning electron microscopy (SEM). SEM samples were prepared by sonicating 16.7mg of **2·HBF$_4$** in 10mL acetonitrile, creating a saturated solution. 1mL was immediately mixed with an equal volume of 2mM tetrabutylammonium salt solution. The one to one mixture of **2·HBF$_4$** to salt was then drop cast as quickly as possible onto an arsenic doped silicon wafer with a native oxide coating. The wafer had been previously treated with a 30% oxygen plasma at 150W for 30 seconds just before the solutions were prepared. The plasma treatment was done to clean the surface and increase wetting. SEM images were taken using a Zeiss Ultra-55 SEM operating at 5 kV with a 20 µm aperture and an in-lens detector.

Figure 3 shows a variety of observed nano-structures grown in the presence of differing tetrabutylammonium salts. The most noticeable features in these images are the long 1-D rods that result from the addition of tetrabutylammonium halides. Remarkably, there are very distinct differences between each of the halide samples. Samples prepared

with tetrabutylammonium chloride form long cylindrical rods that are approximately 200 nm wide and many microns long. On the other hand samples prepared with tetrabutylammonium bromide form cubic rods of varying sizes containing distinct branching points in the center of each cluster. Interestingly, when the even larger tetrabutylammonium iodide is used, long, barbed nanofibers are observed. The structural diversity indicates that even the subtle change of halide size has a very significant impact on the overall morphology of the nanofibers that form.

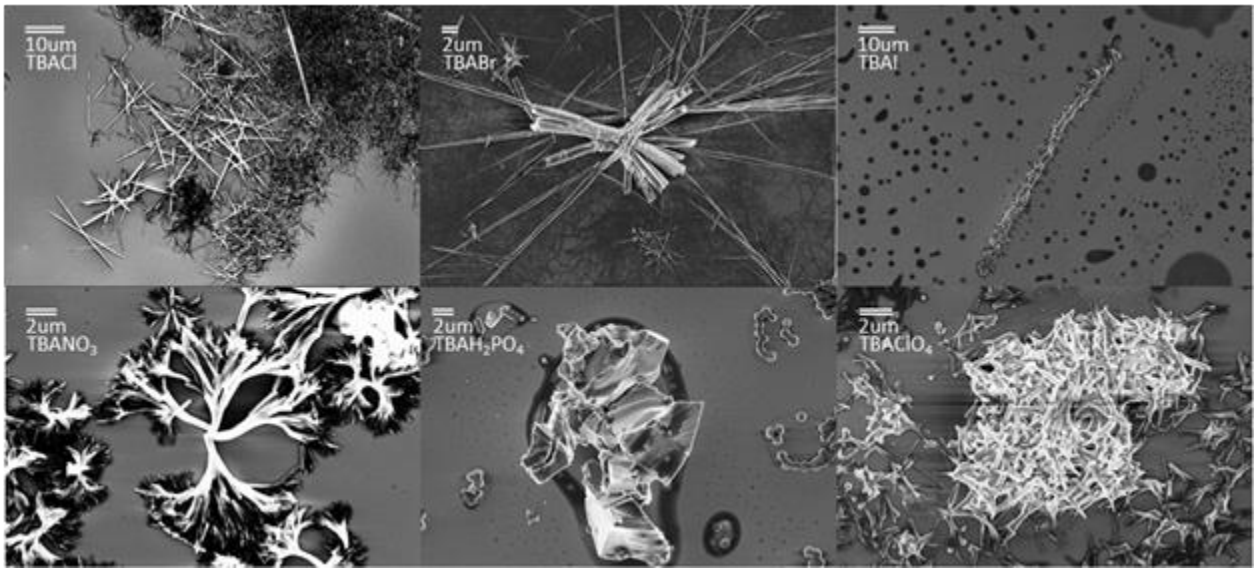

*Figure 3: SEM images of compound **2·HBF$_4$** in the presence of different salts*

The oxoanions result in an even greater diversity of microstructures. For example, when tetrabutylammonium nitrate is used, considerable branching is observed and aggregates form broccoli like structures. Tetrabutylammonium perchlorate forms ill-defined mats of short needles.

It is hypothesized that large anions either bind in a different conformation or they are so large that the backbone is twisted significantly out of planarity. Either of these situations could disrupt or distort molecular stacking resulting in the wide array of nanofibers observed by SEM.

Of particular interest were the fibers that formed upon addition of tetrabutylammonium chloride. These structures appeared to have uniform morphologies and often grew several microns long. An analysis of the elemental composition of the nanofibers and the surrounding organic film was performed using energy-dispersive X-ray spectroscopy (EDS). The background film showed no indication of chloride, while chloride was observed in all of the nanofibers tested. This indicates that inclusion of chloride is essential for fiber formation, and without chloride the host compound simply forms films with varying amounts of pinhole defects.

Solution studies of **2·HBF$_4$** have previously shown the anility of this compound to act as a turn-on fluorescent probe for various anions. An interesting feature of these systems is that films of **2·HBF$_4$** are almost completely non-fluorescent. However, when tetrabutylammonium chloride is added to the solutions before drop casting, the resulting fibers are very fluorescent (Figure 4). It is believed that this fluorescence is due to aggregation induced emission, where the molecular host-gust complex itself is not fluorescent, but the fluorescence is produced when it stacks and forms fibers. This fluorescence is believed to take place via aggregation induced emission. This is the opposite response seen in most fluorophores where stacking tends to lead to a quenching of fluorescence.[19]

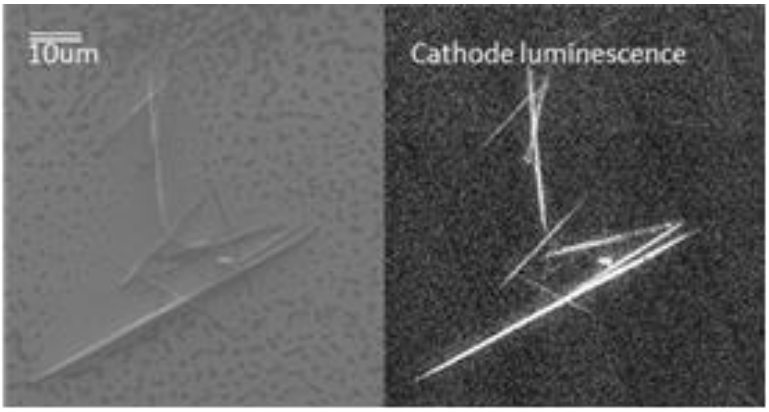

Figure 4: SEM image of Compound 2·Cl (left) and the same sample under Cathodo-Luminescence (right). The fluorescent image shows only the crystals of stacked Compound 2·Cl are visible and not the film of Compound 2·Cl that surrounds them.

5.5. Conclusion

Typically Nanofibers made through supramolecular assemblies rely on π-π, C–H-π, or hydrophobic-hydrophilic supramolecular interactions. These observations indicate that supramolecular nanofiber assemblies can be dramatically altered by the addition of anions. While this is not surprising when compared to other supramolecular structures, such as proteins and supramolecular gels, it is surprising that such a diverse assortment of morphologies of nanofibers can be obtained by simply changing an anionic guest.

This approach allows for fine tuning of nanostructure morphologies in a terminal step. While a bottom-up design approach is appealing from a theoretical point of view, in practice it can be difficult to predict how supramolecular complexes will arrange on a macroscopic scale. Having a simple tool available to fine tune higher order morphologies in a terminal step could not only make accessing a desired structure more facile, but it could also allow access to an array of potentially useful structures from one parent molecule. To the best of our knowledge this is the first such system that takes advantage

of anions as internal templates for nanofiber fabrication.

REFERENCES CITED

Chapter I

(1) Feynman, R. P. There's Plenty of Room at the Bottom. *Eng. Sci.* **1960**, *23*, 269.

(2) Madou, M. Fundamentals of Microfabrication. (2002), CRC Press: Boca Raton, Florida.

(3) Colson, P.; Henrist, C.; Cloots, R. Nanosphere Lithography: A Powerful Method for the Controlled Manufacturing of Nanomaterials. *J. Nanomater.* **2013**, *2013*, 1.

(4) Okazaki, S. High resolution optical lithography or high throughput electron beam lithography: The technical struggle from the micro to the nano-fabrication evolution. *Microelectron. Eng.* **2015**, *133*, 23.

(5) Bonam, R.; Verhagen, P.; Munder, a.; Hartley, J. Performance characterization of negative resists for sub-10-nm electron beam lithography. *J. Vac. Sci. Technol. B Microelectron. Nanom. Struct.* **2010**, *28*, C6C34.

(6) Mojarad, N.; Gobrecht, J.; Ekinci, Y. Interference lithography at EUV and soft X-ray wavelengths: Principles, methods, and applications. *Microelectron. Eng.* **2015**, *143*, 55.

(7) Joshi-imre, A.; Bauerdick, S. Direct-Write Ion Beam Lithography. *J. Nanotechnol.* **2014**, *2014*.

(8) Telecky, A.; Xie, P.; Stowers, J.; Grenville, A.; Smith, B.; Keszler, D. A. Photopatternable inorganic hardmask. *J. Vac. Sci. Technol. B Microelectron. Nanom. Struct.* **2010**, *28*, C6S19.

(9) Oleksak, R. P.; Ruther, R. E.; Luo, F.; Fairley, K. C.; Decker, S. R.; Stickle, W. F.; Johnson, D. W.; Garfunkel, E. L.; Herman, G. S.; Keszler, D. A. Chemical and Structural Investigation of High-Resolution Patterning with HafSOx. *ACS Appl. Mater. Interfaces* **2014**, *6*, 2917.

(10) Grigorescu, A. E.; van der Krogt, M. C.; Hagen, C. W.; Kruit, P. 10nm lines and spaces written in HSQ, using electron beam lithography. *Microelectron. Eng.* **2007**, *84*, 822.

(11) Vigneswaran, N.; Samsuri, F.; Ranganathan, B.; Padmapriya. Recent Advances in Nano Patterning and Nano Imprint Lithography for Biological Applications. *Procedia Eng.* **2014**, *97*, 1387.

Chapter II

(1) Vieu, C.; Carcenac, F.; Pepin, A.; Chen, Y.; Mejias, M.; Lebib, A.; Couraud, L.; Launois, H. Electron beam lithography: resolution limits and applications. *Appl. Surf. Sci.* **2000**, *164*, 111.

(2) Huang, J.; Fan, D.; Ekinci, Y.; Padeste, C. Fabrication of ultrahigh resolution metal nanowires and nanodots through EUV interference lithography. *Microelectron. Eng.* **2015**, *141*, 32.

(3) Brinker, C. J.; Scherer, G. W. Sol-Gel Science: The Physics and Chemistry of Sol-Gel Processing. (1990), Academic Press: San Diego, CA, USA.

(4) Scherer, G. W. Recent progress in drying of gels. *J. Non. Cryst. Solids* **1992**, *147-148*, 363.

(5) Meyers, S. T.; Anderson, J. T.; Hong, D.; Hung, C. M.; Wager, J. F.; Keszler, D. A. Solution-processed aluminum oxide phosphate thin-film dielectrics. *Chem. Mater.* **2007**, *19*, 4023.

(6) Anderson, J. T.; Munsee, C. L.; Hung, C. M.; Phung, T. M.; Herman, G. S.; Johnson, D. C.; Wager, J. F.; Keszler, D. A. Solution-processed HafSOx and ZircSOx inorganic thin-film dielectrics and nanolaminates. *Adv. Funct. Mater.* **2007**, *17*, 2117.

(7) Meyers, S. T.; Anderson, J. T.; Hung, C. M.; Thompson, J.; Wager, J. F.; Keszler, D. A. Aqueous inorganic inks for low-temperature fabrication of ZnO TFTs. *J. Am. Chem. Soc.* **2008**, *130*, 17603.

(8) Jiang, K.; Zakutayev, A.; Stowers, J.; Anderson, M. D.; Tate, J.; McIntyre, D. H.; Johnson, D. C.; Keszler, D. A. Low-temperature, solution processing of TiO2 thin films and fabrication of multilayer dielectric optical elements. *Solid State Sci.* **2009**, *11*, 1692.

(9) Cowell, E. W.; Knutson, C. C.; Wager, J. F.; Keszler, D. A. Amorphous metal/oxide nanolaminate. *ACS Appl. Mater. Interfaces* **2010**, *2*, 1811.

(10) Alemayehu, M.; Davis, J. E.; Jackson, M.; Lessig, B.; Smith, L.; Sumega, J. D.; Knutson, C.; Beekman, M.; Johnson, D. C.; Keszler, D. A. Tunable dielectric thin films by aqueous, inorganic solution-based processing. *Solid State Sci.* **2011**, *13*, 2037.

(11) Jiang, K.; Anderson, J. T.; Hoshino, K.; Li, D.; Wager, J. F.; Keszler, D. A. Low-energy path to dense HfO2 thin films with aqueous precursor. *Chem. Mater.* **2011**, *23*, 945.

(12) Jiang, K.; Meyers, S. T.; Anderson, M. D.; Johnson, D. C.; Keszler, D. A. Functional ultrathin films and nanolaminates from aqueous solutions. *Chem. Mater.* **2013**, *25*, 210.

(13) Kim, K. M.; Kim, C. W.; Heo, J. S.; Na, H.; Lee, J. E.; Park, C. B.; Bae, J. U.; Kim, C. D.; Jun, M.; Hwang, Y. K.; Meyers, S. T.; Grenville, A.; Keszler, D. A. Competitive device performance of low-temperature and all-solution- processed metal-oxide thin-film transistors. *Appl. Phys. Lett.* **2011**, *99*, 2013.

(14) Smith, S. W.; Wang, W.; Keszler, D. A.; Conley, J. F. Solution based prompt inorganic condensation and atomic layer deposition of Al2O3 films: A side-by-side comparison. *J. Vac. Sci. Technol. A Vacuum, Surfaces, Film.* **2014**, *32*, 041501.

(15) Plassmeyer, P. N.; Archila, K.; Wager, J. F.; Page, C. J. Lanthanum Aluminum Oxide Thin-Film Dielectrics from Aqueous Solution. *ACS Appl. Mater. Interfaces* **2015**, *7*, 1678.

(16) Keszler, D. A.; Anderson, J. T.; Meyers, S. T. Oxide Dielectric Films for Active Electronics, In Solution Processing of Inorganic Materials. Mitzi, D. B., Ed.; (2008), John Wiley & Sons, Inc.: Hoboken, NJ, USA.

(17) Nadarajah, A.; Wu, M. Z. B.; Archila, K.; Kast, M. G.; Smith, A. M.; Chiang, T. H.; Keszler, D. A.; Wager, J. F.; Boettcher, S. W. Amorphous In–Ga–Zn Oxide Semiconducting Thin Films with High Mobility from Electrochemically Generated Aqueous Nanocluster Inks. *Chem. Mater.* **2015**, *27*, 5587.

(18) Telecky, A.; Xie, P.; Stowers, J.; Grenville, A.; Smith, B.; Keszler, D. A. Photopatternable inorganic hardmask. *J. Vac. Sci. Technol. B Microelectron. Nanom. Struct.* **2010**, *28*, C6S19.

(19) Oleksak, R. P.; Ruther, R. E.; Luo, F.; Fairley, K. C.; Decker, S. R.; Stickle, W. F.; Johnson, D. W.; Garfunkel, E. L.; Herman, G. S.; Keszler, D. A. Chemical and Structural Investigation of High-Resolution Patterning with HafSOx. *ACS Appl. Mater. Interfaces* **2014**, *6*, 2917.

(20) Ashby, P. D.; Olynick, D. L.; Ogletree, D. F.; Naulleau, P. P. Resist Materials for Extreme Ultraviolet Lithography: Toward Low-Cost Single-Digit-Nanometer Patterning. *Adv. Mater.* **2015**, 1.

(21) Dobisz, E.; Brandow, S.; Bass, R.; Mitterender, J. Effects of molecular properties on nanolithography in polymethyl methacrylate. *J. Vac. Sci Technol. B* **2000**, *18*, 107.

(22) Hasko, D.; Yasin, S.; Mumtaz, A. Influence of developer and development conditions on the behavior of high molecular weight electron beam resists. *J. Vac. Sci Technol. B* **2000**, *18*, 3441.

(23) Sidorkin, V.; Grigorescu, A.; Salemink, H.; Drift, E. Van Der. Resist thickness effects on ultra thin HSQ patterning capabilities. *Microelectron. Eng.* **2009**, *86*, 749.

(24) Grigorescu, A. E.; Hagen, C. W. Resists for sub-20-nm electron beam lithography with a focus on HSQ: state of the art. *Nanotechnology* **2009**, *20*, 292001.

(25) Cairncross, R. A.; Schunk, P.; Chen, K. S.; Prakash, S. S.; Samuel, J.; Hurd, A.; Brinker, C. J. Pore Evolution and Solvent Transport During Drying of Gelled Sol-Gel Coatings: Predicting "Springback." *Dry. Technol.* **1997**, *15*, 1815.

(26) Teodorescu, V. S.; Blanchin, M. G. TEM study of the sol-gel oxide thin films, In Microscopy: Advances in Scientific Research and Education. (2014), FORMATEX: Madrid, Spain.

(27) Gutmann, E.; Meyer, D. C.; Levin, A. A.; Paufler, P. Density-modulated alumina-based nanometre films prepared by sol-gel technique. *Appl. Phys. A Mater. Sci. Process.* **2005**, *81*, 249.

(28) Brito, G. E. S.; Morelha, S. L.; Abramof, E. Nanostructure of sol–gel films by x-ray specular reflectivity. *Appl. Phys. Lett.* **2002**, *80*, 407.

(29) Loke, V. L. Y.; Riefler, N.; Mehner, A.; Prenzel, T.; Hoja, T.; Wriedt, T.; Mädler, L. Multilayer model for determining the thickness and refractive index of sol-gel coatings via laser ellipsometry. *Thin Solid Films* **2013**, *531*, 93.

(30) Anderson, J. T.; Wang, W.; Jiang, K.; Gustafsson, T.; Xu, C.; Gafunkel, E. L.; Keszler, D. A. Chemically Amplified Dehydration of Thin Oxide Films. *ACS Sustain. Chem. Eng.* **2015**, *3*, 1081.

(31) Carnes, M. E.; Knutson, C. C.; Nadarajah, A.; Jackson, M. N.; Oliveri, A. F.; Norelli, K. M.; Crockett, B. M.; Bauers, S. R.; Moreno-Luna, H. A.; Taber, B. N.; Pacheco, D. J.; Olson, J. Z.; Brevick, K. R.; Sheehan, C. E.; Johnson, D. W.; Boettcher, S. W. Electrochemical synthesis of flat-[Ga13−xInx(μ3-OH)6(μ-OH)18(H2O)24(NO3)15] clusters as aqueous precursors for solution-processed semicond. *J. Mater. Chem. C* **2014**, *2*, 8492.

(32) Wang, W.; Liu, W.; Chang, I.-Y.; Wills, L. A.; Zakharov, L. N.; Boettcher, S. W.; Cheong, P. H.-Y.; Fang, C.; Keszler, D. A. Electrolytic synthesis of aqueous aluminum nanoclusters and in situ characterization by femtosecond Raman spectroscopy and computations. *Proc. Natl. Acad. Sci. U. S. A.* **2013**, *110*, 18397.

(33) Phung, T. M.; Johnson, D. C.; Antonelli, G. A. A detailed experimental and analytical study of the thermal expansion of dielectric thin films on Si by x-ray reflectivity. *J. Appl. Phys.* **2006**, *100*, 1.

(34) Wormington, M.; Panaccione, C.; Matney, K. M.; Bowen, K. Characterization of structures from X-ray scatterning data using genetic algorithms. *Phil. Trans. R. Soc. Lond. A* **1999**, *357*, 2827.

(35) Giannuzzi, L. A.; Stevie, F. A. Introduction to Focused Ion Beams: Instrumentation, Theory,Techniques, and Practice. (2005), Springer: New York, USA.

(36) Gustafsson, T.; Garfunkel, E.; Goncharova, L.; Starodub, D.; Barnes, R.; Dalponte, M.; Bersuker, G.; Foran, B.; Lysaght, P.; Schlom, D. G.; Vaithyanathan, V.; Hong, M.; Kwo, J. R. Structure, composition and order at interfaces of crystalline oxides and other high-k materials on silicon. *NATO Sci. Ser. II Math. Phys. Chem.* **2006**, *220*, 349.

(37) Stowers, J.; Keszler, D. a. High resolution, high sensitivity inorganic resists. *Microelectron. Eng.* **2009**, *86*, 730.

(38) Thrun, X.; Choi, K. H.; Freitag, M.; Grenville, A.; Gutsch, M.; Hohle, C.; Stowers, J. K.; Bartha, J. W. Evaluation of direct patternable inorganic spin-on hard mask materials using electron beam lithography. *Microelectron. Eng.* **2012**, *98*, 226.

(39) Ekinci, Y. Evaluation of EUV resist performance with interference lithography towards 11 nm half-pitch and beyond. *Proc. SPIE* **2013**, *8679*, 867910.

(40) Haller, I. High-resolution positive resists for electron-beam exposure. *IBM J. Res. Dev.* **1968**, *12*, 251.

(41) Chen, W.; Ahmed, H. Fabrication of 5-7 nm wide etched lines in silicon using 100 keV lithography and polymethylmethacrylate resist. **2001**, 1499.

(42) Nishida, T.; Notomi, M.; Iga, R.; Tamamura, T. Quantum wire fabrication by E-beam elithography using high-resolution and high-sensitivity E-beam resist ZEP-520. *Japanese J. Appl. Physics, Part 1 Regul. Pap. Short Notes Rev. Pap.* **1992**, *31*, 4508.

(43) Tanenbaum, D. M. High resolution electron beam lithography using ZEP-520 and KRS resists at low voltage. *J. Vac. Sci. Technol. B Microelectron. Nanom. Struct.* **1996**, *14*, 3829.

(44) Ito, H. Chemical amplification resists for microlithography, in Microlithography Molecular Inprinting. (2005).

(45) Namatsu, H. Three-dimensional siloxane resist for the formation of nanopatterns with minimum linewidth fluctuations. *J. Vac. Sci. Technol. B Microelectron. Nanom. Struct.* **1998**, *16*, 69.

(46) Trikeriotis, M. Development of an inorganic photoresist for DUV, EUV, and electron beam imaging. *Proce. SPICE* **2010**, *7639*, 76390E.

(47) Saifullah, M. S. M.; Khan, M. Z. R.; Hasko, D. G.; Leong, E. S. P.; Neo, X. L.; Goh, E. T. L.; Anderson, D.; Jones, G. a. C.; Welland, M. E. Spin-coatable HfO2 resist for optical and electron beam lithographies. *J. Vac. Sci. Technol. B Microelectron. Nanom. Struct.* **2010**, *28*, 90.

(48) Broers, A. N.; Hoole, A. C. F.; Ryan, J. M. Electron beam lithography—Resolution limits. *Microelectron. Eng.* **1996**, *32*, 131.

(49) Hino, M. The surface structure of sulfated zirconia: Studies of XPS and thermal analysis. *Thermochim. Acta* **2006**, *441*, 35.

(50) Breitkopf, C.; Papp, H.; Li, X.; Olindo, R.; Lercher, J. A.; Lloyd, R.; Wrabetz, S.; Jentoft, F. C.; Meinel, K.; F?rster, S.; Schindler, K.-M.; Neddermeyer, H.; Widdra, W.; Hofmann, A.; Sauer, J. Activation and isomerization of n-butane on sulfated zirconia model systems?an integrated study across the materials and pressure gaps. *Phys. Chem. Chem. Phys.* **2007**, *9*, 3600.

(51) Henderson, M. The interaction of water with solid surfaces: fundamental aspects revisited. *Surf. Sci. Rep.* **2002**, *46*, 1.

(52) Herman, G. S.; Kim, Y. J.; Chambers, S. A.; Peden, C. H. F. Interaction of D2O with CeO 2 (001) Investigated by Temperature-Programmed Desorption and X-ray Photoelectron Spectroscopy. *Langmuir* **1999**, *15*, 3993.

(53) Flynn, B.; Kim, D.; Clark, B. L.; Telecky, A.; Arnadottir, L.; Szanyi, J.; Keszler, D. A.; Herman, G. S. In-situ characterization of aqueous-based hafnium oxide hydroxide sulfate thin films. *Surf. interface Anal.* **2014**, *42*, 210.

(54) Okamoto, H.; Ishikawa, A.; Kudo, T. Photoresist Characteristics and Their Reaction Mechanism for Crystalline Peroxopolytungstic Acid. **1989**, *136*, 3.

Chapter III

(1) Michael, J. R. High resolution at low beam energy in the SEM: resolution measurement of a monochromated SEM. *Scanning* **2011**, *33*, 147.

(2) Phifer, D.; Tuma, L.; Vystavel, T.; Wandrol, P.; Young, R. J. Improving SEM Imaging Performance Using Beam Deceleration. *Mycroscopy Today* **2009**.

(3) Bell, D. C.; Erdman, N. Low Voltage Electron Microscopy: Principles and Applications. (2013).

(4) Suga, M.; Asahina, S.; Sakuda, Y.; Kazumori, H.; Nishiyama, H.; Nokuo, T.; Alfredsson, V.; Kjellman, T.; Stevens, S. M.; Cho, H. S.; Cho, M.; Han, L.; Che, S.; Anderson, M. W.; Schüth, F.; Deng, H.; Yaghi, O. M.; Liu, Z.; Jeong, H. Y.; Stein, A.; Sakamoto, K.; Ryoo, R.; Terasaki, O. Recent progress in scanning electron microscopy for the characterization of fine structural details of nano materials. *Prog. Solid State Chem.* **2014**, *42*, 1.

(5) Schatten, H.; Sibley, L. D.; Ris, H. Structural evidence for actin-like filaments in Toxoplasma gondii using high-resolution low-voltage field emission scanning electron microscopy. *Microsc. Microanal.* **2003**, *9*, 330.

(6) Chen, Y. Nanofabrication by electron beam lithography and its applications: A review. *Microelectron. Eng.* **2015**, *135*, 57.

(7) Delachat, F.; Constancias, C.; Reche, J.; Dal'Zotto, B.; Pain, L.; Le Drogoff, B.; Chaker, M.; Margot, J. Determination of spot size and acid diffusion length in positive chemically amplified resist for e-beam lithography at 100 and 5 kV. *J. Vac. Sci. Technol. B, Nanotechnol. Microelectron. Mater. Process. Meas. Phenom.* **2014**, *32*, 06FJ02.

(8) Manfrinato, V. R.; Cheong, L. L.; Duan, H.; Winston, D.; Smith, H. I.; Berggren, K. K. Sub-5 keV electron-beam lithography in hydrogen silsesquioxane resist. *Microelectron. Eng.* **2011**, *88*, 3070.

(9) Liu, C.-H.; Ng, P. C. W.; Shen, Y.-T.; Chien, S.-W.; Tsai, K.-Y. Impacts of point spread function accuracy on patterning prediction and proximity effect correction in low-voltage electron-beam–direct-write lithography. *J. Vac. Sci. Technol. B Microelectron. Nanom. Struct.* **2013**, *31*, 021605.

(10) Rio, D.; Constancias, C.; Saied, M.; Icard, B.; Pain, L. Study on line edge roughness for electron beam acceleration voltages from 50 to 5 kV. *J. Vac. Sci. Technol. B Microelectron. Nanom. Struct.* **2009**, *27*, 2512.

(11) Tilke, a.; Vogel, M.; Simmel, F.; Kriele, a.; Blick, R. H.; Lorenz, H.; Wharam, D. a.; Kotthaus, J. P. Low-energy electron-beam lithography using calixarene. *J. Vac. Sci. Technol. B Microelectron. Nanom. Struct.* **1999**, *17*, 1594.

(12) Oh, S. H.; Kim, J. G.; Kim, C. S.; Choi, D. S.; Chang, S.; Jeong, M. Y. The fabrication of 3-D nanostructures by a low- voltage EBL. *Appl. Surf. Sci.* **2011**, *257*, 3817.

(13) Oleksak, R. P.; Ruther, R. E.; Luo, F.; Fairley, K. C.; Decker, S. R.; Stickle, W. F.; Johnson, D. W.; Garfunkel, E. L.; Herman, G. S.; Keszler, D. A. Chemical and Structural Investigation of High-Resolution Patterning with HafSOx. *ACS Appl. Mater. Interfaces* **2014**, *6*, 2917.

(14) Anderson, J. T.; Munsee, C. L.; Hung, C. M.; Phung, T. M.; Herman, G. S.; Johnson, D. C.; Wager, J. F.; Keszler, D. a. Solution-Processed HafSOx and ZircSOx Inorganic Thin-Film Dielectrics and Nanolaminates. *Adv. Funct. Mater.* **2007**, *17*, 2117.

(15) Telecky, A.; Xie, P.; Stowers, J.; Grenville, A.; Smith, B.; Keszler, D. A. Photopatternable inorganic hardmask. *J. Vac. Sci. Technol. B Microelectron. Nanom. Struct.* **2010**, *28*, C6S19.

(16) Stowers, J.; Keszler, D. a. High resolution, high sensitivity inorganic resists. *Microelectron. Eng.* **2009**, *86*, 730.

(17) Demers, H.; Poirier-Demers, N.; Couture, A. R.; Joly, D.; Guilmain, M.; de Jonge, N.; Drouin, D. Three-Dimensional electron microscopy simulation with the CASINO Monte Carlo software. *Scanning* **2011**, *33*, 135.

(18) Schaffer, M.; Schaffer, B.; Ramasse, Q. Sample preparation for atomic-resolution STEM at low voltages by FIB. *Ultramicroscopy* **2012**, *114*, 62.

(19) Volpe, G.; Quidant, R. Fractal plasmonics: subdiffraction focusing and broadband spectral response by a Sierpinski nanocarpet. *Opt. Express* **2011**, *19*, 3612.

(20) Bond, E. J.; Member, S.; Li, X.; Hagness, S. C.; Veen, B. D. Van. Microwave Imaging via Space-Time Beamforming for Early Detection of Breast Cancer. *IEEE Trans. Antennas Propag.* **2003**, *51*, 1690.

(21) Sierpiński, W. Sur une courbe cantorienne qui contient une image biunivoque et continue de toute courbe donnée. *C. r. hebd. Seanc. Acad. Sci., Paris* **1916**, *162*, 629.

(22) Rosa, L.; Sun, K.; Juodkazis, S. Sierpin´ski fractal plasmonic nanoantennas. *Phys. status solidi - Rapid Res. Lett.* **2011**, *5*, 175.

(23) Krasnok, a E.; Maksymov, I. S.; Denisyuk, a I.; Belov, P. a; Miroshnichenko, a E.; Simovski, C. R.; Kivshar, Y. S. Optical nanoantennas. *Physics-Uspekhi* **2013**, *56*, 539.

(24) Sederberg, S.; Elezzabi, a Y. Sierpiński fractal plasmonic antenna: a fractal abstraction of the plasmonic bowtie antenna. *Opt. Express* **2011**, *19*, 10456.

(25) Yang, Y.; Dai, H. T.; Sun, X. W. Fractal diabolo antenna for enhancing and confining the optical magnetic field. *AIP Adv.* **2014**, *4*, 017123.

(26) Sederberg, S.; Elezzabi, a. Y. The influence of Hausdorff dimension on plasmonic antennas with Pascal's triangle geometry. *Appl. Phys. Lett.* **2011**, *98*, 261105.

(27) Fairbanks, M. S.; McCarthy, D. N.; Scott, S. a; Brown, S. a; Taylor, R. P. Fractal electronic devices: simulation and implementation. *Nanotechnology* **2011**, *22*, 365304.

Chapter IV

(1) Marc, R.; Pfeiffer, R.; Jones, B. Retinal prosthetics, optogenetics, and chemical photoswitches. *ACS Chem. Neurosci.* **2014**, *5*, 895.

(2) Lorach, H.; Marre, O.; Sahel, J.-A.; Benosman, R.; Picaud, S. Neural stimulation for visual rehabilitation: advances and challenges. *J. Physiol. Paris* **2013**, *107*, 421.

(3) Shepherd, R. K.; Shivdasani, M. N.; Nayagam, D. a X.; Williams, C. E.; Blamey, P. J. Visual prostheses for the blind. *Trends Biotechnol.* **2013**, *31*, 562.

(4) Zrenner, E. Will retinal implants restore vision? *Science (80-.).* **2002**, *295*, 1022.

(5) Fischer, K. E.; Alemán, B. J.; Tao, S. L.; Daniels, R. H.; Li, M.; Bünger, M. D.; Nagaraj, G.; Singh, P.; Zettl, A.; Desai, A. Biomimetic nanowire coatings for next generation adhesive drug delivery systems. **2010**, *9*, 716.

(6) Mattson, M. P.; Haddon, R. C.; Rao, A. M. Molecular functionalization of carbon nanotubes and use as substrates for neuronal growth. *J. Mol. Neurosci.* **2000**, *14*, 175.

(7) Hämmerle, H.; Kobuch, K.; Kohler, K.; Nisch, W.; Sachs, H.; Stelzle, M. Biostability of micro-photodiode arrays for subretinal implantation. *Biomaterials* **2002**, *23*, 797.

(8) Oleksak, R. P.; Ruther, R. E.; Luo, F.; Fairley, K. C.; Decker, S. R.; Stickle, W. F.; Johnson, D. W.; Garfunkel, E. L.; Herman, G. S.; Keszler, D. A. Chemical and Structural Investigation of High-Resolution Patterning with HafSOx. *ACS Appl. Mater. Interfaces* **2014**, *6*, 2917.

(9) Piret, G.; Perez, M.-T.; Prinz, C. N. Neurite outgrowth and synaptophysin expression of postnatal CNS neurons on GaP nanowire arrays in long-term retinal cell culture. *Biomaterials* **2013**, *34*, 875.

(10) Tomba, C.; Villard, C. Brain cells and neuronal networks: Encounters with controlled microenvironments. *Microelectron. Eng.* **2015**, *132*, 176.

(11) Vernekar, V. N.; Cullen, D. K.; Fogleman, N.; Choi, Y.; García, A. J.; Allen, M. G.; Brewer, G. J.; LaPlaca, M. C. SU-8 2000 rendered cytocompatible for neuronal bioMEMS applications. *J. Biomed. Mater. Res. Part A* **2008**.

(12) Xue, P.; Bao, J.; Chuah, Y. J.; Menon, N. V.; Zhang, Y.; Kang, Y. Protein covalently conjugated SU-8 surface for the enhancement of mesenchymal stem cell adhesion and proliferation. *Langmuir* **2014**, *30*, 3110.

Chapter V

(1) Zhang, S. Fabrication of novel biomaterials through molecular self-assembly. *Nat. Biotechnol.* **2003**, *21*, 1171.

(2) Xia, Y. N.; Yang, P. D.; Sun, Y. G.; Wu, Y. Y.; Mayers, B.; Gates, B.; Yin, Y. D.; Kim, F.; Yan, H. Q. One-dimensional nanostructures: synthesis, characterization, and applications. *Adv. Mater.* **2003**, *15*, 353.

(3) Welte, L.; Calzolari, A.; Felice, R. Di; Zamora, F.; Gómez-Herrero, J. Highly conductive self-assembled nanoribbons of coordination polymers. *Nat. Nanotechnol.* **2010**, *5*, 110.

(4) Wakayama, Y.; Hiroshiba, N.; Hayakawa, R.; Chikyow, T.; Kobayashi, K. Potential of Directed- and Self-Assembled Molecular Nanowires for Optoelectronic Functional Devices. *Jpn. J. Appl. Phys.* **2012**, *51*, 06FA01.

(5) Kim, F. S.; Ren, G.; Jenekhe, S. A. One-Dimensional Nanostructures of π-Conjugated Molecular Systems: Assembly, Properties, and Applications from Photovoltaics, Sensors, and Nanophotonics to Nanoelectronics†. *Chem. Mater.* **2011**, *23*, 682.

(6) Faramarzi, V.; Niess, F.; Moulin, E.; Maaloum, M.; Dayen, J.-F.; Beaufrand, J.-B.; Zanettini, S.; Doudin, B.; Giuseppone, N. Light-triggered self-construction of supramolecular organic nanowires as metallic interconnects. *Nat. Chem.* **2012**, *4*, 485.

(7) Cafferty, B. J.; Gállego, I.; Chen, M. C.; Farley, K. I.; Eritja, R.; Hud, N. V. Efficient Self-Assembly in Water of Long Noncovalent Polymers by Nucleobase Analogues. *J. Am. Chem. Soc.* **2013**, *135*, 2447.

(8) Zang, L.; Che, Y.; Moore, J. S. One-Dimensional Self-Assembly of Planar π-Conjugated Molecules: Adaptable Building Blocks for Organic Nanodevices. *Acc. Chem. Res* **2008**, *41*, 1596.

(9) Schenning, A. P. H. J.; Meijer, E. W. Supramolecular electronics; nanowires from self-assembled pi-conjugated systems. *Chem. Commun. (Camb).* **2005**, No. 26, 3245.

(10) Percec, V.; Glodde, M.; Bera, T. K.; Miura, Y.; Shiyanovskaya, I.; Singer, K. D.; Balagurusamy, V. S. K.; Heiney, P. A.; Schnell, I.; Rapp, A.; Spiess, H.-W.; Hudson, S. D.; Duan, H. Self-organization of supramolecular helical dendrimers into complex electronic materials. *Nature* **2002**, *417*, 384.

(11) Hoeben, F. J. M.; Jonkheijm, P.; Meijer, E. W.; Schenning, A. P. H. J. About Supramolecular Assemblies of π-Conjugated Systems. *Chem. Rev.* **2005**, *105*, 1491.

(12) Alam, K. M.; Singh, A. P.; Starko-Bowes, R.; Bodepudi, S. C.; Pramanik, S. Template-Assisted Synthesis of π-Conjugated Molecular Organic Nanowires in the Sub-100 nm Regime and Device Implications. *Adv. Funct. Mater.* **2012**, *22*, 3298.

(13) Engle, J. M.; Carroll, C. N.; Johnson, D. W.; Haley, M. M. Synthesis and optoelectronic properties of 2,6-bis(2-anilinoethynyl)pyridine scaffolds. *Chem. Sci.* **2012**, *3*, 1105.

(14) Carroll, C. N.; Berryman, O. B.; Johnson, C. A.; Zakharov, L. N.; Haley, M. M.; Johnson, D. W. Protonation activates anion binding and alters binding selectivity in new inherently fluorescent 2,6-bis(2-anilinoethynyl)pyridine bisureas. *Chem. Commun.* **2009**, 2520.

(15) Carroll, C. N.; Coombs, B. A.; McClintock, S. P.; Johnson, C. A.; Berryman, O. B.; Johnson, D. W.; Haley, M. M. Anion-dependent fluorescence in bis(anilinoethynyl)pyridine derivatives: switchable ON–OFF and OFF–ON responses. *Chem. Commun.* **2011**, *47*, 5539.

(16) Johnson, C. A.; Berryman, O. B.; Sather, A. C.; Zakharov, L. N.; Haley, M. M.; Johnson, D. W. Anion Binding Induces Helicity in a Hydrogen-Bonding Receptor: Crystal Structure of a 2,6-Bis(anilinoethynyl)pyridinium Chloride. *Cryst. Growth Des.* **2009**, *9*, 4247.

(17) Berryman, O.; Johnson, C.; Zakharov, L.; Haley, M.; Johnson, D. Water and hydrogen halides serve the same structural role in a series of 2+2 hydrogen-bonded dimers based on 2,6-bis(2-anilinoethynyl)pyridine sulfonamide receptors. *Angew. CHEMIE-INTERNATIONAL Ed.* **2008**, *47*, 117.

(18) Engle, J. M.; Lakshminarayanan, P. S.; Zakharov, L. N.; Haley, M. M.; Johnson, D. W. Molecular Self-Assembly: Solvent Guests Tune the Conformation of a Series of 2,6-Bis(2-anilinoethynyl)pyridine-Based Ureas. *Cryst. Growth Des.* **2011**, *11*, 5144.

(19) Hong, Y.; Lam, J. W. Y.; Tang, B. Z. Aggregation-induced emission. *Chem. Soc. Rev.* **2011**, *40*, 5361.